The Dawn of Wide-Field Sunyaev-Zel'dovich Cluster Surveys: Efficient Optical Follow-Up

A dissertation presented

by

Fredrick William High

to

The Department of Physics

in partial fulfillment of the requirements
for the degree of
Doctor of Philosophy
in the subject of
Physics

Harvard University
Cambridge, Massachusetts

May 2010

Dissertation Advisor:

Christopher W. Stubbs **Fredrick William High**

The Dawn of Wide-Field Sunyaev-Zel'dovich Cluster Surveys: Efficient Optical Follow-Up

Abstract

The South Pole Telescope team has recently reported the first 21 galaxy clusters uniformly selected by a blind Sunyaev-Zel'dovich (SZ) survey. Prompt optical imaging has confirmed the existence of red-sequence galaxy overdensities at the SZ locations, and provided first estimates of their redshift and optical richness. We have also followed up a subset spectroscopically. These are some of the most massive clusters in the universe, spanning redshifts from $z = 0.15$ to $z > 1$, with median of 0.74. This remarkable sample serves as proof of concept for SZ cluster surveys, which will provide a new, powerful window on the nature of dark energy. We are attacking the problem of following up many hundreds or thousands of SZ detections in the coming years by developing a real-time photometric calibration tool called Stellar Locus Regression. We also attack it from a hardware standpoint by building PISCO, a simultaneous multiband CCD imager. Optimizing the observing strategy alone using SLR provides a factor of 2 in cluster-confirmation yield over standard methods, and PISCO gives another factor of 3 to 4 for $z < 1$ clusters. Finally, we provide the first sky background characterization in the new CCD y band at Cerro Tololo in Chile, which will be used in next-generation astronomical camera systems and will provide useful additional information, as well as new challanges, for cluster studies such as this.

Contents

Citations to Previously Published Work

Chapter 2 was released to the preprint archives and has been submitted to The Astrophysical Journal:

> "Optical Redshift and Richness Estimates of Galaxy Clusters Selected with the Sunyaev-Zel'dovich Effect from 2008 South Pole Telescope Observations", High, Stalder, Song, Ade, Aird, Benson, Bertin, Bleem, Brodwin, Buckley-Geer, Carlstrom, Challis, Chang, Crawford, Crites, de Haan, Desai, Dobbs, Dudley, Foley, George, Gladders, Halverson, Hamuy, Hansen, Holder, Holzapfel, Hrubes, Joy, Keisler, Lee, Leitch, Lin, Loehr, Lueker, Marrone, McMahon, Mehl, Meyer, Mohr, Montroy, Morell, Ngeow, Padin, Plagge, Pryke, Reichardt, Rest, Ruel, Ruhl, Schaffer, Shaw, Shirokoff, Smith, Spieler, Staniszewski, Stark, Stubbs, Tucker, Vanderlinde, Vieira, Williamson, Wood-Vasey, Yang, Zahn, & Zenteno, submitted to ApJ, arXiv:1003.0005v1.

Chapter 3 was published in in The Astronomical Journal:

> "Stellar Locus Regression: Accurate Color Calibration, and the Real-time Determination of Galaxy Cluster Photometric Redshifts", High, Stubbs, Rest, Stalder, & Challis, AJ, 138, 110.

Chapter 4 was released to the preprint archives and has been submitted to Publications of the Astronomical Society of the Pacific:

> "Sky Variability in the y Band at the LSST Site", High, Stubbs, Stalder, Gilmore, & Tonry, accepted to PASP, arXiv:1002.3637v1.

Electronic preprints, which have the prefix "arXiv", are available at the URL `http://arXiv.org/`.

Acknowledgments

This dissertation could not have been written without the loving support of my wife Reshama, my parents Sally and Ben, my sister MaryEllen, and my grandparents Nancy and Tom.

I thank Armin Rest for the years of scientific, professional, and personal guidance that enabled me to succeed in graduate school. I am deeply grateful to him and to Brian Stalder, Ryan Foley, Mark Brodwin, Jonathan Ruel, Pete Challis, Gautham Narayan, Tony Stark, and Chris Stubbs for working hard, doing what they love, loving what they do, and being all around passionate, friendly, and collegial by nature. Graduate school was worthwhile principally because it was a joy to work with these people everyday.

I also thank Jason Rhodes for continued guidance and friendship.

Working with the South Pole Telescope team has been wonderfully surprising. Tom Crawford, Joaquin Vieira, Keith Vanderlinde, Brad Benson, Dan Marrone, Bill Holzapfel, John Carlstrom, and many others on that team have proven to be some of the smartest and friendliest people I've had the great fortune to work with, and I very much look forward to joining them in Chicago.

Finally, my advisor Chris Stubbs showed great patience and enthusiasm while guiding me through the landscape of professional research. He imparted not only scientific knowledge, but the practice of ethical and collegial conduct. Any effectiveness I may now have in working in a collaborative research environment I attribute to Chris's training. I cannot thank Chris enough for the time, effort, and resources he invested in me.

For Reshama.

Chapter 1

Introduction

The standard model of particle physics has described the properties and behavior of the elementary particles with exquisite accuracy for decades, but it excludes gravity. Our picture of the entire cosmos as a whole, where gravity is a dominant player, has independently crossed into the realm of precision science in the last ten years as well. And yet the particle nature of the universe's overwhelmingly predominant constituents—dark energy (74% of all mass-energy) and dark matter (22% of all mass-energy, Dunkley et al., 2009)—and indeed of gravity itself, is still unknown. It is the highest priority in both cosmology and particle physics to resolve this tension.

Galaxy clusters are a unique testbed for both dark matter and dark energy. Galaxy clusters are the largest gravitationally bound structures in the present day universe (see Voit, 2005, for a review). Fritz Zwicky was first to infer the existence of dark matter by observing that the dispersion of galaxy velocities in the Coma cluster was many times greater than that expected from the total gravitational potential of all the luminous stars (Zwicky, 1933). Today we regularly "see" the dark matter in galaxy clusters in the same way we see a perfectly clear wine glass: by the lensing effect it has on objects in the background, in this case induced by the great gravitational potentials (Narayan & Bartelmann, 1996, give a review on gravitational lensing).

The statistical clustering of dark matter is extremely well characterized via cosmological simulations, and is highly sensitive to dark energy (Jenkins et al., 2001; Tinker et al., 2008). Dark energy assists, indeed *accelerates*, the expansion of the universe today (Riess et al., 1998; Perlmutter et al., 1999), effectively counteracting the gravitational collapse of the largest structures in the universe, galaxy clusters. Counting the most massive clusters in existence is a simple yet powerful way to characterize dark energy (Albrecht et al., 2006). The study of galaxy clusters holds great promise in helping to solve what may be the single greatest problem in physics today: what is dark energy?

1.1 The Sunyaev-Zel'dovich Effect

The principal challenge in surveying clusters for the purpose of measuring dark energy is understanding the selection function, and Sunyaev-Zel'dovich (SZ) effect methods offer the best selection for the task. The SZ effect (Sunyaev & Zel'dovich, 1972) is the inverse Compton scattering of cosmic microwave background (CMB) photons by the hot electrons of the intra-cluster medium. The SZ effect slightly boosts the blackbody spectrum of CMB photons, leaving a characteristic imprint on the primary CMB structure on cluster-size scales of about an arcminute (Birkinshaw, 1999). The surface brightness of the SZ imprint is independent of redshift, and the integrated effect is nearly so. In addition, the SZ signal strength is directly sensitive to the total thermal energy of the instra-cluster medium, and therefore to the total cluster mass. The SZ effect provides a way to discover all clusters in the universe above a nearly fixed mass threshold (Carlstrom et al., 2002)—something that no other technique can offer.

The South Pole Telescope (SPT; Carlstrom et al., 2009) is a new facility dedicated to searching for the SZ effect for the purpose of measuring dark energy. The SPT is a 10 m telescope at the South Pole Station in Antarctica that observes the sky at millimeter wavelengths, near the peak of the CMB intensity. The SPT saw first light in February 2007, and presented the first galaxy clusters ever detected *first* by their SZ effect a year and a half later (Staniszewski et al., 2009). The list was expanded from four to 21 another 17 months later (Vanderlinde et al., 2010; High et al., 2010a). Vanderlinde et al. (2010) and High et al. (2010a) presented the catalog of 21 clusters and, using them, provided first constraints on dark energy's equation of state paramter w, in combination with other cosmological data sets. These publications are the first to prove empirically that SZ cluster surveys, and dark energy measurements using them, are possible.

1.2 The Optical Aspect

SZ signals alone contain no redshift information, yet cluster redshifts are needed to make competitive dark energy measurements. The most efficient way to achieve this is to image SZ clusters at optical wavelengths and estimate redshifts with broadband photometry. Optical follow-up is a necessary component of dark energy experiments using the SZ cluster technique, and it may be argued an "SZ cluster survey" is in fact the combination of millimeter cluster detection and optical and infrared follow-up.

High et al. (2010a, reproduced here as Chapter 2) presented the first coordinated optical work in an SZ survey, and was the companion to the publication of Vanderlinde et al. (2010). High et al. (2010a) showed optical pictures of the clustered galaxies, confirming the existence of eponymous "galaxy clusters" near the SZ detections. They also presented spectroscopic and photometric redshift estimates for the 21 clusters, as well as rough estimates of total cluster mass derived directly from the optical data.

A major challenge for the optical follow-up effort is to keep abreast of SPT's expected yield. SPT's nominal plan is to survey 500 $\deg^2$ per year. Vanderlinde et al. (2010) showed that SPT yields one cluster with SZ detection significance of 5 or greater (corresponding to total cluster masses of $\gtrsim 3-5\times 10^{14}M_\odot$) approximately every 8 $\deg^2$. Figure 1.1 shows SPT's projected cluster yield, which has been empirically calibrated using these results. At detection significance of ≥ 5, SPT will deliver about 60 detections per year with about 95% purity, all of which must be followed up in the optical. If an overall purity of 50% is allowed, then all clusters with detection significance $\gtrsim 4.2$ would require follow-up, which corresponds to one detection every 2 $\deg^2$ or 250 detection per year. This is a significant challenge given realistic estimates of total telescope time awarded per year to a typical team of astronomers.

Put another way, follow-up in SPT's cluster survey is optical telescope-time limited. The primary goal is to obtain a sample with as clean a selection in mass as possible, and the most straightforward way to do this is to select all objects above a chosen SZ detection significance value. This was the approach taken by Vanderlinde et al. (2010), and it allowed for a useful cosmological analysis to be performed

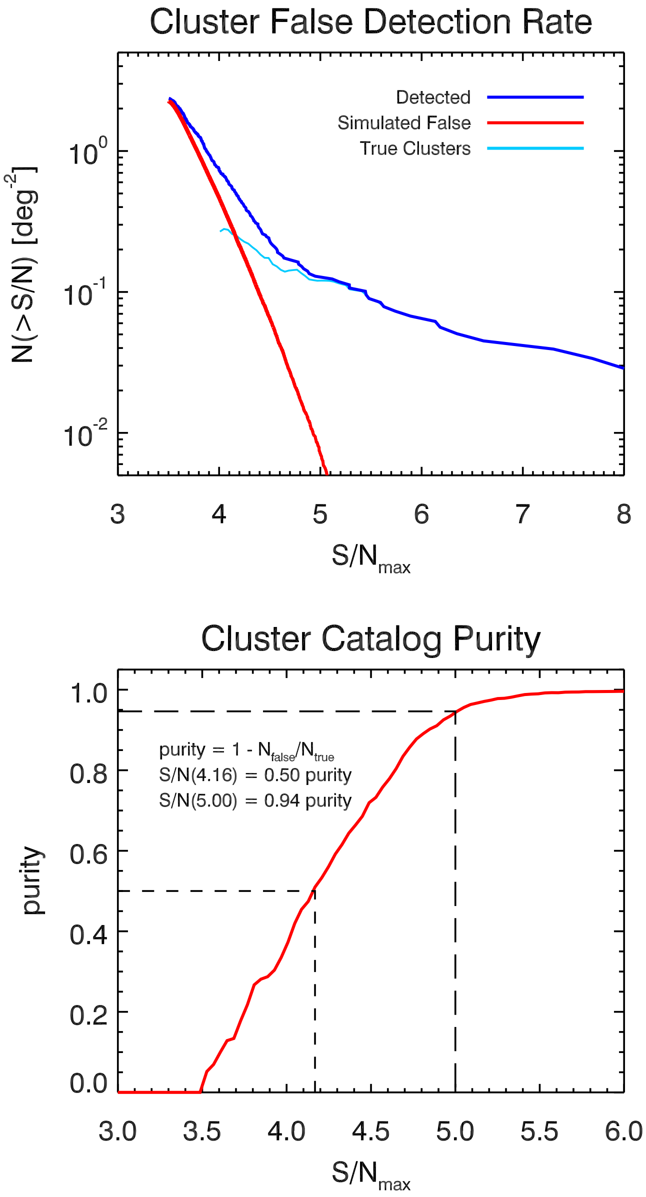

Figure 1.1: SPT's projected cluster yield as a function of SZ detection threshold. The top panel shows the cumulative number of clusters per square-degree with S/N greater than the value given, as well as the number of objects falsely identified as clusters. The bottom panel shows the fraction of objects that are true clusters versus lower S/N threshold.

with as few as 21 clusters. It follows that the lowest possible SZ detection significance threshold should be adopted such that the total cluster sample size is maximal while still permitting complete optical follow-up, thus minimizing statistical uncertainties on cosmological parameters. Therefore the optical follow-up strategy should be optimized to yield the greatest possible number of cluster redshifts, and achievable follow-up yield determines the lower threshold of SZ detection significance.

1.3 Efficient Follow-Up

In thinking about how to maximize the yield of optical cluster follow-up, we have made a number of innovations on both the strategy and the apparatus fronts. The simplest and most immediately accessible innovation involves modifying the observing strategy during a typical observing run.

A reasonable, quantitative goal of an optical follow-up run would be to detect early-type galaxies with rest-frame luminosity brighter than $L*$ in $4''$ apertures with signal-to-noise ratio greater than 10 in the Sloan Digital Sky Survey's r, i, and z passbands. These passbands are chosen because the color $r - z = (r - i) + (i - z)$ of early-type galaxy colors is unambiguously monotonic over the broadest redshift range available from any other passband combination, $0 < z \lesssim 1.5$ (see §2.3.1). We adopt this as the nominal goal of any observing strategy, and use the IMACS imager on the Magellan 6.5 m telescope at Las Campanas Observatory in Chile as our hypothetical facility. The model galaxies used in our analysis here are described in §2.3.1.

1.3.1 A Typical Observing Strategy

The most straightforward strategy is to observe all SZ detections with fixed total exposure time, and to choose the total exposure times such that the minimum required statistical uncertainty is reached on all clusters up to a maximum chosen redshift of, for example, unity. Individual SZ cluster detections come with no redshift priors, so it is reasonable to treat all candidates equally like this.

In a realistic observing run on IMACS, one would split the exposures up by first observing in (g, r, i, z) at 60 s each, then obtain additional (r, i, z) exposures at $(320, 60, 80)$ s to reach the nominal optical detection requirements on redshift 1 early-type cluster galaxies. With 60 s CCD readout time, this translates to about 18 min spent per cluster, for a total yield of about 3 clusters per hour or 30 clusters per 8 hr night. A team of astronomers may realistically expect to be awarded about 3 nights per year on a 6.5 m-class telescope such as Magellan, for a total of about 90 clusters per year. Because the goal is to follow up a sample of clusters that is complete in SZ detection significance, a threshold of ~ 4.8 should be adopted. This calculation has assumed, for simplicity, that only a negligibly small fraction of the clusters are at redshift > 1.

1.3.2 An Efficient Observing Strategy

It is easy to imagine a simple modification to this strategy. If the observer can quantitatively determine whether the desired sensitivity has been reached on a low redshift cluster *in the initial* 60 s *exposures*, then the observer can decide not to obtain the additional exposures on that cluster, and instead move on to the next SZ detection in the list. If the cluster is not seen or 10σ significance is not reached on the L^* early-type galaxies in riz, then a decision can be made to take the additional exposures.

This strategy is schematically illustrated in Figure 1.2, together with the exposure time calculations for each $griz$ band on IMACS individually, and the overhead requirements from CCD readout. These exposure time calculations show that the initial set of 60 s exposures reaches sufficient statistical significance for clusters at $z \lesssim 0.8$. If 80% of the SZ detections are assumed to be clusters at $0 < z < 0.8$, and the rest are within $0.8 < z < 1.0$, then an average of about 10 min is spent per cluster rather than the 18 min from before, yielding about 50 cluster confirmations in an 8 hr night. Thus by examining the images and photometry at the telescope during an observing run, and making decisions in real time on whether to acquire more exposures, the number of SZ clusters confirmed in the optical increases by nearly a factor of 2. Over the nominal 3 nights per year on a Magellan-like telescope, this yields 150 clusters per year, corresponding to SZ detection significance of ~ 4.4.

We have used this strategy in following up the SPT SZ detections presented in Vanderlinde et al. (2010) and High et al. (2010a), as well as additional clusters that have not yet been published. Our record yield was 27 cluster confirmations at $z \lesssim 1$ in about 4 hr, which extrapolates to 54 clusters in a full 8 hr night, in agreement with our hypothetical calculation here.

Performing astronomical imaging data reductions in real time is not a simple or easy task. It requires ample preparation and robust software. If these requirements are met, then one will be faced with the fundamental limiting temporal factor in

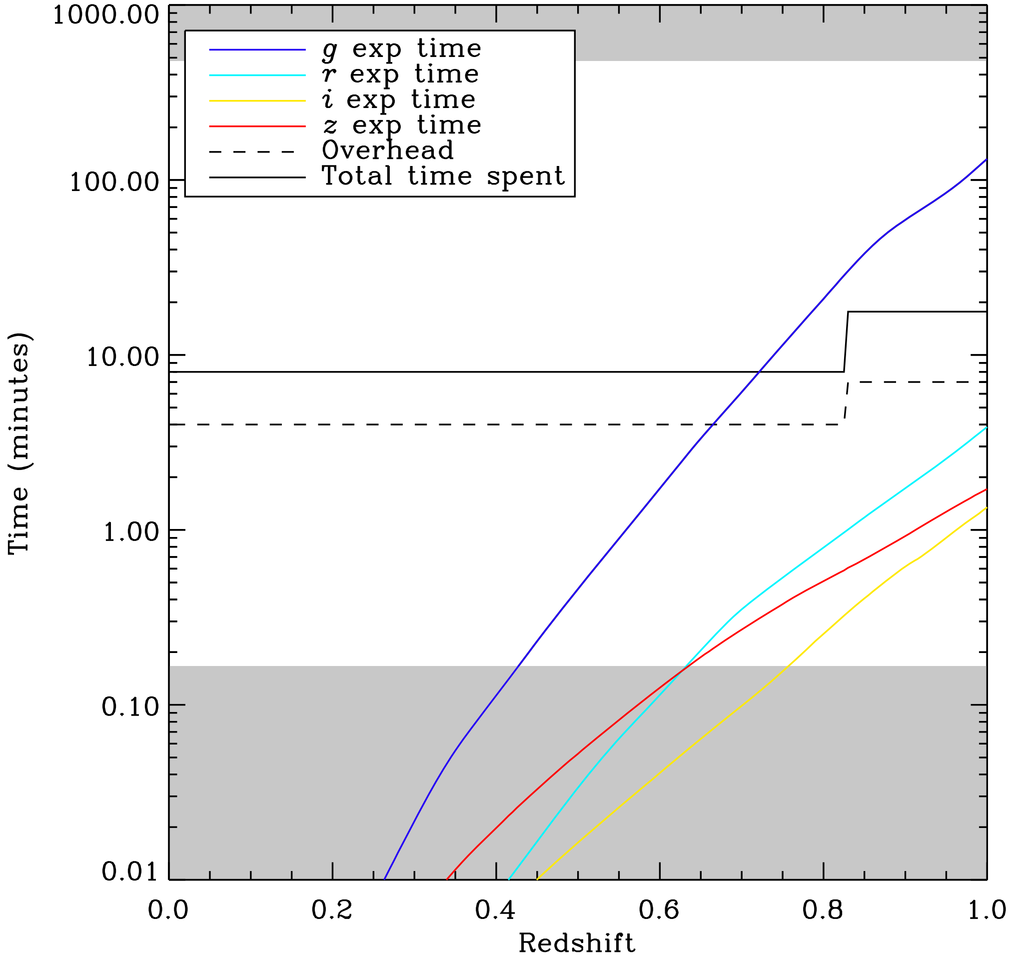

Figure 1.2: Total exposure time required to achieve a 10σ detection of L^* early-type galaxies in $4''$ apertures in the Sloan Digital Sky Survey passbands using the IMACS imager on the Magellan 6.5 m telescope.

the standard data reduction algorithm: photometric flux calibration. The typical approach to calibration is to observe standard stars in between science exposures. Flux levels of a given celestial object can change with apparent position on the sky because the light traverses different amounts of atmosphere, which scatters and absorbs photons. Flux levels at a fixed position on the sky can also change with time due to variability in the atmosphere, particularly in the presence of water vapor in "non-photometric" conditions. To account for these effects, astronomers must observe standard stars frequently during the night, and over a range of air masses. Calibration is achieved by assuming a calibration model that accounts for extinction, estimating model parameters with the network of standard star fields, *and interpolating those parameters in both space and time to the science fields.* It is therefore necessary to obtain the complete network of standard star fields over a full night before embarking on photometric calibration of one's science fields. The minimum time needed to perform final calibrations is therefore about 12 to 24 hr, though it is common practice not to begin the analysis at all until well after the entire observing run has been completed.

We have eliminated this bottleneck by developing Stellar Locus Regression (SLR, Chapter 3). SLR uses the stars appearing any field whatsoever to calibrate the photometry of all objects in the same field by taking advantage of the astrophysically fundamental distribution of the colors of stars. Besides eliminating the need for standard star observations, SLR produces highly accurate photometric calibrations even in non-photometric conditions. This is because the stars appearing in a set of science images are used to calibrate the flux of all the objects in that field, which are behind the same air mass. SLR is a general purpose tool that allows astronomers to produce final calibrations at the telescope during observations, immediately upon readout of a set of multiband images of a given field. It therefore enables for decisions to be made in real time during SZ cluster follow-up—indeed, in any program.

While this efficient strategy provides a significant improvement in cluster yield, it is reasonable to continue to seek yet greater yields. With the major strategic bottleneck now eliminated thanks to SLR and an efficient observing strategy, we look to optimizate the *apparatus*. To this end, we have designed a simultaneous multiband imager called PISCO.

1.3.3 PISCO

PISCO is the Parallel Imager for Southern Cosmological Observations, a CCD camera intended for the Magellan 6.5 m telescopes that images in the $griz$ bands in a single exposure. Its defining features are four different focal planes, a series of three dichroic beamsplitters, and a single photometric shutter that serves them simultaneously.

Dichroic beamsplitters are optical elements that transmit red light and reflect blue, and the transition wavelength is highly tunable. The first dichroic in PISCO's optical train passes iz light and reflects gr light. A second dichroic in the iz beam is tuned to pass z band wavelengths and reflect i, each of which is focused onto its own focal plane with independent CCDs. And a third dichroic in the gr beam is tuned to pass r light and reflect g, each of which focuses again to its own focal plane with independent CCDs. PISCO thereby captures all photons within the $griz$ system in a single shutter cycle. On average this saves a factor of 4 in time spent obtaining *griz* imaging of a given field. Compared to a direct imager that contains a minimum number of glass optical elements, PISCO suffers a roughly 20% relative reduction in overall photon efficiency due to its reimaging optics, so this gain may be closer to a factor of 3 depending on the instrument being compared.

In light of our hypothetical IMACS program in §1.3.2, this factor of 3 or so in efficiency directly translates to 3 times more SZ cluster confirmations and redshifts, or nearly 500 clusters per year assuming three 8 hr nights per year on PISCO and adoption of the efficient observing strategy. This is about 6 to 7 times the yield of the traditional observing strategy described in §1.3.1. This well exceeds the nominal requirement of obtaining a cluster catalog complete at SZ detection significance of 4.2 and greater.

1.4 Summary

We have performed and published the optical follow-up to the first successful blind SZ cluster survey in history, and it has highlighted the future challenges in keeping abreast of the number of clusters SPT is expected to yield every year. Here we have shown that, with appropriate adjustments in observing strategy as enabled by the accurate, real-time photometric data calibrations of SLR, and by using the PISCO simultaneous multiband imager, it will be possible, within the same year, to follow up a complete sample of South Pole Telescope SZ detections down to the lowest significance levels that push the limit of acceptable false-detection rates, at $\gtrsim 50\%$. This means that the cosmological analysis using such a continuously-growing cluster sample can be maximally precise thanks to a maximized sample size, and can be performed the same year as the discovery. The speeds are significantly greater than would be possible using traditional pointed or contiguous survey strategy, in the regime of days rather than months and years.

Chapter 2 of this dissertation describes the optical follow-up results for the South Pole Telescope's 2008 cluster survey. Chapter 3 outlines the Stellar Locus Regression method of real-time photometric calibration, which was used successfully in the SPT optical follow-up program. Finally, Chapter 4 describes the first results of sky brightness measurements at Cerro Tololo, Chile, in a new CCD passband at one micron, y. This new band will be deployed by next-generation camera systems, and will provide useful additional information, as well as new challenges, for the kinds of cluster studies we discuss here.

Chapter 2

Optical Follow-Up of the First 21 SZ Clusters

2.1 Introduction

Galaxy clusters are laboratories for both astrophysics and cosmology (Evrard, 2004). Clusters represent the most massive dark matter halos, and their number density as a function of cosmic time is highly sensitive to dark energy (Wang & Steinhardt, 1998; Haiman et al., 2001; Holder et al., 2001; Battye & Weller, 2003; Molnar et al., 2004; Wang et al., 2004; Lima & Hu, 2007). The mass of these systems is dominated by dark matter, but the primary means of observing clusters—especially large samples of them—are the luminous baryons of the hot intracluster gas and the galaxies themselves. The formation of the halos is well understood, while the precise behavior of the baryons is not as well modeled (see Voit, 2005, for a review). This gap must be closed so that data from large cluster surveys can place precise constraints on cosmological parameters over a wide range of redshifts. Multi-wavelength observations of a cleanly selected, redshift-independent sample of galaxy clusters are a potentially powerful method of achieving this.

Searches for galaxy clusters using the Sunyaev-Zel'dovich (SZ) effect (Sunyaev & Zel'dovich, 1972) promise to provide such a clean, redshift-independent sample. The SZ effect is scattering of cosmic microwave background photons to higher energy by the hot electrons in galaxy clusters (Birkinshaw, 1999). The SZ surface brightness is independent of redshift but is closely related to cluster mass and so it is expected to be an excellent method for creating approximately mass-limited samples extending over a wide redshift range (Carlstrom et al., 2002). The constraints on cosmological parameters from such samples are complementary to geometrical tests using type Ia supernovae and baryon acoustic oscillations (e.g., Vikhlinin et al., 2009). Two SZ surveys, the Atacama Cosmology Telescope (ACT; Fowler et al., 2007) and the South Pole Telescope (SPT; Carlstrom et al., 2009) projects, are well positioned to provide large surveys which can be used for growth of structure studies.

Staniszewski et al. (2009, hereafter S09) presented the first discovery of previous unknown galaxy clusters using their SZ signature. Cluster redshifts are needed in addition to SZ data to provide the strongest constraints on dark energy. Coordinated optical follow-up observations can provide the needed redshift measurements. The Blanco Cosmology Survey (BCS; Ngeow et al., 2006, and `http://cosmology.illinois.edu/BCS/`), an NOAO survey program (2005-2008), provided multiband optical observations for the initial follow-up of portions of the first SPT survey fields. These data were used to identify optical counterparts to the S09 sample, search for giant arcs, explore possible cluster superpositions, and derive photometric redshifts.

Cluster mass can be estimated using several methods: the SZ and X-ray luminosity, which are sensitive to intracluster electrons; the number, luminosity, and velocity dispersion of cluster galaxies; and from gravitational lensing, which is the most direct probe of total cluster mass. Menanteau & Hughes (2009) characterized the galaxy counts and luminosity of the S09 cluster sample, and McInnes et al. (2009) subsequently explored their weak gravitational lensing signals.

Using data acquired by the SPT in 2008, Vanderlinde et al. (2010, hereafter V10) present an additional 17 SZ-detected clusters. Here we describe coordinated optical imaging of the catalog of 21 uniformly selected SZ detections, and new spectroscopic results on 8 of the clusters. Counterparts to a subset have been found in the catalogs of Abell et al. (1989a, hereafter A89) and Menanteau et al. (2010, hereafter SCS-II). Seven clusters fell within the BCS footprint. For the remaining 14 clusters, and also for a subset of the BCS sample, we conducted pointed imaging observations and, for 8 clusters, spectroscopic observations, with the Magellan telescopes. The photometry was used to search for overdensities of red-sequence galaxies near the SZ locations, and if present, estimate their redshifts and also characterize their mass via optical red-sequence galaxy counts, or *richness*.

We describe in §2.2 the observations and data reduction. Section 2.3 outlines the redshift and richness analysis we used, and §4.6 describes the results on redshift (§2.4.1) and richness (§2.4.2). In Section 3.5 we discuss the results, and conclude with §2.6.

Throughout this paper we assume a flat concordance ΛCDM universe, with

$(\Omega_\Lambda, \Omega_\mathrm{M}, h) = (0.736, 0.264, 0.71)$ (Dunkley et al., 2009). All magnitudes are in the Sloan Digital Sky Survey (SDSS) *griz* AB system.

2.2 Data Acquisition & Reduction

Cluster detection was achieved using millimeter-wavelength data from the South Pole Telescope, and optical imaging and spectroscopy provided cluster confirmation and redshift and richness estimates.

2.2.1 South Pole Telescope

The sample of 21 clusters presented here and in V10 is the first cosmologically significant catalog of clusters selected via the SZ effect. The sample was selected from two SPT survey fields totaling $178\,\mathrm{deg}^2$ at R.A. = $23^\mathrm{h}30^\mathrm{m}$, Decl. = $-55°$ and R.A. = $5^\mathrm{h}30^\mathrm{m}$, Decl. = $-55°$ (J2000). Both fields were observed with arcminute resolution to an equivalent white noise level of 18 μK-arcmin[1].

The SPT time-ordered data were filtered and binned into maps, with the filtering acting roughly as a 1° high-pass filter in the R.A. direction. Clusters were extracted from these maps using a matched filter approach based on the work of (Haehnelt & Tegmark, 1996; Herranz et al., 2002a,b; Melin et al., 2006). Spatial filters were constructed to maximize detection significance within a set of cluster profiles. The SPT astrometry is based on comparisons of radio source positions derived from SPT

---

[1] The unit K refers to equivalent fluctuations in the CMB temperature, i.e., the level of temperature fluctuation of a 2.73 K blackbody that would be required to produce the same power fluctuation. See V10.

maps and positions of those sources in the AT20G catalog (Murphy et al., 2010), and should be accurate to $5''$.

Cluster candidates were then identified by selecting all peaks above a fixed significance threshold and choosing the filter scale which produced the maximum detection significance ξ. A 3 parameter model for M_{200} involving ξ and the cluster redshift is presented in V10, along with the details of the SPT data reduction.

2.2.2 Blanco Cosmology Survey

BCS is an NOAO survey program to obtain deep *griz* imaging of two southern fields centered at R.A. = $23^{\rm h}00^{\rm m}$, Decl. = $-55^\circ 12'$ and R.A. = $5^{\rm h}30^{\rm m}$, Decl. = $-52^\circ 47'$ (J2000), each roughly 50 $\deg^2$. The 2008 SPT survey fields are larger than the BCS fields and include the entire BCS regions. BCS was conducted from 2005–2008 using the Mosaic-II wide-field imager on the Blanco 4 m telescope at Cerro Tololo Inter-American Observatory. Mosaic-II is an array of eight $2\,\mathrm{k} \times 4\,\mathrm{k}$ CCDs with a pixel scale of $0.270''$ pixel^{-1} and a 0.36 $\deg^2$ field of view. The strategy was to obtain deep, contiguous *griz* imaging of the survey fields. In addition, BCS imaging was carried out for 7 photometric redshift calibration fields which include a sample of several thousand published spectroscopic redshifts.

The BCS data were processed and calibrated using a data management system developed for the Dark Energy Survey (Ngeow et al., 2006; Mohr et al., 2008) and run on the NCSA TeraGrid IA-64 Linux cluster. Data reduction includes crosstalk correction, overscan correction, bias subtraction, flat fielding, fringe and illumination corrections, field distortion correction, standard star photometric calibration, coaddstacking, and photometric extraction of sources. BCS stacks typically reach 5σ galaxy photometry limits of 24.75, 24.65, 24.35 and 23.5 mag in *griz*, corresponding, for example, to a $0.5L^*$ cluster elliptical at $z = 1$. Completeness measurements in a typical field that are derived from comparison with deeper, better seeing CFHT data suggest 50% completeness limits of 24.25, 24.0, 23.75 and 23.0 in *griz* (Zenteno et al. in prep.).

2.2.3 Magellan

2.2.3.1 Imaging

For clusters that fell outside the BCS coverage region, for 5 that were within the BCS region, and for the unconfirmed candidate (see §2.4.3) we obtained *griz* imaging with the Inamori Magellan Areal Camera and Spectrograph (IMACS; Dressler et al., 2003a; Osip et al., 2008a) and Low Dispersion Survey Spectrograph (LDSS3; see Osip et al., 2008a)—both in imaging mode—on the twin Magellan 6.5 m telescopes. IMACS is on the Magellan Baade telescope at the $f/11$ Nasmyth focus. Its circular field of view in $f/2$ mode subtends 0.20 deg^2, mapped onto a 8192×8192 pixel, 8-chip CCD array, for a pixel scale of $0.200''$ pixel^{-1}. LDSS3 is on the Magellan Clay telescope at the $f/11$ Nasmyth focus, and its roughly 60 arcmin^2 circular field of view maps onto a subregion of a 4064×4064 pixel CCD, at a pixel scale of $0.189''$ pixel^{-1}.

Using the science-tested pipeline described by Rest et al. (2005) and Miknaitis et al. (2007), the same image reduction operations described above were performed on the Magellan images. Instead of using standard stars for photometric calibration, however, we employ Stellar Locus Regression (SLR; High et al., 2009) using stars that appear in the cluster images themselves. SLR delivers photometric calibrations by regressing the instrumental color-color locus of stars in any field to the known, astrophysically fundamental locus in the AB system. SLR enabled us to forego observations of standard stars altogether, maximizing the total integration time on the cluster fields.

The principal difference in strategy between Magellan and BCS observations is that the Magellan exposure times were adaptive rather than uniform. We first exposed for roughly 100 s in $griz$, searched for a cluster in the images, and continued with additional exposures if none was found. In median seeing of $0.8''$, these exposures reach nominal, 5σ point-source limiting magnitudes of 24.8, 24.8, 24.4, and 23.4 mag in $griz$. If no cluster was detected with the initial set of images, we acquired further exposures until a detection was achieved at a depth of approximately 1 to $0.4L^*$ with respect to the early-type cluster galaxies. This strategy results in highly variable depth for the Magellan imaging, but is the most efficient use of telescope time for follow-up observations.

Figures 2.1–2.22 are false-color optical images of the clusters, together with the SZ detection significance maps. In all images, north is up, east is left.

The SZ-only insets subtend 8 arcminutes on a side. The mapping between color and SZ significance ξ is the same in all SZ thumbnails. The highest significance cluster, Figure 2.16, spans the largest color range, which is $\xi \in [-5.57, 14.94]$. The peak value in each thumbnail is equal to the quoted SZ detection significance in V10. Contours are given at steps of $\Delta(\xi) = 2$, and the corresponding values are labeled. Contours are dashed where ξ is negative, and solid where ξ is nonnegative.

The optical images have the same contours as their corresponding SZ thumbnail overlain, and subtend 1.5 Mpc in the cluster rest frame. We have mapped the zrg passbands to the RGB channels, respectively, so that the apparent redness of red-sequence cluster galaxies approximately increases with redshift.

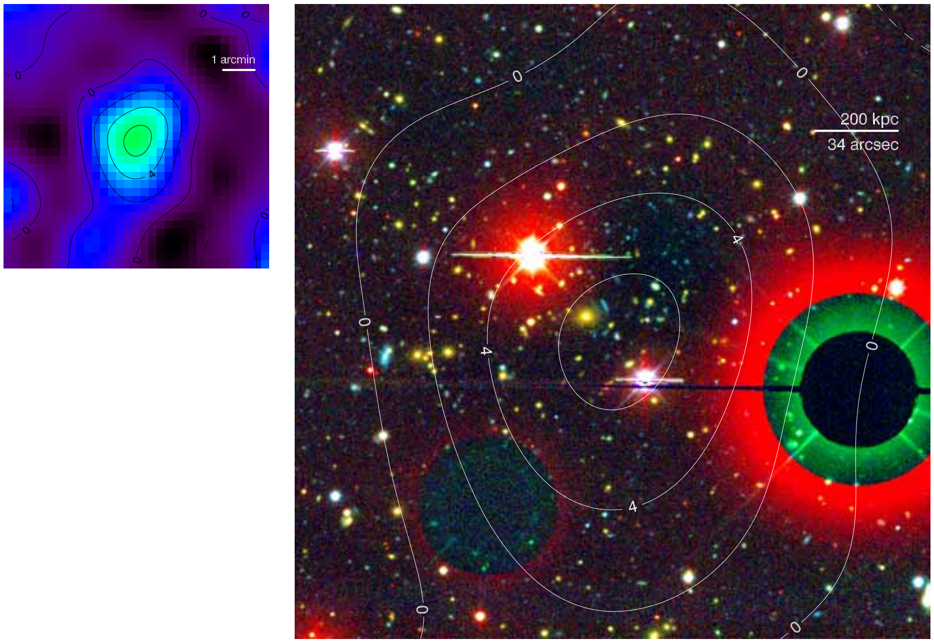

Figure 2.1: SPT-CL J0509-5342

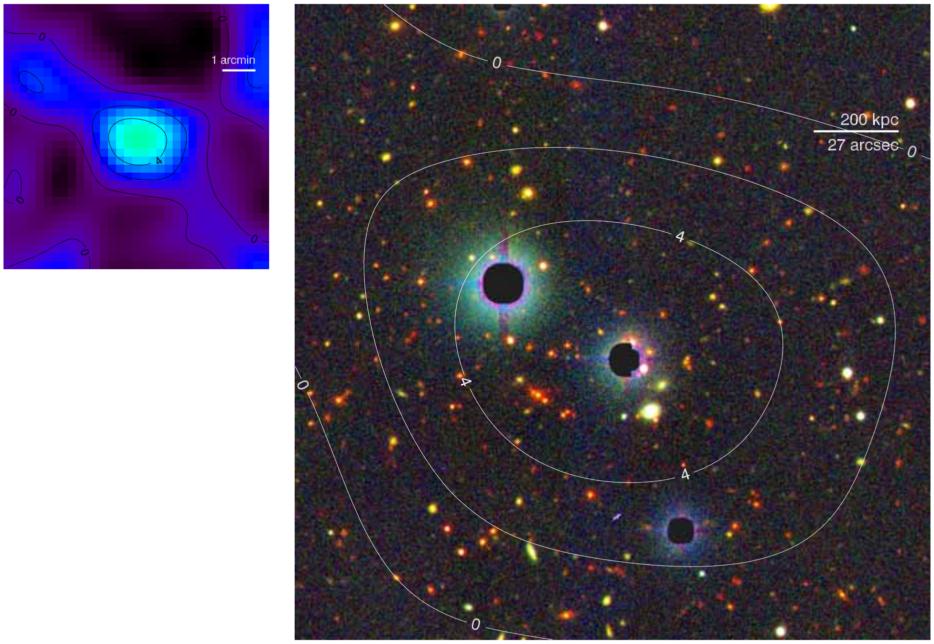

Figure 2.2: SPT-CL J0511-5154

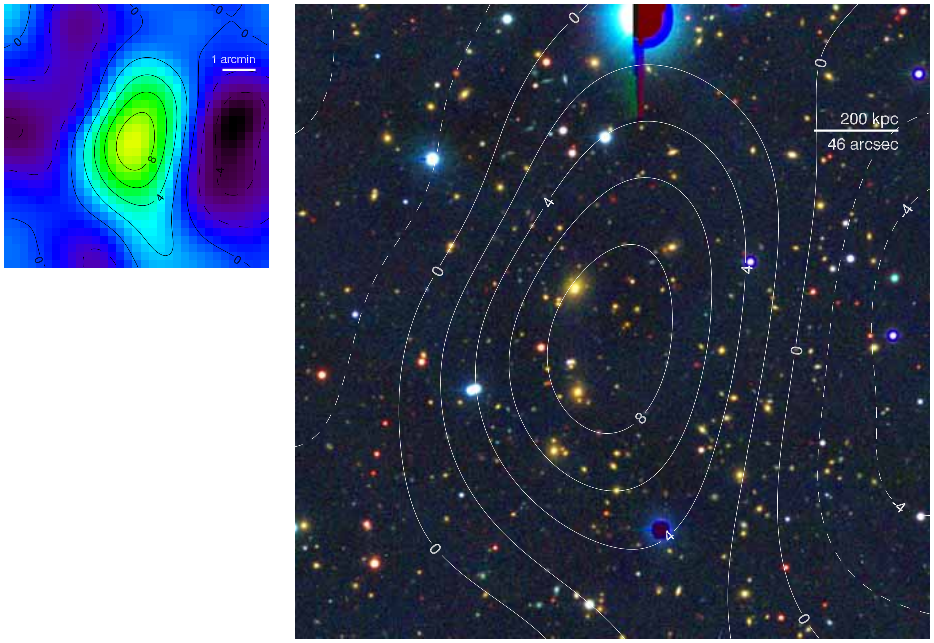

Figure 2.3: SPT-CL J0516-5430

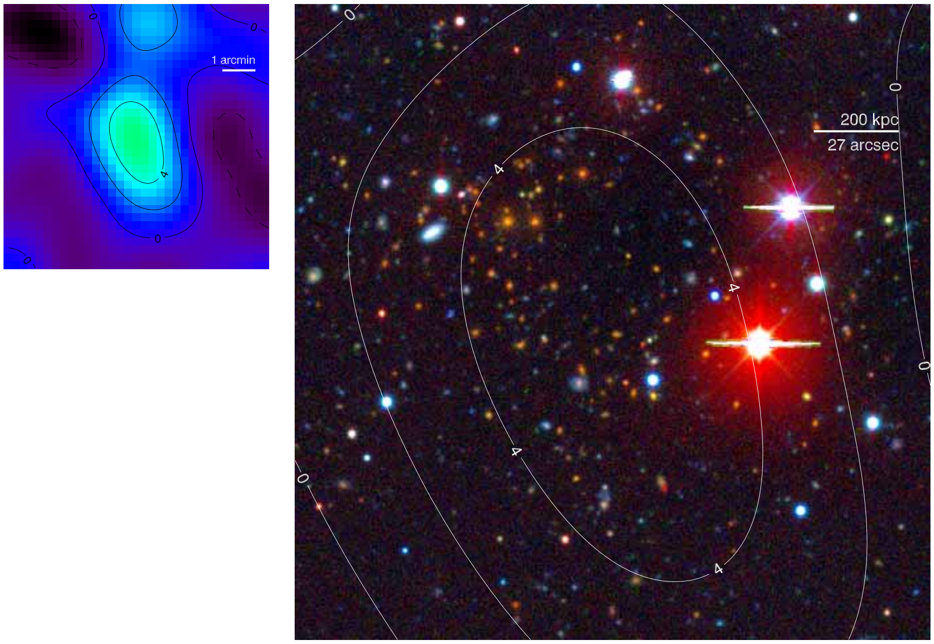

Figure 2.4: SPT-CL J0521-5104

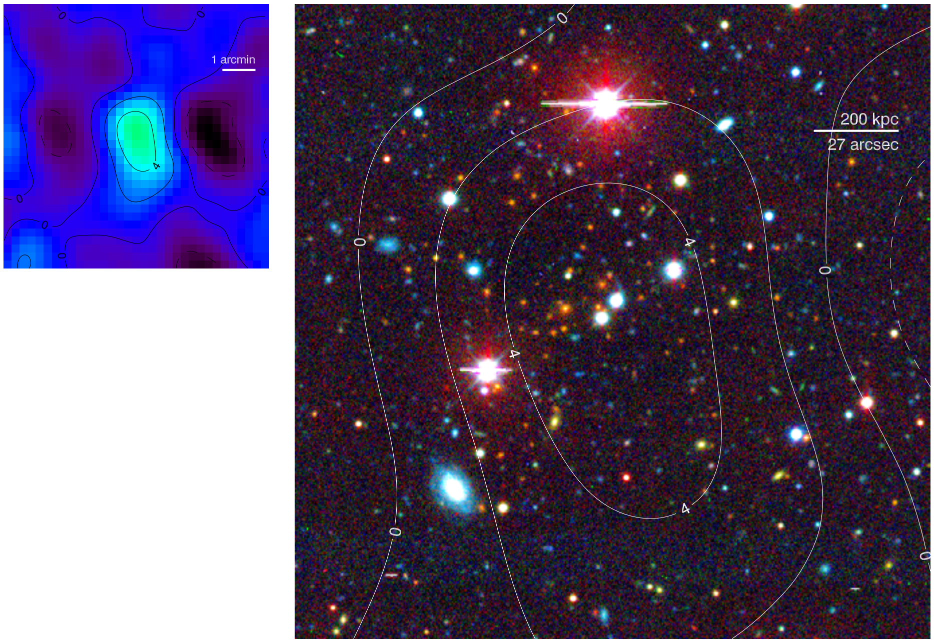

Figure 2.5: SPT-CL J0528-5300

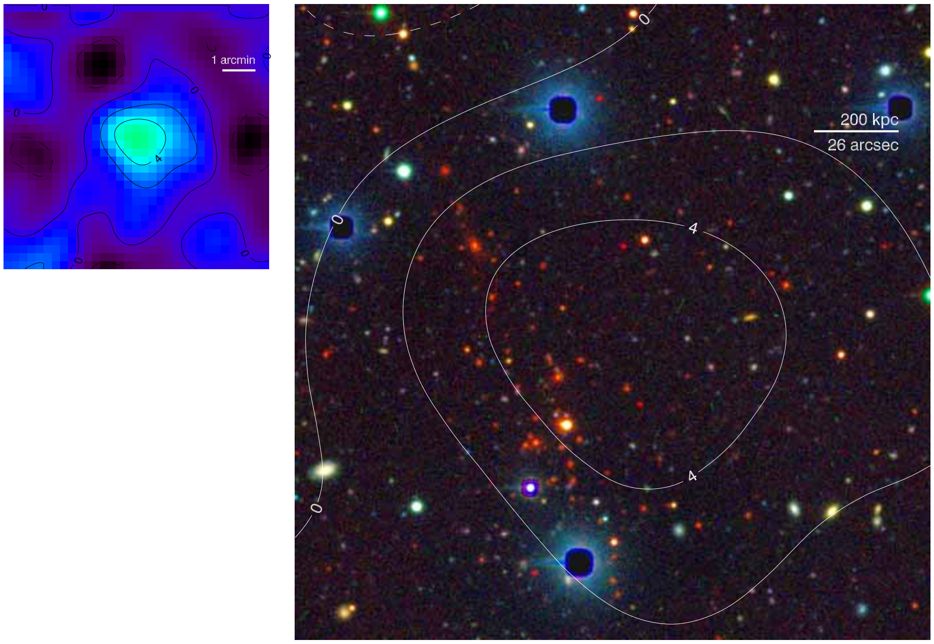

Figure 2.6: SPT-CL J0533-5005

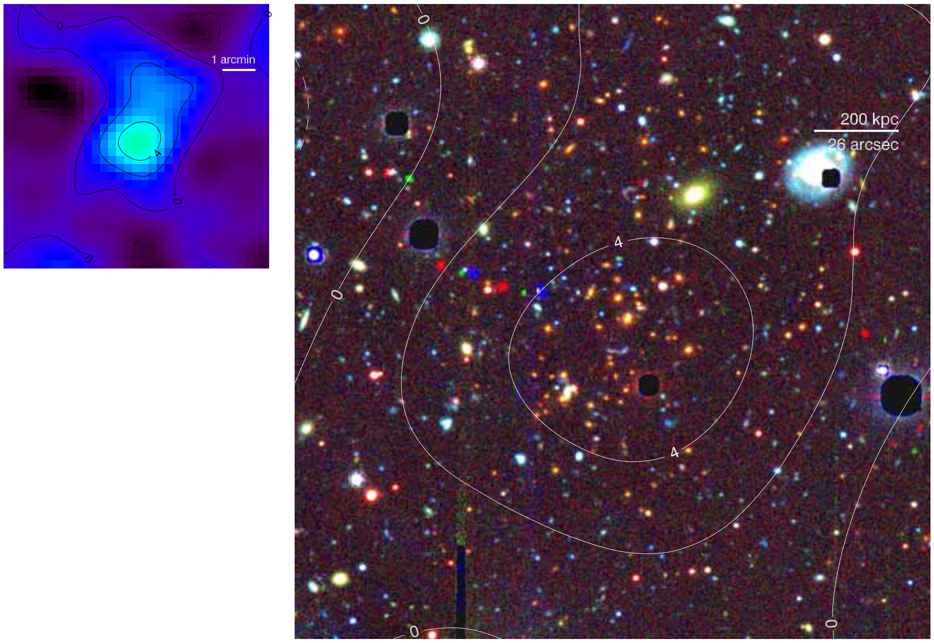

Figure 2.7: SPT-CL J0539-5744

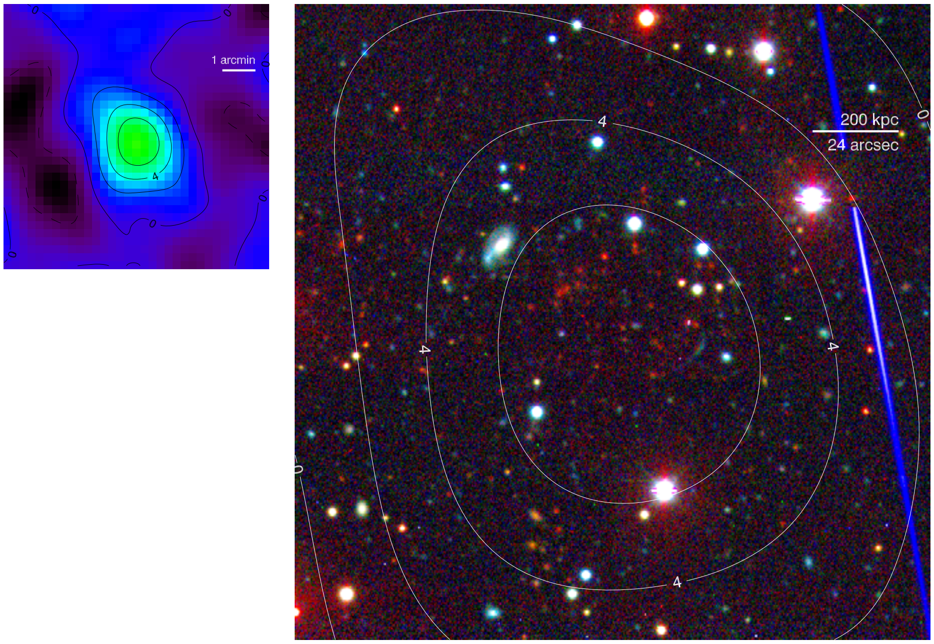

Figure 2.8: SPT-CL J0546-5345

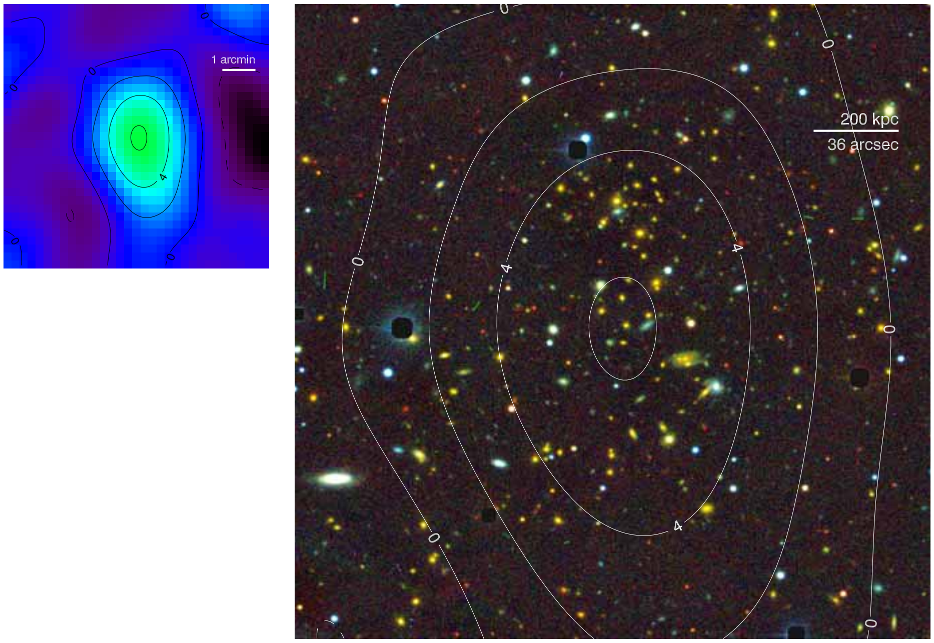

Figure 2.9: SPT-CL J0551-5709

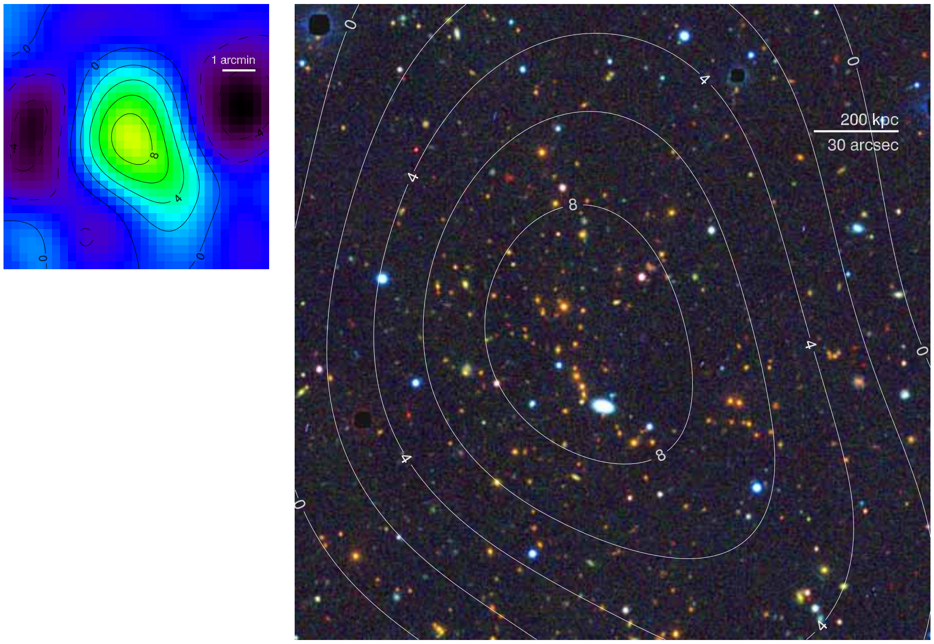

Figure 2.10: SPT-CL J0559-5249

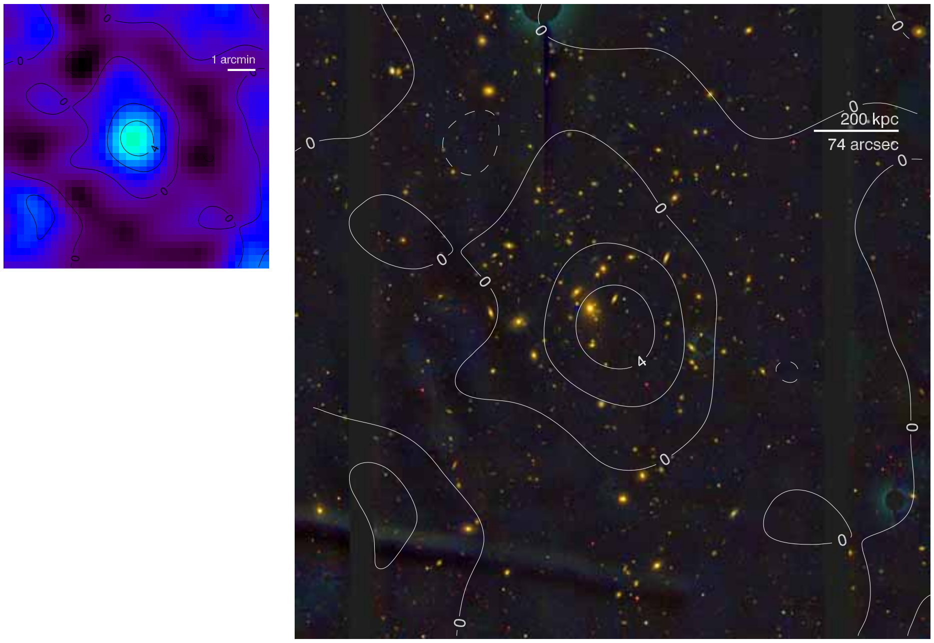

Figure 2.11: SPT-CL J2259-5617

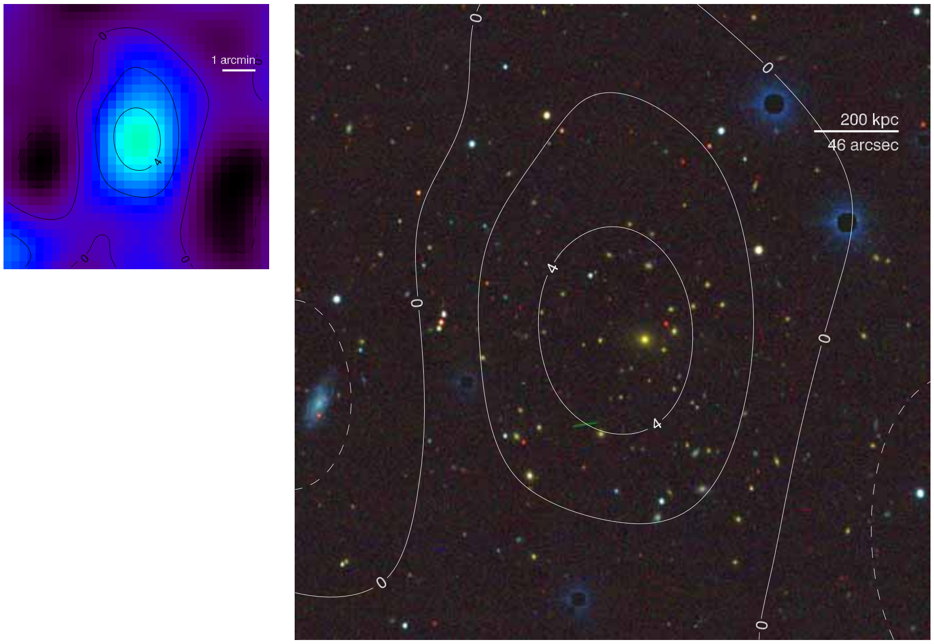

Figure 2.12: SPT-CL J2300-5331

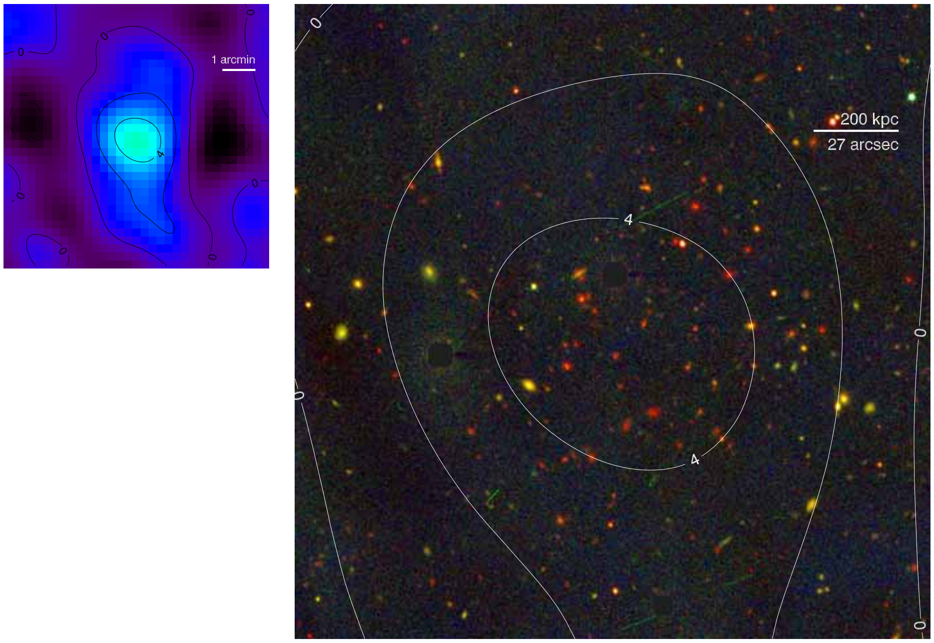

Figure 2.13: SPT-CL J2301-5546

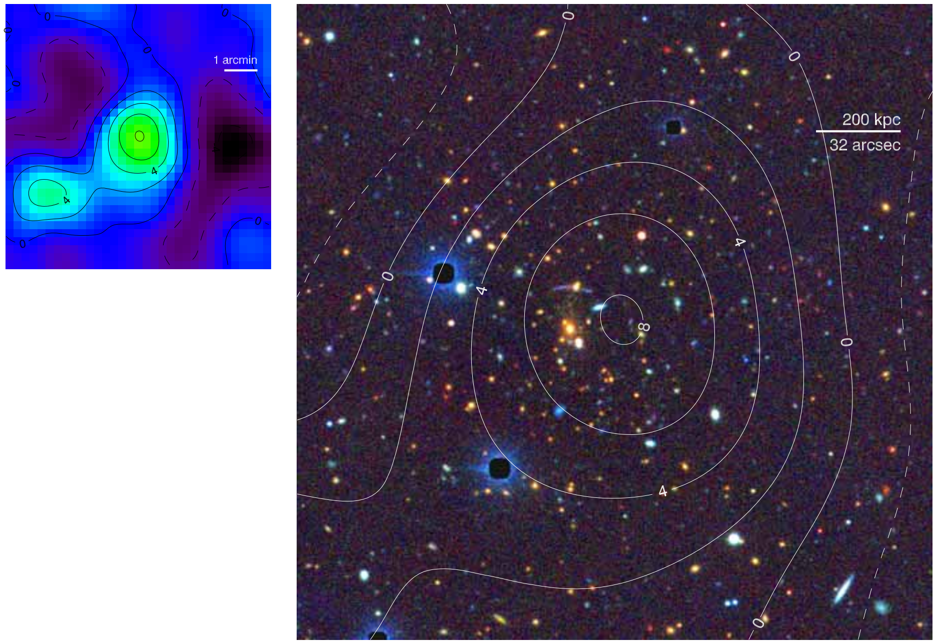

Figure 2.14: SPT-CL J2331-5051

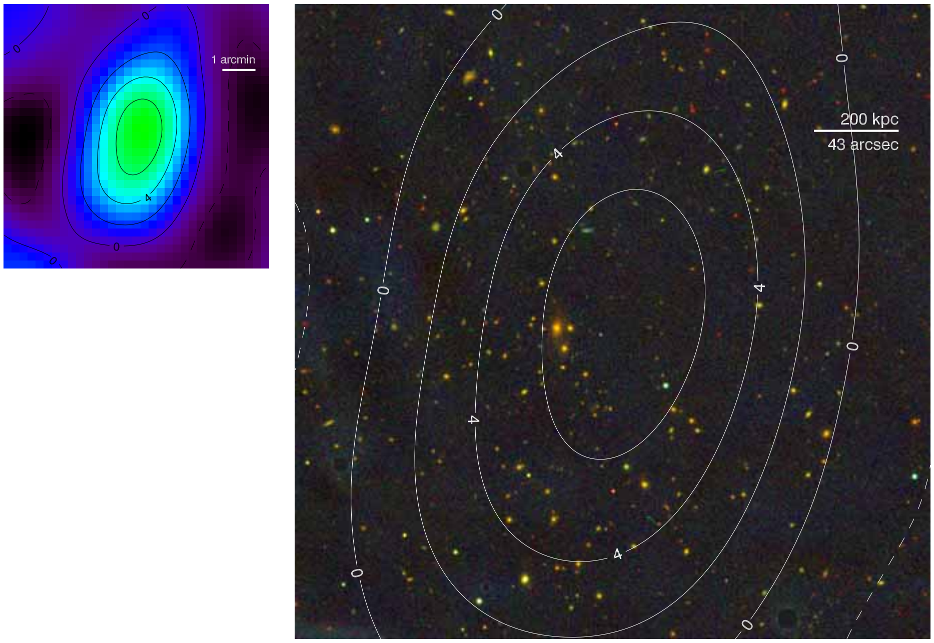

Figure 2.15: SPT-CL J2332-5358

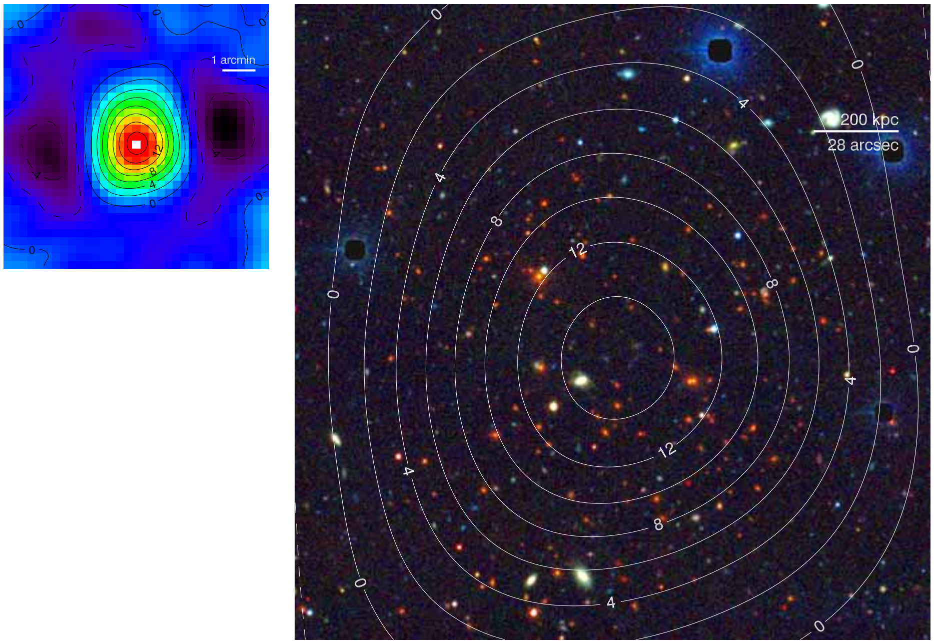

Figure 2.16: SPT-CL J2337-5942

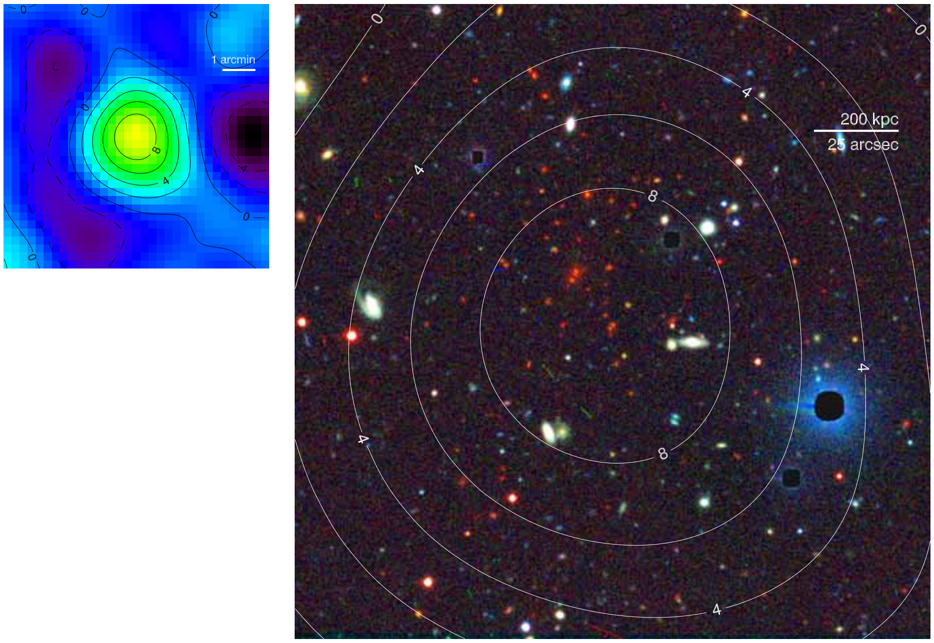

Figure 2.17: SPT-CL J2341-5119

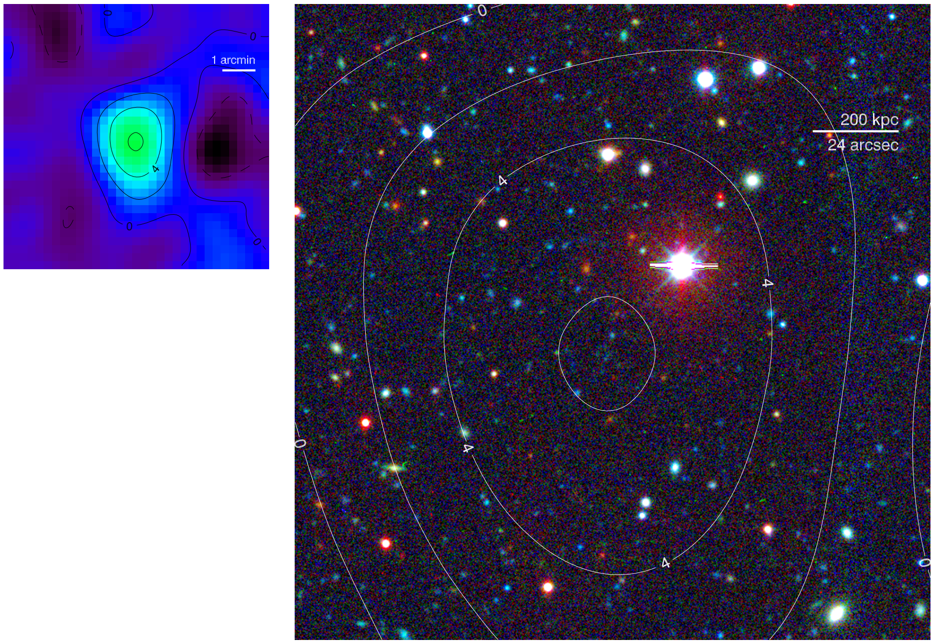

Figure 2.18: SPT-CL J2342-5411

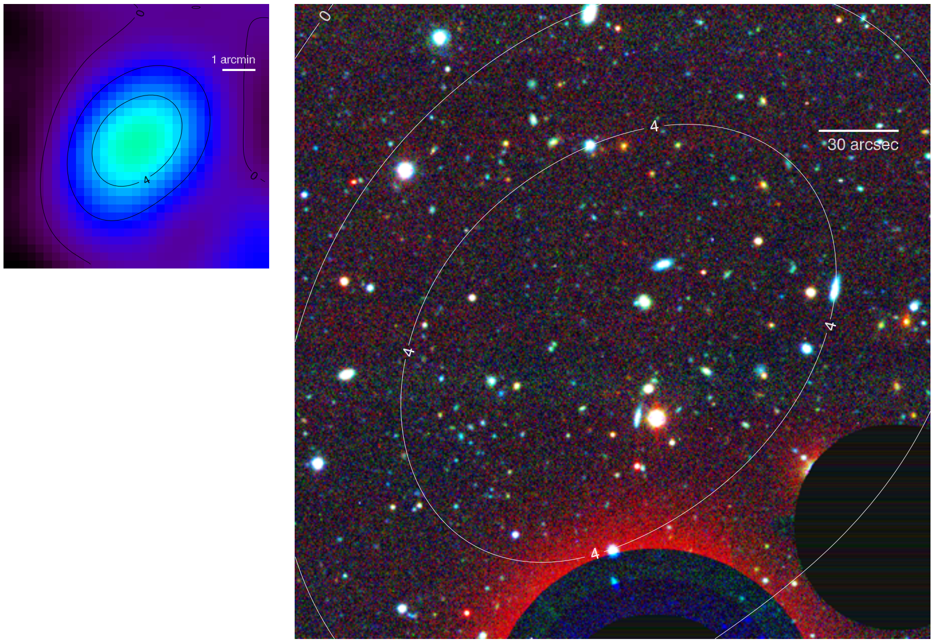

Figure 2.19: SPT-CL J2343-5521 (unconfirmed)

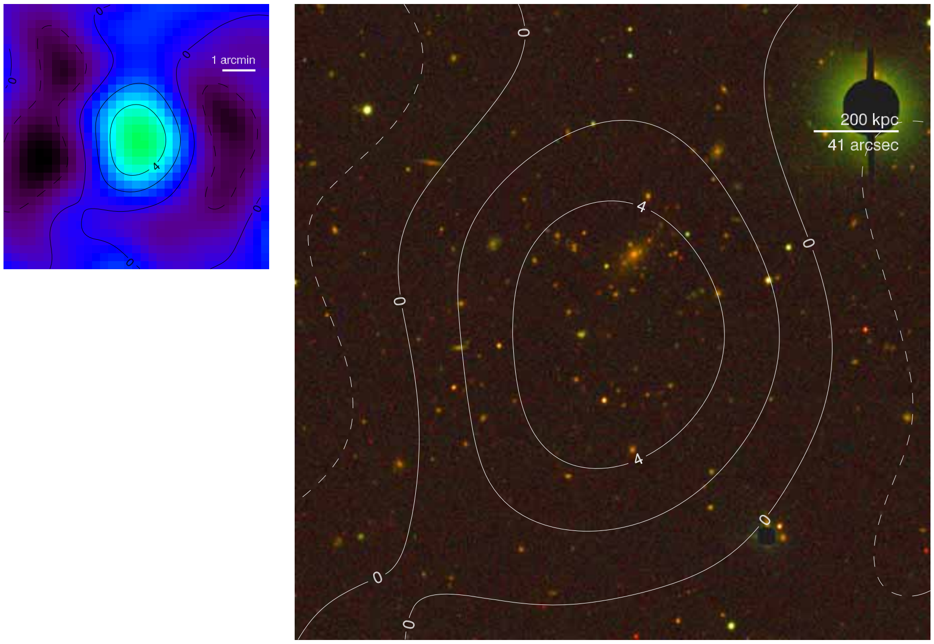

Figure 2.20: SPT-CL J2355-5056

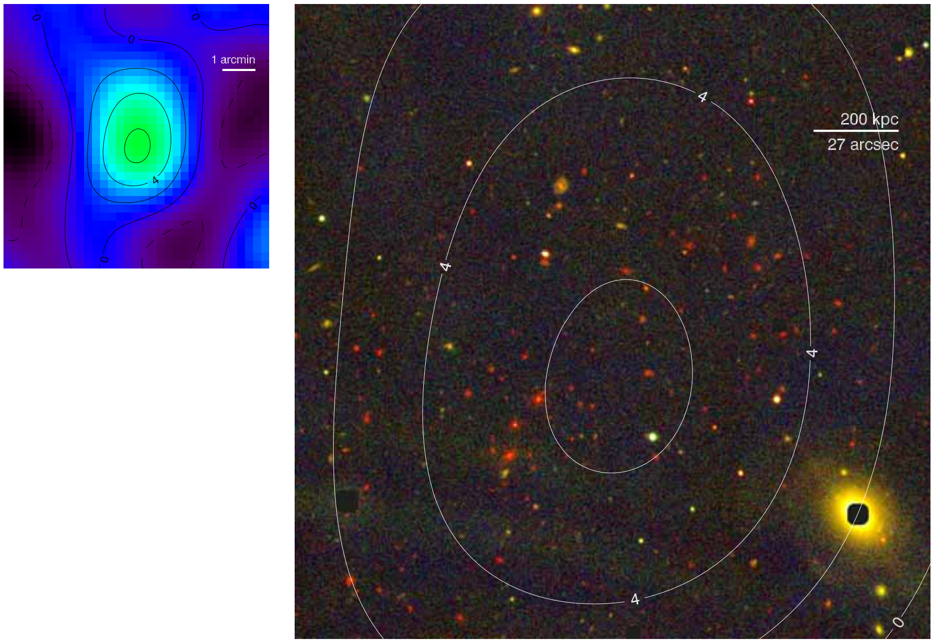

Figure 2.21: SPT-CL J2359-5009

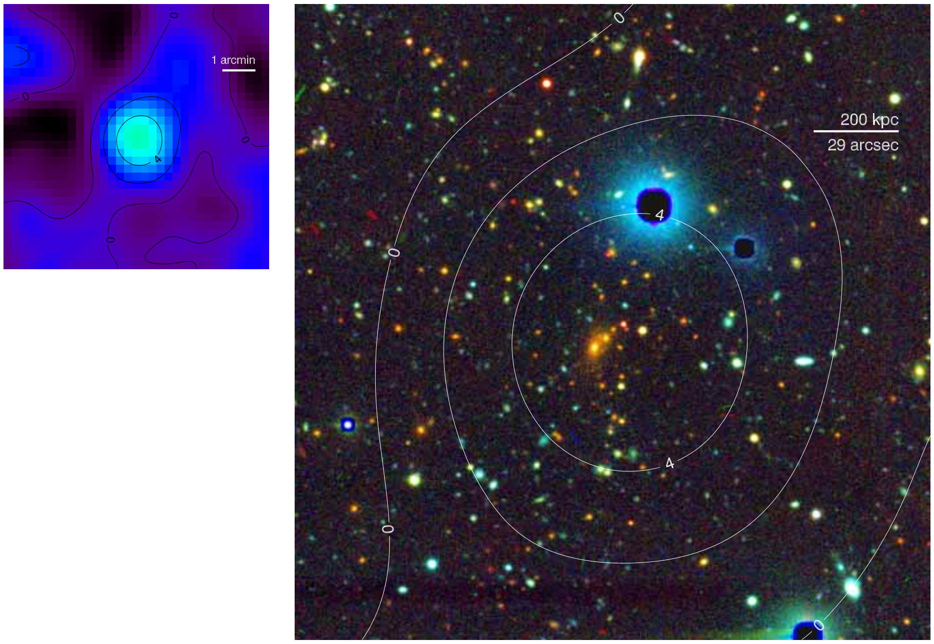

Figure 2.22: SPT-CL J0000-5748

2.2.3.2 Spectroscopy

Spectroscopic data were acquired with LDSS3 in long-slit mode for the purpose of measuring redshifts. Given limited telescope time for spectroscopy, we observed only a subset of the confirmed clusters. The subset was chosen to span the widest possible range in redshifts, so that we could assess the performance of our red-sequence redshift measurement methodology (see §2.3.2 and §2.4.1).

We obtained low-resolution spectra of galaxies in the field of 8 SPT clusters, using the VPH-Red and VPH-All grisms. The median seeing was about $0.7''$ and conditions were photometric. Standard CCD processing and 2D-spectrum extraction, with preliminary wavelength solutions, were accomplished with the COSMOS reduction package[2]; the 1D spectra were then extracted using the APALL task in IRAF. We employed our own IDL routines to flux calibrate the data and remove telluric absorption using the well-exposed continua of the spectrophotometric standards (Wade & Horne, 1988; Foley et al., 2003).

2.3 Analysis

We adopted a standard red-sequence model for optical cluster detection, photometric redshifts, and richness estimation. As previously introduced, spectroscopic data on about half the clusters were used to empirically correct the red-sequence model colors and then verify photometric red-sequence redshifts over a long redshift baseline.

---

[2] http://obs.carnegiescience.edu/Code/cosmos/

2.3.1 Red-Sequence Model

Red-sequence models were derived from the work of Bruzual & Charlot (2003), reflecting passively evolving, instantaneous-burst stellar populations with a formation redshift of $z = 3$, using Bertelli et al. (1994) evolutionary tracks and the Chabrier (2003) initial mass function. At each redshift, a range of metallicities was chosen by including a randomization in the metallicity-luminosity relation. The models were smoothed by linear fits in color-magnitude space at each redshift, and finally interpolated to arbitrary redshift using cubic splines.

We made an empirical correction to the model using the subsample of 10 clusters with spectroscopic data. After performing the red sequence peak finding (§2.3.2), we plotted red sequence redshifts against spectroscopic redshifts. The best fit line through the data was measured to have slope 0.89 ± 0.03 and y-intercept 0.04 ± 0.02. Model colors were then corrected by reassigning the model redshifts to be equal to the inverse of this linear relation. The effect of the model color correction is to leave redshifts near the pivot, $z \sim 0.4$, roughly unchanged, and to boost redshifts near ~ 1 by about $\Delta z = +0.07$, or $\Delta z = +3.5\%(1 + z)$. The resulting red-sequence model is shown in Figure 2.23.

2.3.2 Red-Sequence Finding and Redshifts

We confirm the existence of clusters by searching near the SZ cluster coordinate for a background-subtracted excess of red-sequence objects, effectively segregated by redshift. At each redshift step of size $\Delta z = 0.01$ in the range $0.1 < z < 1.4$, and with an aperture of $2'$ radius around the SZ coordinate, we select all objects with a

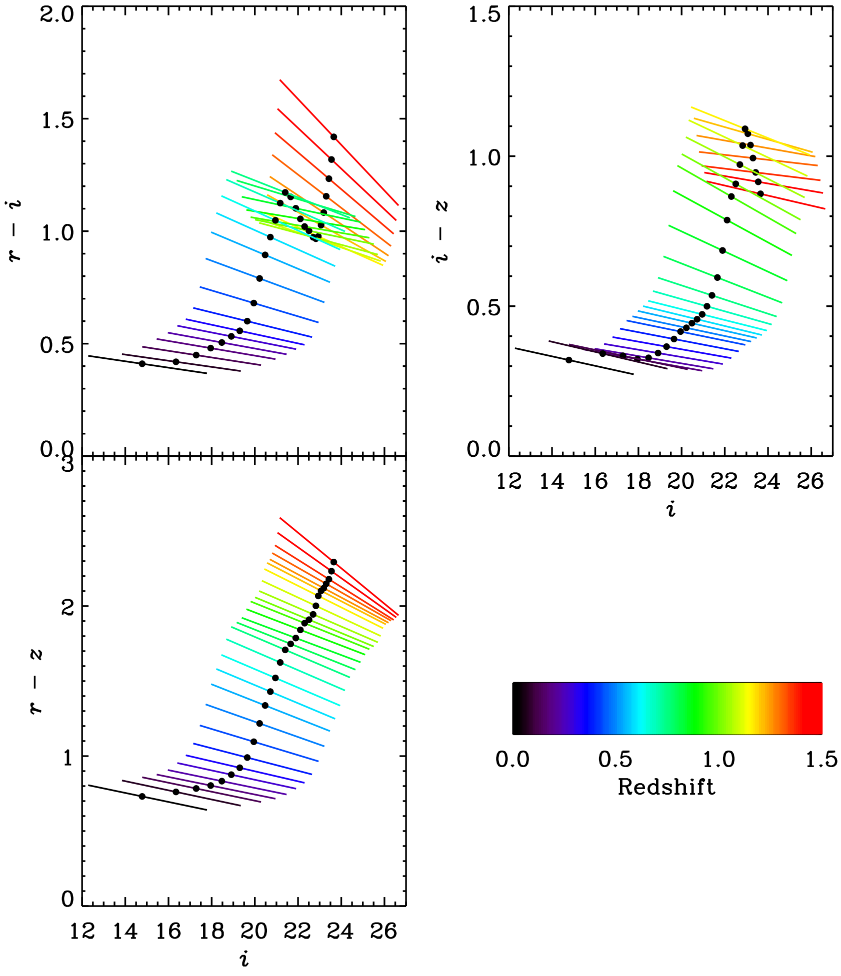

Figure 2.23: Red-sequence color-magnitude models as a function of redshift. Galaxy colors $r - i$ and $i - z$ were fit simultaneously in the red-sequence analysis, because that particular combination of colors (namely, $r - z = (r - i) + (i - z)$) allows for monotonic mapping from color to redshift over the widest redshift range ($0 < z \lesssim 1.4$) using optical wavelengths. The apparent i band magnitude of M^* at each redshift is denoted with the black points.

photometric signal-to-noise ratio > 5 in riz, whose $r - i$ and $i - z$ colors are also within 2σ of the red-sequence model line. The total uncertainty, e.g., for $r - i$, is defined as

$$\sigma^2 \equiv \sigma_{ri}^2 + \sigma_{ri}^{\mathrm{rs}2}, \tag{2.1}$$

and likewise for $i-z$. Here σ_{ri} (σ_{iz}) is the photometric uncertainty in $r-i$ ($i-z$) color of an object, and $\sigma_{ri}^{\mathrm{rs}}$ ($\sigma_{iz}^{\mathrm{rs}}$) is the intrinsic color scatter of the red sequence. These colors were chosen because their combination, $r-z = (r-i)+(i-z)$, increases monotonically over a long baseline of redshift, $0 < z \lesssim 1.4$. We assume $(\sigma_{ri}^{\mathrm{rs}}, \sigma_{iz}^{\mathrm{rs}}) = (0.05, 0.05)$ mag (Koester et al., 2007; Menci et al., 2008; Mei et al., 2009). The intrinsic scatter in color of cluster ellipticals alone is about two times smaller than this, and has been shown to be constant with redshift out to $z \approx 1.2$ (Menci et al., 2008; Mei et al., 2009). Morphological and spectral galaxy classification is beyond the scope of this work, and we assume our red sequence selections contain S0 galaxies in addition to ellipticals. This increases the color scatter and may also effectively induce redshift evolution due to evolving S0 populations; we ignore the latter effect, as the small number of clusters presented here is not sufficient to constrain redshift evolution.

We sum the selected galaxies, and normalize the counts by the projected area. This yields total surface density of all objects with colors consistent with the red-sequence model, within the $2'$ aperture, as a function of redshift, $\Sigma_{\mathrm{total}}(z)$. Uncertainties are estimated as the square root of counts, divided by the area.

The background red-sequence surface density is measured in a similar way. In the same set of riz exposures, we count red-sequence objects within many adjacent apertures of size $5' \times 5'$ over the entire field of view, excluding the $2'$ region around the SPT candidate position. The background surface density at each redshift, $\Sigma_{\rm background}(z)$, is calculated as the median of area-normalized counts from all apertures, and the uncertainty is the standard deviation divided by the square root of the total number of apertures. This approach is meant to minimize the contamination of the background signal by the red galaxies in the clusters themselves.

The red-sequence excess as a function of redshift is

$$\Sigma_{\rm net} = \Sigma_{\rm total} - \Sigma_{\rm background} \tag{2.2}$$

in units of galaxies per arcmin^2. We then renormalize the red sequence excess $\Sigma_{\rm net}$ in each redshift bin such that each galaxy contributes a *constant area* under the curve. The reason for this is that one galaxy may fall into multiple adjacent bins due to the size of color uncertainties, sometimes significantly widening the red-sequence peaks, especially for faint objects. The renormalization is a measure to mitigate this effect.

A cluster is detected if (1) there is an excess of red galaxies of the same apparent color in false color images, and (2) the galaxies corresponding to the maximum overdensity, $\Sigma_{\rm net}(z_{\rm max})$, are those identifiable in the false-color images. The cluster photometric redshift is taken to be $z_{\rm max}$. Figure 2.24 illustrates the process of red-sequence finding for one of the SZ clusters.

2.3.2.1 Completeness

We tested for completeness in red-sequence finding at representative BCS and Magellan depths. After constructing mock optical catalogs (Song et al. in prep.) containing simulated clusters of mass above $\sim 3 \times 10^{14}\, h^{-1}\, M_{\odot}$, we searched for red-sequence overdensities as we have described. Our estimated completeness is the frac-

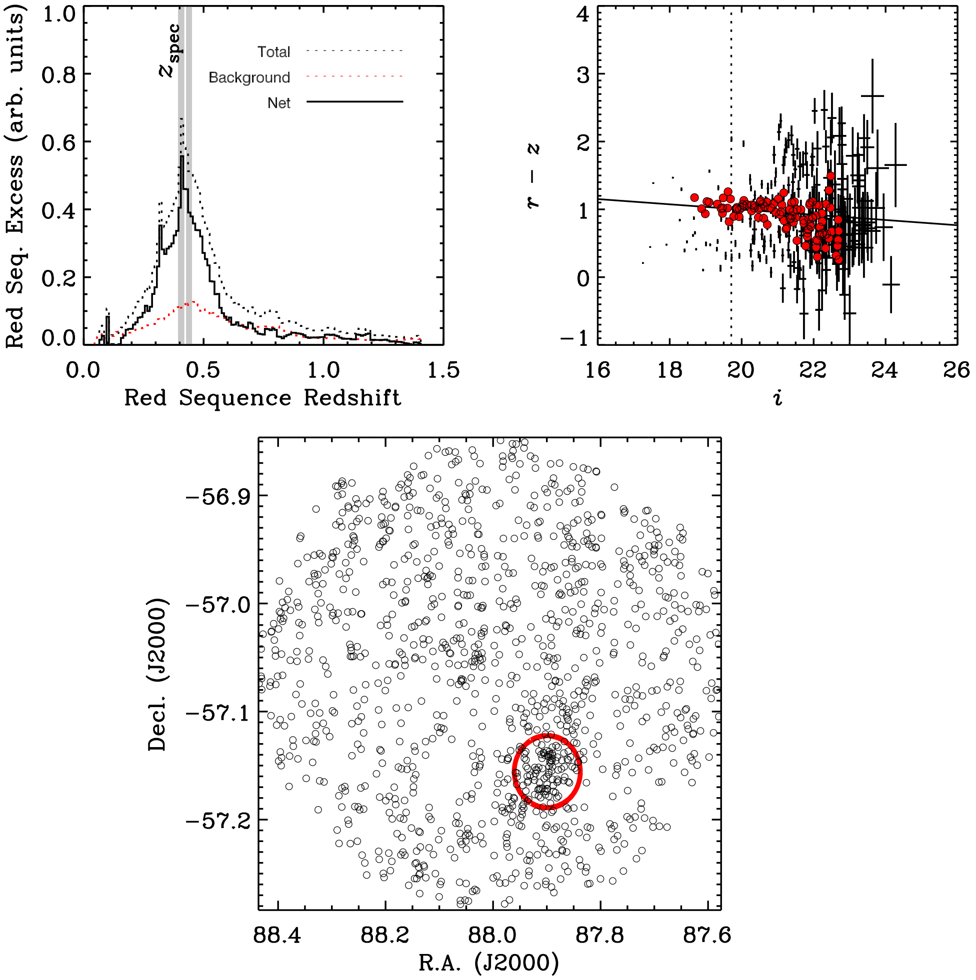

Figure 2.24: An illustration of red-sequence finding for the cluster SPT-CL J0551-5709 at $z_{\text{spec}} = 0.4230$. The top left plot shows the surface density of objects consistent within 2σ of the red-sequence model as a function of redshift. The peak occurs at redshift $z_{\max} = 0.41$, which is consistent with the spectroscopic redshift (vertical white line, with $\sigma_z = 2\%(1+z)$ uncertainty region shaded in gray for illustration). The color-magnitude diagram for all objects within $2'$ of the SPT coordinate is shown in the upper right, and the subsample of red-sequence objects at $z_{\max}$ shown as red points. The vertical dotted line is the model m^* at this redshift. Positions of all objects consistent with the $z_{\max}$ red sequence are shown in the bottom panel, where we have also circled the cluster aperture. A spatial overdensity of objects is clearly seen at the aperture.

tion of clusters recovered from the mock catalog. These mock catalogs include clusters with red and blue galaxy populations that are tuned to match the populations observed in real clusters (e.g., Lin et al., 2004). The galaxy distribution in space is determined using subhalo positions within high-resolution N-body simulations, and so the mock cluster spatial, kinematic and color signatures are a good match to those seen in real clusters.

The resulting selection function is shown in Figure 2.25. We recovered 100% of simulated clusters above the given mass threshold up to redshift 0.9. At this point the 4000 Å break begins to redshift out of the i band, making galaxies much harder to detect in $i - z$ color space. The completeness begins to fall here, and for these BCS and Magellan depths the probability of finding an optical counterpart above this mass threshold falls to zero by $z \approx 1.2$. Near-infrared photometry or much deeper space based optical photometry is required to push reliably to higher redshifts. But for the current sample only a single SPT cluster candidate was not confirmed using this multiband optical method.

2.3.3 $N_{\rm gal}$ and N_{200} Richness

After confirming a cluster and estimating its redshift, we measured the optical richness using a procedure that emulates the MaxBCG richness estimator (Koester et al., 2007), but adapted to high-redshift clusters. This began by again selecting objects with color within 2σ of the red-sequence line at redshift $z_{\rm max}$; luminosity brighter than $0.4L^*$ and fainter than the brightest cluster galaxy (BCG); and position within a projected radius of $R = 1\,h^{-1}\,{\rm Mpc}$ of the cluster center. We binned the

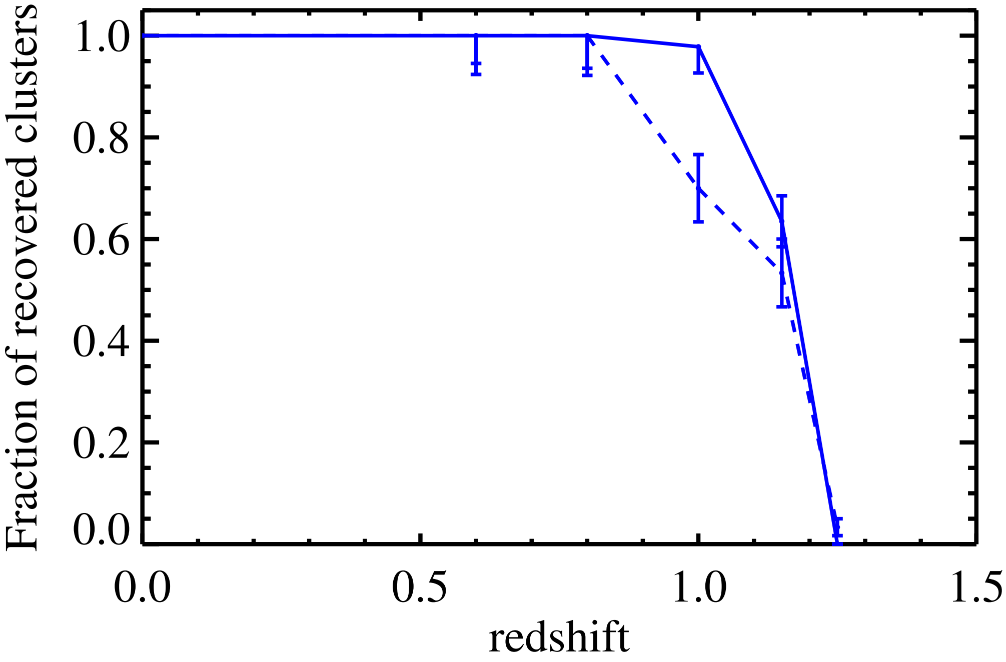

Figure 2.25: This shows the completeness of optical cluster finding from tests on a mock galaxy catalog with depth representative of the BCS survey (solid line) and Magellan imaging (dashed line). We have approximated Magellan data here as having limiting magnitudes ∼ 1 magnitude brighter than BCS.

selected objects in i band magnitude bins of size $\Delta m = 0.4$. We subtracted the background, as before, by performing the same procedure in many apertures on the sky away from the cluster but in the same exposures, and normalizing by projected area. The background was subtracted from the total red-sequence counts in each magnitude bin.

We then fitted Schechter luminosity functions (LF, Schechter, 1976) to the i band magnitudes of the selected objects:

$$\begin{aligned}\phi(m)\mathrm{d}m = 0.4\ln(10)\phi^{*}10^{-0.4(m-m^{*})(\alpha+1)} \\ \times \exp\left[-10^{-0.4(m-m^{*})}\right]\mathrm{d}m,\end{aligned} \tag{2.3}$$

where m^{*} is the characteristic magnitude of the LF, α is the faint-end slope, and ϕ^{*} is the normalization. Our photometry was not uniformly complete on all clusters with respect to m^{*}, so our ability to constrain the slope was weak. We therefore fixed $\alpha = -1$, which has been shown to be reasonable for the most massive MaxBCG clusters (Lin & Mohr, 2003; Hansen et al., 2005; Rudnick et al., 2009; Crawford et al., 2009). We tested fixing m^{*} at each redshift using our passive model, and leaving it free. For those clusters for which the luminosity function was well constrained, we measured values consistent with the model, and we ultimately chose to fix this parameter at each redshift. This is in agreement with the detailed LF studies of Zenteno et al. (in prep) on a subset of these clusters. The faint-end slope α has been shown to evolve with redshift (Rudnick et al., 2009), however, such studies must be performed at magnitudes fainter than $m^{*}+1$. We test varying α by ± 0.3, and find our richness results are largely unaffected to within our uncertainties. Because we integrate only to $m^{*}+1$ there is only weak sensitivity to the adopted faint-end slope.

We fit the LF only at magnitudes brighter than our limiting magnitude and fainter than the BCG. Limiting magnitudes are estimated to be the faintest magnitude bin before which the red-sequence background becomes incomplete, as indicated by a deviation from linearity in the logarithmic i band magnitude distribution of red-sequence galaxies. We also assess photometric completeness using simulated point sources in our cluster images. We determine that we recover 90% of simulated objects in images at *all magnitudes* brighter than the above-defined limiting magnitude. The majority of unrecovered objects are lost to pixel masking due to bright stars and to object crowding. We make a generic correction by this amount in all magnitude bins, the effect of which is to increase $N_{\rm gal}$ estimates by 0.9^{-1}. The analytic LF is then integrated down to $m^* + 1$. The resulting integration is an estimate of $N_{\rm gal}$, which is the number of red sequence galaxies within $1\,h^{-1}\,$Mpc of the cluster center, above a fixed luminosity threshold.

We stress that the LF fitting step deviates from the MaxBCG procedure, but it is necessary because our photometry is not complete to $0.4L^*$ on all clusters. Our fitting and extrapolating the LF of fairly bright, red-sequence satellite galaxies is physically reasonable because it is known that the luminosity function of such members of massive clusters is only very weakly dependent on mass and is well described by a Schechter function from lower redshifts (Hansen et al., 2009) to redshifts close to unity (Gilbank et al., 2008). Figure 2.26 illustrates the resulting LF fit for one of the SPT clusters.

R_{200} is estimated from $N_{\rm gal}$ using the empirical $N_{\rm gal}$–R_{200} relation of Hansen et al.

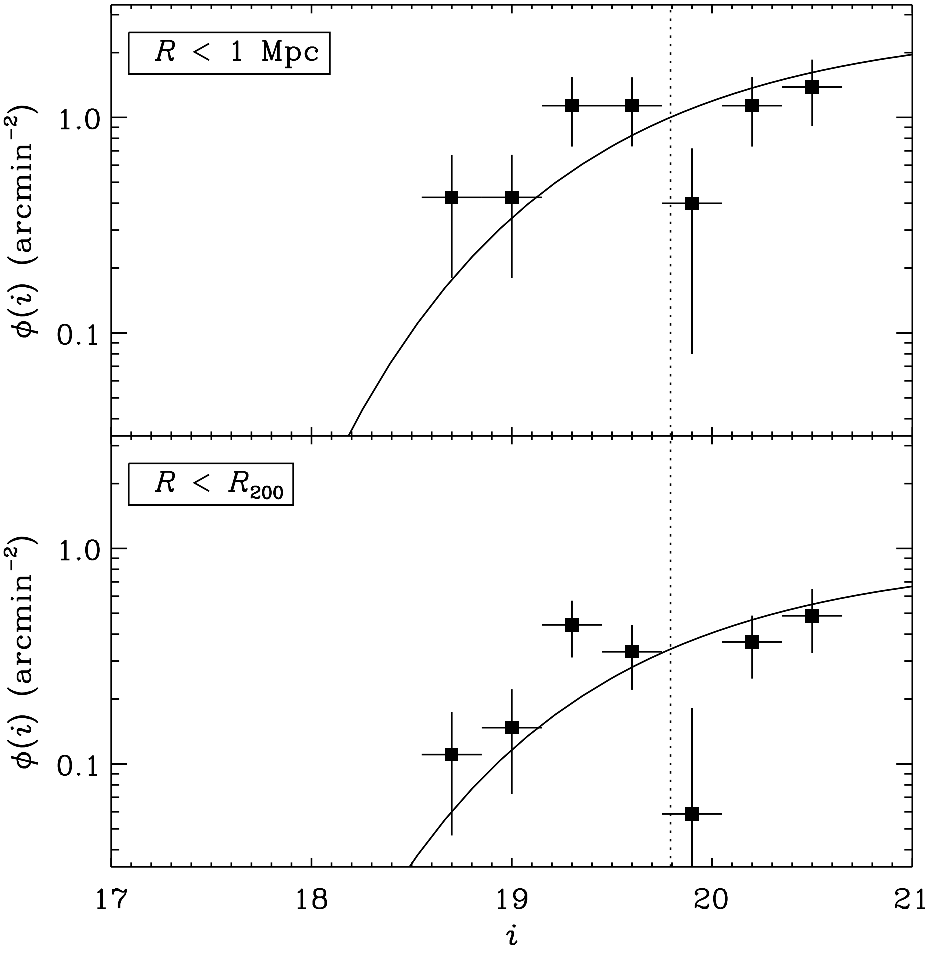

Figure 2.26: An illustration of luminosity function fitting for SPT-CL J0551-5709. We use our passively evolving model to fix m^* to 19.77 mag (vertical dotted line), and integrate down to $m^* + 1$ to estimate N_{gal} (top panel) and N_{200} (bottom panel). R_{200} is estimated from N_{gal}, as described in the text.

(2005),

$$R_{200} = 0.156 N_{\rm gal}^{0.6}\, h^{-1}\,{\rm Mpc}. \tag{2.4}$$

This relation was measured from the MaxBCG cluster sample, which ranged in redshift from 0.1 to 0.3 and had a median mass of about $1 \times 10^{14}\, h^{-1}\, M_\odot$. The clusters we present in this work are mostly above this redshift range, and expected to have higher median mass (see V10, §2.4.2). Nonetheless, we adopt this relation to estimate cluster radii, and leave verification of the relation on an SZ selected sample such as this to future work.

The entire richness procedure is repeated, now setting $R = R_{200}$ instead of $1\, h^{-1}\,{\rm Mpc}$, to arrive at an estimate of N_{200}. N_{200} is then used to estimate cluster mass using previously established empirical relations, which we now outline.

2.3.3.1 Mass-Richness Scaling and Scatter

By comparing to weak gravitational lensing masses, N_{200} richness has been shown by Reyes et al. (2008) to scale with M_{200}, the cluster mass contained within a sphere that has an average mass density of 200 times the universal average, as

$$\frac{M_{200}}{10^{14} h^{-1}\, M_\odot} = (1.42 \pm 0.08) \left(\frac{N_{200}}{20}\right)^{1.16 \pm 0.09} . \tag{2.5}$$

Earlier, Johnston et al. (2007) presented a similar, independent weak lensing study, and their relation (normalization 0.88 ± 0.12, power law 1.28 ± 0.04) differs from Equation (2.5) by about 30% in mass at $5 \times 10^{14}\, h^{-1}\, M_\odot$. We adopt Equation (2.5) as our mass-richness scaling relation with overall uncertainty of 30%.

Scatter in M_{200} at fixed $N_{200} = 40$ as determined from weak lensing and X-ray cluster masses is $\sigma_{M|N} = 45\% \pm 20\%$ (95% CL, Rozo et al., 2009).

If richness quantities scale as

$$M_{200} \sim N_{200}^{1/\alpha} \sim N_{\rm gal}^{1/(\alpha\beta)} = N_{\rm gal}^{1/0.56} \sim R_{200}^3, \tag{2.6}$$

where α is the N_{200}–M_{200} power law and β is the $N_{\rm gal}$–N_{200} power law, then $\alpha = 0.86$ and $\beta = 0.65$, using results of Equations (2.4) and (2.5). Scatter of 45% (60%) in mass translates to scatter of 39% (52%) in N_{200}, 25% (34%) in $N_{\rm gal}$, and 15% (20%) in R_{200}.

As with the $N_{\rm gal}$–R_{200} relation (Equation (2.4)), these N_{200}–M_{200} mass relations were determined from weak lensing measurements of MaxBCG clusters in SDSS, a sample that was deemed to be complete at redshifts $0.1 < z < 0.3$, with median mass of approximately $1 \times 10^{14}\, h^{-1}\, M_\odot$. Our SZ selected cluster sample has a significantly broader redshift distribution, as well as a median mass about five times larger. Red galaxies are known to be biased tracers of dark matter, and the bias is a function of mass, redshift, and radius. Given the small size of our sample and the large intrinsic uncertainties inherent to richness techniques, we assume our data are insensitive to deviations from these fiducial relations, and we leave the study of the evolution of red galaxy populations with larger SZ cluster samples to future work.

2.3.3.2 Statistical Richness Uncertainties

We estimated statistical uncertainties on $N_{\rm gal}$ and N_{200} by bootstrapping (Efron, 1979) the entire richness procedure thousands of times. In particular, we assumed that the statistically limiting step in our procedure was the luminosity function fitting to the binned magnitude data. Therefore, the start of the bootstrap process was a random resampling of the magnitude bins themselves. For each realization, we re-fitted the luminosity function, integrated to obtain N_{gal}, and estimated R_{200}. We independently bootstrapped the LF fitting for N_{200} estimation as well. Parameters were assigned as the biweight means (Beers et al., 1990) of bootstrap distributions, and sample uncertainties as the biweight standard deviations.

2.3.4 Spectroscopic Redshifts

For each galaxy spectrum, the redshift was found by cross-correlating with the FABTEMP97 template, using the RVSAO package in IRAF (Kurtz & Mink, 1998). The validity of the cross-correlation redshift was checked by visual inspection and judged by the presence of visible absorption (and in a few cases, emission) lines. Redshift uncertainties were estimated as two times those given by RVSAO for the BCG redshifts, or the biweight interval estimator (Beers et al., 1990) for the other cases. We discard non-galactic spectra as well as redshifts in strong disagreement with the ensemble average or our prior photometric redshift estimate. The redshift adopted for each cluster is the median redshift of the galaxies passing all cuts.

2.4 Results

2.4.1 Redshifts

We list redshift results in Table 2.1. Figure 2.27 is a plot of red sequence redshifts versus spectroscopic redshifts for clusters on which we have both measurements. The line we fitted to uncorrected redshifts, which were used to empirically calibrate the red-sequence model colors (§2.3.1), is the dashed line in the figure. After the correction, we verify that the red sequence redshifts are unbiased to within the uncertainties. Root-mean-square scatter in redshift per cluster is $\sigma_z = 0.02(1+z)$, with maximum absolute deviation of $0.05(1+z)$. We therefore generically assign random uncertainties of 2% to all redshifts in the range we have directly tested, $0.15 < z < 1$. For redshifts estimated to be > 1, we assign 5% uncertainties in order to effectively rule out redshifts less than 1. Finally, for clusters at $z < 1$ where our photometric uncertainties are large, we also generically increase the uncertainty estimates.

Table 2.1: Cluster Redshift Data

Cluster Name	z_{rs}	z_{spec}	N_{spec}	Imaging Coverage	
				BCS?	Magellan?
SPT-CL J0509-5342	0.47(3)	0.4626(4)	6	Y	Y
SPT-CL J0511-5154	0.74(3)	···	···	N	Y
SPT-CL J0516-5430	0.25(3)	0.2952	8	Y	Y
SPT-CL J0521-5104	0.72(3)	···	···	Y	N
SPT-CL J0528-5259	0.75(4)	0.7648(5)	2	Y	Y
SPT-CL J0533-5005	0.83(4)	0.8810(9)	4	N	Y
SPT-CL J0539-5744	0.77(4)	···	···	N	Y
SPT-CL J0546-5345	1.16(11)	···	···	Y	N
SPT-CL J0551-5709	0.41(3)	0.4230(10)	5	N	Y
SPT-CL J0559-5249	0.66(3)	0.6112(3)	5	N	Y

Continued on next page…

Table 2.1 – Continued

Cluster Name	z_{rs}	z_{spec}	N_{spec}	Imaging Coverage	
				BCS?	Magellan?
SPT-CL J2259-5617	0.16(2)	0.1528	1	N	Y
SPT-CL J2300-5331	0.29(3)	···	···	N	Y
SPT-CL J2301-5546	0.78(9)	···	···	N	Y
SPT-CL J2331-5051	0.55(3)	0.5707(5)	8	N	Y
SPT-CL J2332-5358	0.32(3)	···	···	Y	Y
SPT-CL J2337-5942	0.77(4)	0.7814(5)	2	N	Y
SPT-CL J2341-5119	1.03(4)	0.9983(5)	1	N	Y
SPT-CL J2342-5411	1.08(10)	···	···	Y	N
SPT-CL J2332-5521	···	···	···	Y	Y
SPT-CL J2355-5056	0.35(3)	···	···	N	Y
SPT-CL J2359-5009	0.76(4)	···	···	N	Y
SPT-CL J0000-5748	0.74(9)	···	···	N	Y

2.4.2 Richness

In Figure 2.28 we compare our richness-derived masses to those presented in V10, which were estimated from SPT millimeter-wavelength data. We label V10 masses as

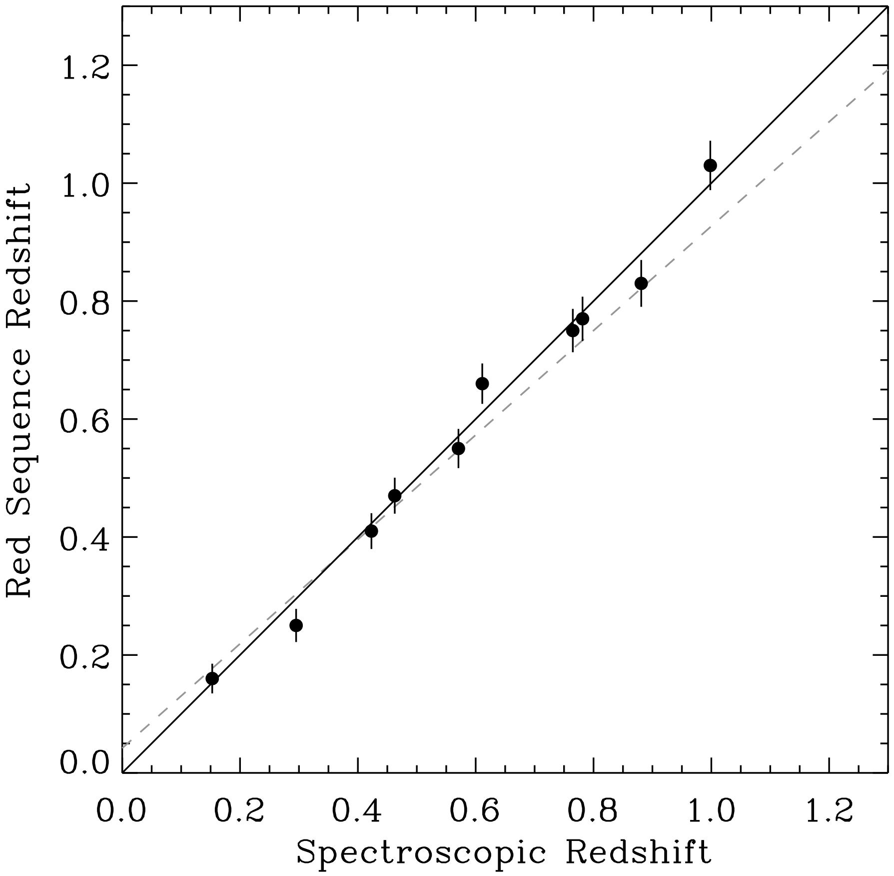

Figure 2.27: Spectroscopic versus red-sequence redshifts. We have applied an empirical linear correction to the red-sequence model colors using this sample, and this plot shows the result of red-sequence redshift measurements after the model correction. The best fit line to the uncorrected redshifts is the dashed line, shown for comparison. Typical RMS redshift scatter is about 2% in $\sigma_z/(1+z)$. Redshift estimates for the entire sample are presented in Table 2.1.

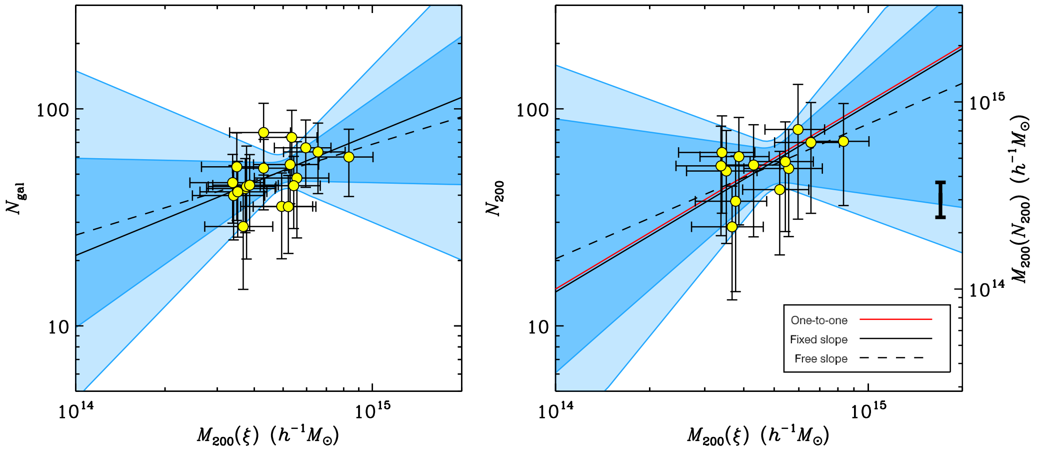

Figure 2.28: Optical richness versus total cluster mass estimated from the SPT data. This plot shows that the richness correlates highly with this millimeter-wavelength mass-observable (taken from Vanderlinde et al., 2010), and together the data agree with previously established scaling relations to within the uncertainties. The solid red line in the right-hand panel is the one-to-one mass relation, and the solid black lines in both panels are best-fit relations when fixing the slope to previously measured values. The dashed lines are best-fit relations leaving both slope and intercept free. The dark, inner shaded areas denote the 68% confidence regions assuming zero intrinsic richness-mass scatter for the two parameter regression. The light, outer shaded areas denote 68% confidence regions assuming 35% scatter in mass, which is a better match to the data. The heavy error bar on the far right-hand side indicates the nominal overall uncertainty of 30% in the N_{200}–M_{200} relation.

$M(\xi)$, because they are calculated from the SZ signal-to-noise ratio ξ. The purpose of the comparison is to assess the level of correlation and explore whether the power law and normalization of the scaling laws are consistent with previous work. We additionally estimate the normalization of $N_{\rm gal}$, which we treat as an empirical mass observable in its own right rather than only as a measurement intermediate to N_{200}.

Richness and $M(\xi)$ are plotted against one another in Figure 2.28. We have used Equation (2.5) to render the far right-hand mass axis, with the 30% overall uncertainty in this relation denoted with the heavy error bar. We do not display a mass axis in the $N_{\rm gal}$ panel of the figure because there have been no previous measurements of an $N_{\rm gal}$–M_{200} scaling relation.

We perform the analysis only considering clusters whose radius (R_{200} in the case of N_{200}, $1\,h^{-1}\,$Mpc in the case of $N_{\rm gal}$) falls fully within the observed field of view. For Magellan IMACS imaging this limited radii to $\lesssim 6'$, because we placed the SPT center in the middle of one of the eight chips, at a distance of about six arcminutes from the field edge. Spatial incompleteness of this kind does not affect the BCS data.

2.4.2.1 $N_{\rm gal}$ Scaling

R_{200} for massive clusters is approximately $1.5\,h^{-1}\,$Mpc, which subtends $\gtrsim 6'$ at redshifts $z \lesssim 0.3$. We find it useful to count red galaxy overdensities in a smaller region, corresponding to $1\,h^{-1}\,$Mpc in co-moving coordinates, which subtends $\gtrsim 6'$ at redshifts $z \lesssim 0.17$. This is a better match to the observed typical angular size of the SZ signal. In addition, the surface density of red galaxies in the smaller aperture is greater than for R_{200}, whose larger area effectively dilutes the signal. For these reasons we explore $N_{\rm gal}$ as an empirical mass proxy.

As argued in § 2.3.3.1, $N_{\rm gal}$ should scale with mass as $M_{200}^{0.56}$. We fix this slope and measure

$$N_{\rm gal} = (52 \pm 3 \pm 9)\left(\frac{M_{200}}{5\times 10^{14}\,h^{-1}\,M_\odot}\right)^{0.56}, \tag{2.7}$$

If zero intrinsic scatter is assumed, the reduced chi-square of the fit is $\chi^2_\nu \approx 3$, whereas 20% in $N_{\rm gal}$ (corresponding to $\sim 35\%$ in mass) produces $\chi^2_\nu = 1$. The first error given in Equation (2.7) is random-only, which includes the intrinsic mass-richness scatter, and the second error is the overall systematic uncertainty of 30%. This fit is shown as the solid black line in the left-hand panel of Figure 2.28.

Letting the slope be free, we measure a normalization consistent with Equation (2.7) and slope 0.42±0.50. This is the dashed line in the left-hand panel of Figure 2.28. In the figure, the inner, dark shaded area denotes the 68% confidence region for the best two-parameter fit assuming zero intrinsic scatter, while the outer, light shaded area is the 68% confidence region for best two-parameter fit assuming 35% intrinsic mass scatter, which is a significantly better match to the data. We estimate the uncertainty on intrinsic scatter by varying it until the chi-square doubles, resulting in relative 1σ uncertainty at the $\sim 50\%$ level.

2.4.2.2 N_{200} Scaling

We perform the same analysis on N_{200}. Fixing the mass-mass slope to unity, we measure

$$N_{200} = (57 \pm 4 \pm 15) \left(\frac{M_{200}}{5 \times 10^{14}\, h^{-1}\, M_\odot} \right)^{0.86} . \tag{2.8}$$

Again, 35% intrinsic mass scatter, corresponding to 30% scatter in N_{200}, gives $\chi^2_\nu = 1$. This fit is shown as the black line in right-hand panel of Figure 2.28, and can be compared to the one-to-one mass line, in red.

Letting the slope be free, the measured normalization consistent with Equation (2.8) and slope 0.62 ± 0.73. This is shown with the dashed black line in Figure 2.28. As before, the dark, inner shaded region is the 68% confidence region for the best two-parameter fit assuming zero intrinsic scatter, while the outer, light shaded area is the 68% confidence region for best two-parameter fit assuming 35% intrinsic mass scatter, which is a significantly better match to the data. Relative uncertainty on the intrinsic scatter is comparable to that quoted above for $N_{\rm gal}$.

All richness results are given in Table 2.2. In the table we have adopted Equation (2.5) to estimate masses from N_{200}, and for $N_{\rm gal}$ masses we have used Equation (2.7). Systematic uncertainties are taken to be the quadrature sum of the nominal 45% intrinsic scatter in mass (§2.3.3.1) and the 30% overall uncertainty in the richness–mass scaling relation. Further work on a larger sample of clusters selected with similar criteria as these is needed to reduce statistical uncertainties and measure the scatter directly. We discuss the implications of our richness measurements in §3.5.

Table 2.2: Cluster Richness Data

Cluster Name	${N_{\rm gal}}^{\rm a}$	$M_{200}(N_{\rm gal})^{\rm b}$ $(10^{14}h^{-1}\,M_\odot)$	${R_{200}}^{\rm a}$ $(h^{-1}{\rm Mpc})$	${N_{200}}^{\rm a}$	$M_{200}(N_{200})^{\rm b}$ $(10^{14}h^{-1}\,M_\odot)$
SPT-CL J0509-5342	41(8)	$3.3 \pm 2.0 \pm 1.0$	1.46(17)	51(13)	$4.3 \pm 2.5 \pm 1.3$
SPT-CL J0511-5154	77(12)	$10.3 \pm 5.9 \pm 3.1$	2.13(20)	…	…
SPT-CL J0516-5430	…	…	…	…	…
SPT-CL J0521-5104	44(7)	$3.7 \pm 2.2 \pm 1.1$	1.52(15)	57(13)	$4.8 \pm 2.7 \pm 1.4$
SPT-CL J0528-5300	44(9)	$3.8 \pm 2.3 \pm 1.1$	1.52(18)	60(13)	$5.1 \pm 2.8 \pm 1.5$
SPT-CL J0533-5005	28(10)	$1.7 \pm 1.4 \pm 0.5$	1.17(25)	28(6)	$2.2 \pm 1.2 \pm 0.6$
SPT-CL J0539-5744	63(9)	$7.1 \pm 4.0 \pm 2.1$	1.88(16)	69(14)	$6.1 \pm 3.3 \pm 1.8$
SPT-CL J0546-5345	66(7)	$7.7 \pm 4.1 \pm 2.3$	1.93(12)	80(31)	$7.1 \pm 4.8 \pm 2.1$
SPT-CL J0551-5709	54(15)	$5.4 \pm 3.8 \pm 1.6$	1.71(29)	…	…
SPT-CL J0559-5249	59(6)	$6.5 \pm 3.4 \pm 1.9$	1.82(11)	70(8)	$6.2 \pm 3.2 \pm 1.8$

Continued on next page…

Table 2.2 – Continued

Cluster Name	N_{gal}[a]	$M_{200}(N_{\mathrm{gal}})$[b] $(10^{14}h^{-1}\,M_\odot)$	R_{200}[a] $(h^{-1}\mathrm{Mpc})$	N_{200}[a]	$M_{200}(N_{200})$[b] $(10^{14}h^{-1}\,M_\odot)$
SPT-CL J2259-5617	$\cdots$	$\cdots$	$\cdots$	$\cdots$	$\cdots$
SPT-CL J2300-5331	35(10)	$2.5 \pm 1.8 \pm 0.8$	1.33(22)	$\cdots$	$\cdots$
SPT-CL J2301-5546	35(8)	$2.5 \pm 1.6 \pm 0.8$	1.33(17)	42(6)	$3.4 \pm 1.8 \pm 1.0$
SPT-CL J2331-5051	73(5)	$9.4 \pm 4.8 \pm 2.8$	2.06(8)	$\cdots$	$\cdots$
SPT-CL J2332-5358	42(8)	$3.5 \pm 2.1 \pm 1.1$	1.49(16)	$\cdots$	$\cdots$
SPT-CL J2337-5942	53(8)	$5.2 \pm 2.9 \pm 1.6$	1.69(15)	55(11)	$4.6 \pm 2.5 \pm 1.4$
SPT-CL J2341-5119	39(7)	$3.1 \pm 1.9 \pm 0.9$	1.42(16)	62(7)	$5.4 \pm 2.8 \pm 1.6$
SPT-CL J2342-5411	43(19)	$3.7 \pm 3.4 \pm 1.1$	1.51(38)	37(12)	$2.9 \pm 1.8 \pm 0.9$
SPT-CL J2355-5056	55(5)	$5.6 \pm 3.0 \pm 1.7$	1.73(10)	$\cdots$	$\cdots$
SPT-CL J2359-5009	47(16)	$4.3 \pm 3.4 \pm 1.3$	1.59(32)	53(8)	$4.4 \pm 2.3 \pm 1.3$

Continued on next page. . .

Table 2.2 – Continued

Cluster Name	$N_{\rm gal}$[a]	$M_{200}(N_{\rm gal})$[b] $(10^{14}h^{-1}\,M_\odot)$	R_{200}[a] $(\,h^{-1}{\rm Mpc})$	N_{200}[a]	$M_{200}(N_{200})$[b] $(10^{14}h^{-1}\,M_\odot)$
SPT-CL J0000-5748	45(6)	$4.0 \pm 2.2 \pm 1.2$	1.55(12)	54(11)	$4.6 \pm 2.5 \pm 1.4$

---

[a] Uncertainties given are statistical only.

[b] Uncertainties given are statistical and systematic, respectively.

2.4.3 Notable Clusters

In this section we describe notable information, if any, about the clusters. As we will point out, a subset of clusters also appear in the catalogs of A89, Böhringer et al. (2004a), S09, Menanteau & Hughes (2009, hereafter MH09), Menanteau et al. (2009, hereafter M09), and Menanteau et al. (2010, hereafter M10). Our redshifts agree to within $\sigma_z \approx 3\%(1+z)$ of the photometric redshifts presented in M09 and M10, except for the highest redshift cluster from S09, SPT-CL J0546-5345 (see below). Because we have not presented exhaustive optical cluster-finding in the entire BCS survey in this work, instead having concentrated on fields in the direction of the SZ detections, and because the number of overlapping clusters is too small to draw useful conclusions with high statistical confidence, we leave a formal inter-comparison of redshift and richness results of M09 and M10 to future studies.

SPT-CL J0509-5342 This cluster was previously identified by S09.

SPT-CL J0511-5154 This cluster has recently been identified by M10, who assigned the name SCSO J051145-515430.

SPT-CL J0516-5430 This cluster was previously identified by S09, where it was called by a different name, SPT-CL J0517-5430. The SPT name ascribed to this object in this work and in V10 follow the recommendations of the International Astronomical Union (IAU), and should be adopted permanently. This cluster also identified as Abell S0520 (Abell et al., 1989a, hereafter A89), and RXCJ0516.6-5430 (Böhringer et al., 2004a), the latter of which is the source of the spectroscopic redshift. M10 detected this object and call it SCSO J051637-543001.

SPT-CL J0521-5104 This cluster has been identified by M10 as SCSO J052113-510418.

SPT-CL J0528-5300 This cluster was previously identified by S09, where it was called by the same name, and was also identified by M10 as SCSO J052803-525945.

SPT-CL J0539-5744 This cluster displays a possible strong gravitational lens arc.

SPT-CL J0546-5345 This cluster was previously identified by S09, where it was called by a different name, SPT-CL J0547-5345. The SPT name ascribed to this object in this work and in V10 follow the recommendations of the IAU, and should be adopted permanently. S09 reported a photometric redshift of ~ 0.9 and M09 independently reported $z_{\rm photo} = 0.88^{+0.08}_{-0.04}$. We do not detect a red-sequence overdensity near redshift 0.9, but a faint red-sequence peak is evident at $z_{\rm rs} \approx 1.15$.

SPT-CL J0551-5709 Abell S0552 (A89) is in the foreground of this cluster. No redshift estimate exists for Abell S0552, but a strong red sequence at $z_{\rm rs} = 0.09$ is clearly visible in color-magnitude diagrams. The SPT cluster identified here, however, is measured at $z = 0.42$.

SPT-CL J0559-5249 Our red-sequence studies reveal two significant red galaxy overdensities, one at the redshift given in Table 2.1 and another at $z \approx 0.4$. On inspection of the spatial distribution of galaxies, we attribute the SZ signal to the higher redshift system.

SPT-CL J2259-5617 We identify this cluster with Abell 3950, and recover a spectroscopic redshift from archival data on what we identify as the BCG. The SPT SZ detection coordinate lies nearly exactly on the line joining the two Abell 3950 coordinates given in the literature, at a projected distance of $71''$ from that quoted by Arp & Madore (1996), and $208''$ from that quoted by A89. The redshift of Abell 3950 has not been previously measured, but we have identified the BCG in 2MASS as 2MASX J23000108-5617061, which the 6dF Galaxy Survey measured to be at $z_{\rm spec} = 0.152787$ (Jones et al., 2005). This galaxy lies $18''$ from the SPT coordinate.

SPT-CL J2300-5331 We identify this with Abell S1079 (A89). No previous redshift estimates exist for this cluster.

SPT-CL J2331-5051 This cluster exhibits a giant gravitational lens arc and a well separated secondary cluster structure in both the optical and SZ data. This is among the most interesting of the clusters presented here, and is the subject of a dedicated study (High et al., in preparation).

SPT-CL J2332-5358 This cluster was recently identified by M10 as SCSO J233227-535827.

SPT-CL J2343-5521 No red-sequence cluster appears in BCS imaging, whose 50% completeness depth in the i band is 23.5 mag, corresponding to m^* at $z \approx 1.2$. Either there exists a cluster at higher redshift, or this is a false SZ detection. V10 show that the false detection rate is only 7% for clusters at equivalent SZ significance. However, the SZ profile radius is significantly larger than any other cluster, consistent with a cosmic microwave background fluctuation. Preliminary follow-up of this cluster at other wavelengths suggest this is indeed a false detection.

2.5 Discussion of Systematic Effects

The greatly different criteria with which our SZ clusters were selected as compared to the MaxBCG sample could give rise to differences in measured properties. One important effect is the evolution of the mean and scatter of red cluster-galaxy colors with redshift and mass. While elliptical (E) galaxies are highly homogeneous in the range of redshifts our sample represents, $0 < z \lesssim 1.2$ (Menci et al., 2008; Lidman et al., 2008; Mei et al., 2009), the mean and scatter of S0 galaxy colors are known to evolve with redshift and density of the environment (e.g., van Dokkum et al., 1998). The environment also causes color evolution with distance from the cluster center. Our method, and indeed that of MaxBCG, does not explicitly use morphological selection criteria, so we must assume E and S0 populations contribute to our richness estimates. Understanding color-selection effects at all redshifts for a large sample of clusters would require sophisticated simulations or full photometric redshift measurements that are beyond the scope of this work.

Another important effect is the evolution of the abundance of early-type cluster galaxies as a function of luminosity. Clusters have been observed to accumulate faint galaxies at a greater rate than bright ones over time, manifesting as evolution in the slope of the luminosity function's faint end, α, as a function of redshift (Rudnick et al., 2009). Despite our long redshift baseline, we expect our measurements here to be largely unaffected by behavior at the faint end, as we integrate the LF down to a relatively shallow magnitude of $m^* + 1$. Indeed, tests where we vary α have not significantly affected our results.

In addition, because our richness measurement is not exactly that used with maxBCG (from which the R_{200}–$N_{\rm gal}$ relationship that we use here is taken) our R_{200} estimates are likely to be somewhat overestimated (cf. discussion in Hansen et al., 2009). Using a larger-than-ideal aperture for counting red galaxies may contribute to some of the scatter in the richness-mass correlation that we observe here.

Red galaxy counting has nonetheless proven to be a simple and accessible way to estimate the total mass in clusters and groups. If this technique can be accurately extended to the very wide range of redshifts that SPT SZ-selected clusters span, then modeling and measuring evolutionary effects in SZ clusters will be useful to obtaining constraints on masses of very large cluster samples.

2.6 Conclusions

We have observed clusters from the 2008 South Pole Telescope SZ survey at optical and near-infrared wavelengths. We estimate redshifts and richness with red-sequence techniques, and we obtain spectroscopic redshifts for a subsample of the clusters.

Our red-sequence-derived redshifts exhibit 2% RMS scatter in $\sigma_z/(1+z)$ in the subsample with spectroscopic overlap, over the redshift range $0.15 < z < 1.0$. Our analysis provides no evidence that the SZ selected sample from SPT follows different scaling relations than those followed by SDSS optically selected clusters.

The clusters presented in this paper comprise the largest sample of galaxy clusters discovered with the SZ and demonstrates that current SZ surveys can detect many high-mass galaxy clusters across a wide range of redshifts. Precise dark energy constraints from these surveys require the cluster redshifts, masses, and selection function to be known. The SZ effect contains no redshift information, and coordinated observations at optical and infrared wavelengths are an efficient means of providing this, especially for large cluster samples. Optical cluster identification is also potentially useful for understanding SZ selection functions. In the future, there will probably be greater coverage of SZ clusters by OIR imaging than any other wavelength or observing method other than the millimeter-wavelength itself. Optical redshifts are essential for constraining cosmology with SZ surveys, and the same data may also be brought to bear on the mass and cluster selection problems.

2.7 Acknowledgments

This research has made use of the NASA/IPAC Extragalactic Database (NED) which is operated by the Jet Propulsion Laboratory, California Institute of Technology, under contract with the National Aeronautics and Space Administration. This publication has made use of data products from the Two Micron All Sky Survey, which is a joint project of the University of Massachusetts and the Infrared Processing and Analysis Center/California Institute of Technology, funded by the National Aeronautics and Space Administration and the National Science Foundation. This research has made use of the NASA/ IPAC Infrared Science Archive, which is operated by the Jet Propulsion Laboratory, California Institute of Technology, under contract with the National Aeronautics and Space Administration.

IRAF is the Image Reduction and Analysis Facility, distributed by the National

Optical Astronomy Observatories, which are operated by the Association of Universities for Research in Astronomy, Inc., under cooperative agreement with the National Science Foundation.

We used the cosmology calculator tools of Wright (2006).

This work is supported by the NSF (AST-0607485, AST-0506752, ANT-0638937, ANT-0130612, MRI-0723073), the DOE (DE-FG02-08ER41569 and DE-AC02-05CH11231), NIST (70NANB8H8007), and Harvard University. B. Stalder and A. Loehr gratefully acknowledge support by the Brinson Foundation. R. J. Foley acknowledges the generous support of a Clay fellowship.

We also thank the team of scientists, engineers and observing staff of the Las Campanas Observatory and of Cerro Tololo Inter-American Observatory.

Chapter 3

Stellar Locus Regression

3.1 Introduction

The observed broadband colors—*i.e.* flux ratios—of celestial objects depend on the photon spectral energy distribution of the source; on extragalactic, Galactic and atmospheric scattering and absorption along the line of sight; and on the instrumental sensitivity function over the wavelengths of interest. One challenge of astronomical photometric analysis is to disentangle, from a given set of observations, the source's colors from such a plethora of perturbing factors.

Colors hold information about a source's type, temperature, metallicity, and redshift. A source's apparent magnitude, on the other hand, also depends on its distance and on the size and nature of the emitting regions. We assert that for almost all astrophysical endeavors, accurate photometric *colors* are more useful than high accuracy *magnitudes*, especially because we seldom know distances well enough to convert from apparent to absolute magnitudes at the percent level. Furthermore, for photometric redshift techniques that use a prior on magnitudes, the broad luminosity function of galaxies generates a span in magnitude that far exceeds the range in color, for a given galaxy type at a particular redshift.

The current and next generation of wide-field multicolor survey projects include the CFHTLS[1], PanSTARRS[2], BCS[3], DES[4], LSST[5], and SkyMapper[6]. Object classification and distance estimation with photometric redshifts are necessary starting points for extragalactic science using these surveys, and these in turn depend on knowing calibrated colors. The technique we describe here can be used very early in a survey to obtain highly accurate colors of objects, as well as magnitude estimates. This should allow more rapid exploitation of new survey data—indeed, of nearly any multiband data.

The standard approach to determining colors of sources is to first calibrate magnitudes in all observed passbands (such as g, r, i, and z), and then subtract the calibrated magnitudes to obtain calibrated colors ($g-r$, $g-i$, *etc*). This is typically time-consuming, both at the telescope and in the analysis phase. Establishing photometric zeropoints for a stack of multiband images requires separate observations of spectrophotometric standard stars to measure the instrumental sensitivity and estimate atmospheric extinction, and spatiotemporal interpolation of the calibration

---

[1] `http://www.cfht.hawaii.edu/Science/CFHLS/`

[2] `http://pan-starrs.ifa.hawaii.edu/public/`

[3] `http://cosmology.uiuc.edu/BCS/`

[4] `https://www.darkenergysurvey.org/`

[5] `http://www.lsst.org/Science/lsst_baseline.shtml`

[6] `http://msowww.anu.edu.au/skymapper/`

parameters to the science fields under “photometric conditions.”

In this paper we describe how to calibrate optical and infrared colors directly from objects cataloged from multiband, flat-fielded images of a field, without having to first determine the corresponding photometric zeropoints, and without the usual repeated measurements of standard stars. While here we perform tests within the $grizJ$ filter set, we fully expect the method to be equally useful when applied to other, appropriate combinations of $grizBVRIJHK$. We would generally exclude the u- and U-bands, as they have heightened sensitivity to the effects of stellar metallicity and Galactic dust extinction. As we note in §3.2, the appearance of a “kink” feature in the stellar locus is what makes our method possible, and this is afforded by including, at minimum, a blue filter such as g or B in addition to at least 2 of any other filters. We demonstrate how calibrations can be done on such data accurately, yielding colors accurate to a few percent; and rapidly, allowing for optimal use of allocated telescope time.

Our technique exploits the optical and infrared color-color *stellar locus* (cf. Covey et al., 2007; Ivezić et al., 2007), the one-dimensional and astrophysically fundamental track that stars occupy in color-color space. The majority of stars lie somewhere along this locus, at a position that depends primarily upon effective temperature. The universality of the stellar locus was exploited in the Oxford-Dartmouth Thirty-Degree Survey (“stellar locus fitting,” MacDonald et al., 2004) to stabilize photometric zeropoints in non-photometric conditions, and in Sloan Digital Sky Survey’s (SDSS) Stripe 82 (“stellar locus method,” Ivezić et al., 2007) to account for differences in the response function of different detectors in the SDSS instrument. Our approach is different from these mainly because we do not first establish photometric zeropoints per band: we immediately calibrate colors in all fields, and only optionally solve for the calibrated apparent magnitudes, using the stellar locus. We do not use Stellar Locus Regression as a diagnostic or corrective tool, but as our primary calibrator. The resulting, calibrated colors can be immediately used in studies such as that of Witham et al. (2008), who discovered $H\alpha$ emission-line objects, which are stellar locus outliers, purely in color-color space.

Our Stellar Locus Regression (SLR) approach builds on these previous pioneering works. We establish the location of the stellar feature in instrumental color-color space, and we determine what transformations are needed to bring this into coincidence with the known location of a standard stellar locus. Applying appropriate color-corrections to the entire rest of the catalog automatically accounts for all of the standard calibration terms, including zeropoints, atmospheric extinction, aperture corrections, and Galactic extinction. The technique is straightforward, fast, and requires observers to observe standard star fields *far less frequently than once per night* (and only to measure color terms), because all observed stars are expected to lie along the same stellar locus. We have calibrated fields with SLR using as few as 7 stars in fields of view as small as $4' \times 8'$. While SLR, as it stands, requires such infrequent standard star observations, we of course acknowledge that it relies on data calibrated in the traditional way in order to construct the standard locus. However, once this is done, it need not be repeated except to improve the standard itself.

Figure 3.1 schematically illustrates the technique. We perform SLR on new data (see §3.4.2-3.4.4) taken with the IMACS instrument (Dressler et al., 2003b; Osip et al., 2008b) on the Magellan 6.5 m telescope. All panels show our adopted standard stellar locus line and stellar density contours, reproduced from Covey et al. (2007, §3.2.1), along with 36 IMACS stellar colors (red points). The top panels show instrumental stellar colors with the standard locus. We perform SLR, neglecting instrumental color terms, with results shown in the middle panels. We perform SLR again after measuring color terms independently from an external standard star field, with results shown in the bottom panels. By way of illustration, the vectors in the middle panels show the expected direction and magnitude of extinction by Galactic dust ($A_r =$ 0.2 mag and $R_V = 3.1$, estimated using Schlegel et al., 1998) and the atmosphere (1.3 airmasses).

We adopt a standard stellar locus in §3.2, and then motivate and build a picture of what comprises it so as to understand its universality. In §3.3 we outline the mathematics of color calibration and describe an optimal algorithm for real-time color calibration, which we apply to real data in a series of tests (§3.4). In §3.4.1 we perform our first test, applying SLR to already-calibrated SDSS photometry, where we recover the canonical Galactic reddening vector in direction and magnitude over a wide rage of dust thicknesses. Section 3.4.2 examines the fundamental repeatability of SLR color and magnitude measurements by comparing SDSS data to data from a different instrument. Section 3.4.3 isolates the effect of atmospheric extinction. Our final test appears in §3.4.4, where we recover the spectroscopic redshifts of 11 low redshift galaxy clusters to high accuracy using only SLR colors. We end with a discussion (§3.5) and conclusions (§4.7).

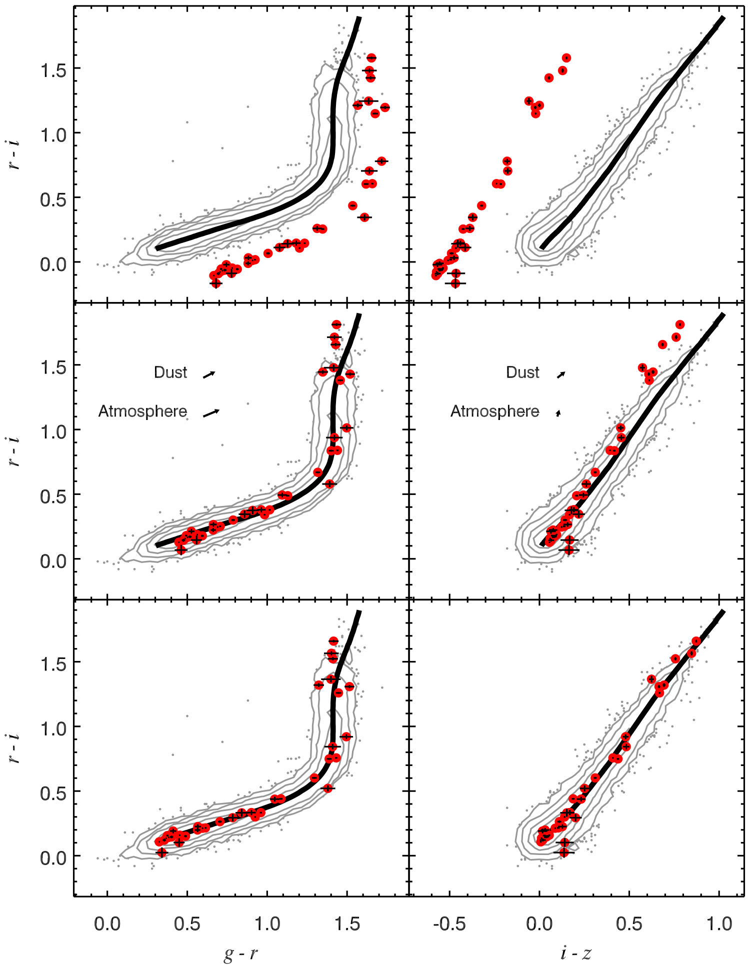

Figure 3.1: An illustration of Stellar Locus Regression (SLR). Colors are plotted on the SDSS photometric system. All panels show the standard stellar locus (black line and gray density contours), reproduced from Covey et al. (2007). Red points are stellar colors obtained from a Source Extractor analysis of flat-fielded Magellan 6.5 m IMACS images. *Top panels:* The instrumental IMACS colors are plotted, with a clear mismatch between them and the standard locus. *Middle panels:* SLR is performed with only a common translation vector applied to the instrumental colors. Note the color-dependent discrepancies in the upper right portions of the central panels. By way of example, the vectors show the expected direction and magnitude of extinction by Galactic dust ($A_r = 0.2$) and the atmosphere (1.3 airmasses). *Bottom panels:* Color terms are measured from a single observation of a field containing standard stars. Fixing these color terms, a new best-fit translation is determined, which brings the observed colors onto the SDSS-calibrated color system, as defined by the stellar locus. This SLR analysis, when the corrections are then applied to all objects in the photometric catalog, allows us to rapidly obtain highly accurate colors on the SDSS system, directly from flat-fielded data, with a single correction step that accounts for atmospheric extinction, Galactic extinction and instrumental response differences.

3.2 The Stellar Locus

The nearly-blackbody emission spectra of stars place them predominantly along a line in optical and infrared color-color space. Stellar color therefore depends primarily on effective temperature and is the basis for the Morgan-Keenan (MK) stellar classification system (Morgan et al., 1943). Real stellar atmospheres deviate from blackbody behavior because of molecular absorption and metallicity effects. Observations, which capture stellar light that has traversed the dust of our galaxy, our atmosphere, and our telescope systems, will produce stellar color loci that deviate further from the expected intrinsic behavior. We have based our SLR approach on the assumption that we can identify a stellar locus in $grizJ$ color space that is intrinsically universal. We explore the extent to which this is true by inspecting what comprises an observed stellar locus.

3.2.1 A Standard Locus

We adopt as our standard the empirical stellar locus of Covey et al. (2007). Those authors calculated the running-median of the colors of $\sim 10^5$ stars, from high quality observations by both the SDSS and 2MASS surveys. The line-of-sight Galactic dust for their sample was estimated from the maps of Schlegel et al. (1998, SFD) to be $A_r < 0.2$. We additionally smooth this locus line with a 0.2 mag size boxcar averaging kernel to reduce some of the scatter between adjacent points. These are the data we present in Figure 3.1—we call this the standard stellar locus line.

The two most salient features of the standard locus are its nearly one-dimensional nature and a dramatic break or kink in the $(g-r, r-i)$ plane at $r-i \sim 0.7$. As we explore below (§3.2.2), blue-ward of the kink are mainly evolved and main sequence (MS) A- through K-type stars, and red-ward are mainly M-type dwarfs (Finlator et al., 2000; Hawley et al., 2002; Covey et al., 2007; Jurić et al., 2008).

Because of the well-defined relationships between the color (effective temperature), age, and intrinsic luminosity of stars, each point along the stellar locus probes roughly predictable 3-dimensional spatial volumes, given some fixed dynamic range for the observations. The reddest MS stars that make up the $r-i > 0.7$ branch of the stellar locus are less luminous, so the effective volume an observation probes is small and nearby. Likewise, bluer MS and evolved stars are intrinsically brighter, so the effective volumes probed at those colors are larger and farther away—and because both MS and evolved stars constitute the $r-i < 0.7$ portion of the stellar locus, observations are sensitive to a plurality of volumes and distances.

A comprehensive Galactic structure and population synthesis analysis is beyond the scope of this paper, but we will explore below the factors that give rise to uniformity in the *observed* stellar locus, including the dramatic color-volume effects at typical SDSS depths.

3.2.2 Color-Volume Effects

Each pointing of an astronomical camera images a cone-shaped region of space, set by the solid-angle field of view Ω of the instrument. For a single frame there is also a limited observable dynamic range in apparent magnitude: the brightest observable objects are determined by the saturation limit of the system, and the faintest useful objects must satisfy some selection in signal-to-noise ratio. A star of a particular absolute magnitude and corresponding color is therefore detectable within a truncated cone of opening angle Ω, with an near-edge determined by the saturation limit and a far-edge set by the required signal-to-noise ratio. For simplicity we assume an unextincted line of sight.

Table 3.1 illustrates the dramatic selection-effect of dynamic range on observed stars of various intrinsic luminosities. We take a notional saturation limit of $r = 14$ and a faint detection limit at $r = 22$, which are approximate values appropriate for SDSS. For a dynamic range of 8 mag, the outer detection edge of the detectability cone is always ~ 39 times farther away than its inner saturation edge, for a given absolute magnitude object. Table 3.1 also shows that for each additional magnitude increase of stellar luminosity, the survey volume increases by a factor of four. Luminous stars are detectable over a vastly larger volume than fainter stars, since the outer edge of the detectability region is *proportional to* the distance to the inner edge.

As a concrete example, at SDSS depths and Galactic latitudes $|b| = 90$ deg, absolute magnitudes $\mathrm{M}_r \gtrsim 12$ are detectable only closer than $\sim 1\,\mathrm{kpc}$, which is the height of the Galactic disk (Jurić et al., 2008). Objects with $\mathrm{M}_r \lesssim 4$ are seen only at Galactic heights $|Z| > 1\,\mathrm{kpc}$, so are in the halo.

Table 3.1: Detectability Volumes vs. Absolute Magnitude.

M_r (AB mag)[a]	R_{inner} (pc)[b]	R_{outer} (pc)[c]	Detectability Volume (pc^3)[d]
-5	6.3E4	2.5E6	1.0E12
-4	4.0E4	1.6E6	2.8E11
-3	2.5E4	1.0E6	6.3E10
-2	1.6E4	6.3E5	1.6E10
-1	1.0e4	4.0E5	4.0E9
0	6.3E3	2.5E5	1.0E9
1	4.0E3	1.6E5	2.5E8
2	2.5E3	1.0E5	6.3E7
3	1.6E3	6.3E4	1.6E7
4	1.0E3	4.0E4	4.0E6
5	6.3E2	2.5E4	1.0E6
6	4.0E2	1.6E4	2.5E5
7	2.5E2	1.0E4	6.3E4
8	1.6E2	6.3E3	1.6E4
9	1.0E2	4.0E3	4.0E3
10	6.3E1	2.5E3	1.0E3
11	4.0E1	1.6E3	2.5E2

Continued on next page...

Table 3.1 – Continued

M_r (AB mag)[a]	$R_{\rm inner}$ (pc)[b]	$R_{\rm outer}$ (pc)[c]	Detectability Volume (pc^3)[d]
12	2.5E1	1.0E3	6.3E1
13	1.6E1	6.3E2	1.6E1
14	1.0E1	4.0E2	4.0E0
15	6.3E0	2.5E2	1.0E0

Absolute stellar magnitude varies with stellar color and age in well understood ways. To explore the relation in the SDSS magnitude system, we used the model stellar populations of Marigo et al. (2008, `http://stev.oapd.inaf.it/cgi-bin/cmd_2.1`). This online tool modeled stars with initial masses down to $0.15\,M_\odot$. We have just shown that the typical SDSS dynamic range is sensitive to both halo and disk stars, so we consider three models, using Ivezić et al. (2008) as a guide:

1. a 13 Gyr halo population, with a metallicity $[\mathrm{Fe/H}]_{\rm halo} = -1.5$,
2. a 13 Gyr disk population of higher metallicity, $[\mathrm{Fe/H}]_{\rm disk} = -0.5$, and

---

[a] Absolute magnitudes of stars in the SDSS r-band.

[b] Closest distances (in parsecs) for the object to be observable, for a notional saturation limit of $r = 14$.

[c] Furthest distances (in parsecs) for a 10σ detection limit of $r = 22$.

[d] Volume (in arbitrary units) within which objects of a given absolute magnitude can be detected, subject to the instrumental dynamic range constraints.

3. a 5 Gyr disk population of higher metallicity, $[\mathrm{Fe/H}]_{\mathrm{disk}} = -0.5$.

Figure 3.2 shows the color-magnitude and color-color diagrams that illustrate the connection between absolute magnitudes and regions in color-color space for these populations.

Figure 3.2 shows that only disk-metallicity stars populate the locus red-ward of the kink. The main sequence M dwarfs in this color range have $M_r \gtrsim 11$ mag and so in the SDSS dynamic range these objects lie at distances $\lesssim 1.5$ kpc from Earth. These stars are almost entirely in the disk. The M giants red-ward of the kink have $M_r \lesssim -2$ mag corresponding to distances $\gtrsim 15$ kpc. Few disk-metallicity stars lie at such distances (Ivezić et al., 2008). Therefore the vast majority of the stars that populate the $(r-i) > 0.7$ region of the locus at SDSS depths are disk dwarfs. Hawley et al. (2002) also support this viewpoint, attributing SDSS objects with $1 < (r-i) < 2$ to M0 through M6 stars at typical distances ranging from 1 to 0.1 kpc respectively.

Continuing these arguments, stellar locus stars blue-ward of the $(r-i) \sim 0.7$ kink comprise of a blend of MS disk stars, MS halo stars, and evolved (post-turnoff) halo stars. The luminosity of the bluer MS stars are 4 mag $\lesssim M_r \lesssim$ 11 mag and are detectable from both the disk and halo. We also see that even for a stellar population 13 Gyr old, with a main sequence turnoff at around $M_r \sim 4$, blue turnoff stars that are closer than 1 kpc would saturate the detector.

The relative proportion of disk and halo stars that make up the stellar locus at $(r-i) < 0.7$ (blue-ward of the kink) is magnitude dependent. Ivezić et al. (2008) show that for $0.2 < (g-r) < 0.4$, at $g \sim 17.5$ half the stars have metallicity characteristic of the disk, and half are halo stars. In deeper observations the proportion of halo

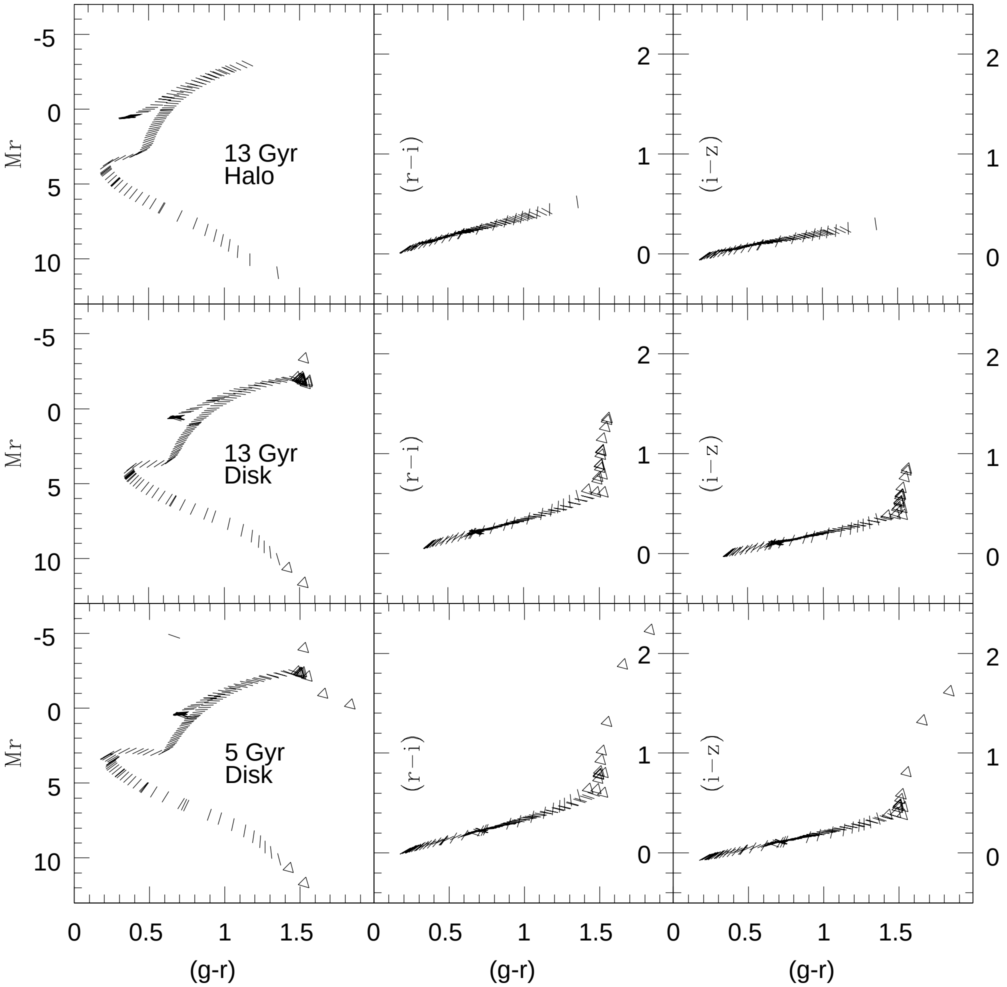

Figure 3.2: Comparisons of modeled M_r vs. $g - r$ color-magnitude diagrams (left column), $r - i$ vs. $g - r$ (central column), and $i - z$ vs. $g - r$ (rightmost column) color-color diagrams for different stellar populations, for zero Galactic extinction. The upper row corresponds to a stellar halo population with [Fe/H] = -1.5 and an age of 13 Gyr. The central row also corresponds to a 13 Gyr age, but with a characteristic disk metallicity; [Fe/H] = -0.5. The bottom row is what one might expect for more recent star formation in the Galactic disk, with [Fe/H] = -0.5 and an age of 5 Gyr. Absolute magnitudes are indicated by the *angle* of the whisker, with $\theta = 9M_r\,\mathrm{mag}^{-1}$ deg. Objects with $(r - i) > 0.7$ are shown as triangles. Only stellar populations with [Fe/H] > -0.7, seen in the central and lower rows, produce the “kink” feature in the stellar locus; this feature is what enables SLR to uniquely solve for color calibration parameters.

stars increases. Shallower observations will likewise contain fewer halo stars, but the number of M disk stars will decrease until, at the brightest limiting magnitudes, there are effectively no stars red-ward of the kink. SLR requires the kink feature to find a unique color-calibration solution, as a straight line would not uniquely locate points in color-color space without additional information. SDSS depths and deeper give good proportions of stars red- and blue-ward of the kink; observers intent on employing SLR are advised to consider these arguments when deciding on single-epoch exposure times.

Armed with this understanding of the observed stellar locus's constituent populations, we explore the effect their corresponding metallicity distributions should have.

3.2.3 Metallicity

A number of previous authors have explored the influence of metallicity on stellar colors in the SDSS photometric system (Lenz et al., 1998; Covey et al., 2007; Jurić et al., 2008; Ivezić et al., 2008). Ivezić et al. (2008) demonstrated that most halo stars have a common metallicity that is reasonably well described by a Gaussian distribution with median $[\mathrm{Fe/H}]_{\mathrm{halo}} = -1.5$ and width $\sigma_{\mathrm{halo}} = 0.3\,\mathrm{dex}$. The median disk metallicity was shown to be about -0.5 and exhibits half the scatter of the halo, with $\sigma_{\mathrm{disk}} = 0.16\,\mathrm{dex}$.

The biggest observable broadband effect from metallicity occurs in the u-band, which is one of the reasons we exclude that band from consideration here. Stellar metallicity effects in $g - r$ are ten times smaller than in $u - g$. Using this fact and

Figure 21 of Ivezić et al. (2008), the expected spread in $g-i$ color for halo stars should be of order 0.05 mag. This is a conservative upper limit estimate of the intrinsic width of the halo contribution to the stellar locus from metallicity alone.

We have modeled the effect of metallicity on the stellar MS, and present some of the results in Table 3.2. We used a grid of model atmospheres derived from the Phoenix project (Brott & Hauschildt, 2005) and the Kurucz (1993) library for the typical disk and halo metallicities, [Fe/H] $= -0.5$ and -1.5 dex. The range of parameters used was $3,500K \leq T_{\rm eff} \leq 10,000K$ for M5 to A0 using the Phoenix models and $15,000K \leq T_{\rm eff} \leq 45,000K$ for B5 to O5 from the Kurucz (1993) models, and we adopted a typical main sequence $\log(g)$ for each spectral type. We then calculated the broadband colors based on the SDSS filter and CCD throughput.

Table 3.2: Model Stellar Color Difference Between $Z = -0.5$ and $Z = -1.5$.

MK type	$\delta(g-r)^{\rm a}$	$\delta(r-i)^{\rm a}$	$\delta(i-z)^{\rm a}$
O5V	-0.005	-0.002	-0.003
B0V	-0.000	-0.002	-0.002
B5V	-0.003	-0.002	-0.005
A0V	-0.000	-0.004	-0.003
A5V	0.004	-0.007	-0.007
F0V	0.004	-0.010	-0.012

Continued on next page. . .

Table 3.2 – Continued

MK type	$\delta(g-r)^{\mathrm{a}}$	$\delta(r-i)^{\mathrm{a}}$	$\delta(i-z)^{\mathrm{a}}$
F5V	0.019	-0.009	-0.013
G0V	0.031	-0.012	-0.015
G5V	0.037	-0.013	-0.015
K0V	0.053	-0.015	-0.014
K5V	0.124	0.002	-0.014
M0V	0.004	0.067	0.031
M5V	-0.137	0.117	0.080

We found that the greatest influence of metallicity on broadband color is in the late-type stars (around M0 and later) and is in opposite direction to the color displacement of early-type stars. The relatively cool atmospheres of the red stars are rich with molecules, and the molecular absorption features blend together with other lines to form a continuum that differs substantially from a blackbody spectrum. We also observed that a minimum metallicity of [Fe/H] $= -0.7$ is needed for red stars to populate the locus red-ward of the kink. Less metallicity "irons out" the kink, making the model colors colinear with the bluer stars. This observation is consistent with the conclusions drawn in §3.2.2. A continuum of metallicities near this threshold

---

[a] As a comparison, for galactic extinction ($A_r = 0.2$) the color perturbation is (0.076, 0.048, 0.044); for 1.3 atmospheres of extinction, the color perturbation is (0.103, 0.053, 0.010).

would smear the observed stellar locus in the redder region. The apparent lack of such smearing in the observed locus indicates the paucity of stars at this intermediate metallicity, as found by Ivezić et al. (2008). It is therefore the high mean metallicity and molecular absorption of disk stars that produce the kink in the SDSS stellar locus in the first place, and that make our implementation of SLR possible.

3.2.4 Age

Younger stellar populations have a brighter, bluer main sequence turnoff point, and this shifts the blue tip of the stellar locus towards the blue. This does not distort the basic shape of the stellar locus. For very young populations at high metallicity there is also a red-ward extension of the main locus, due to massive stars evolving to $r - i > 0.7$, but we concluded in §3.2.2 that these stars do not appear in the stellar locus at SDSS depths, since these young stars would be in the disk and would saturate. Other features in the color-magnitude diagram, such as helium-burning loops, essentially remain confined to the standard locus line and do not change its shape. Our methods (§3.3) are therefore expected to be largely insensitive to population age effects.

3.2.5 Binaries and Unresolved Superpositions

Superpositions of stars, either as physical binaries or chance coincidences, most often fall within the standard locus area, but can also produce systematic outliers and therefore change the observed stellar locus shape. For the latter to happen, the objects within a single PSF must have different colors, but similar magnitudes. One can adopt two philosophical resolutions to this issue.

One approach is to realize that both our standard locus and the instrumental colors should contain binaries, and so the effect will average to zero over many fields. While this may be true statistically, if the stars drawn from an observed field are few in number, the observed stellar locus may be distorted by small number statistics.

Another approach is to iteratively excise stellar colors that are significantly different from the standard color expectation. This should suppress locus shape distortions due to the occasional unresolved binary, but nevertheless the incidence of binary outliers is expected to be low. Smolčić et al. (2004) have shown the existence of an “echo” of the stellar locus, which they ascribed to unresolved binaries of similar luminosity but different effective temperatures. They assessed the number of objects in this “echo locus” as being fewer than 1/2000 as numerous as the objects that occupy the main stellar locus. The combined low incidence and known location of these outliers makes these binaries unproblematic.

3.2.6 Variable Stars

Photometric variability is a source of systematic error for stellar locus color methods. If a star’s observed brightness varies in the time between observations in the various passbands under analysis, even if the underlying stellar color does not vary, the magnitude differences will introduce a shift in color-color space. Since the SDSS photometric data in different bands are obtained within a few minutes of each other, the SDSS-band standard stellar locus should have minimal contamination from this effect. Similarly, the 2MASS instrument obtained J, H, and K photometry essentially simultaneously. Combining 2MASS and SDSS photometry, however, can fall prey to variability, since the observations were taken at different times. So establishing the joint optical-NIR standard stellar locus must attend to this issue.

Similarly, if the images under analysis are obtained at different times, variability on this timescale will distort the derived calibration color shifts. Sesar et al. (2007) explored the incidence of variables in the SDSS color-color diagram. They showed that there is a substantial variation in the fraction of objects that exhibit variability, across the color-color diagram. The blue tip of the stellar locus has two classes of variables: low redshift QSOs and RR Lyrae stars. These can be suppressed by selecting a judicious region in color-color space where the standard locus is matched to the instrumental color distribution, iteratively.

The multi-epoch analysis of SDSS photometry in Sesar et al. (2007) indicates that fewer than 5% of the objects in the main stellar locus exhibit variability with $\Delta g > 0.05\,\mathrm{mag}$. A sigma-clipped iterative analysis of multi-epoch photometry should be able to produce a cleansed standard stellar locus.

3.2.7 Galactic Dust

Galactic dust is another extrasolar source of stellar locus perturbations. The dust is shown by Marshall et al. (2006) and Jurić et al. (2008) to be confined to a sheet roughly 100 pc above and below the Galactic midplane. At SDSS depths, the vast majority of stars are therefore behind the dust.

To first approximation the extinction obeys the canonical $R_V = 3.1$ reddening law and the degree of extinction A_V follows the maps of SFD. This induces a simple overall color-color vector shift—reddening—whose direction depends on R_V and whose magnitude depends on A_V. Ivezić et al. (2007) showed that the stellar locus position reflects these predictions in some regions of SDSS Stripe 82, but breaks down as Galactic latitude $|b|$ decreases (§3.4.1).

The usual adoption of extinction coefficients from the SFD appendix assumes an underlying spectral energy distribution typical of an elliptical galaxy. This is not valid for Galactic stars (eg McCall, 2004). To next approximation, a more correct treatment would provide extinction coefficients for each stellar spectral type. Errors of this form induce differential distortions of the stellar locus as a function of effective temperature.

Other deviations occur when the basic assumptions of extinction behavior break down. If the reddening law is not strictly $R_V = 3.1$ (eg Larson & Whittet, 2005), the stellar locus shifts in different directions. If some observed stars are in front of the dust and others behind, the stellar locus will show additional scatter, preferentially in the reddening directions. Because the stars are most often behind the dust, Galactic extinction is a major contributor to the observed stellar locus properties.

The SLR approach makes no specific assumption about any value of R_V. It corrects for Galactic extinction subject to the assumption that the observed stars all lie behind a *common* Galactic extinction layer. We suspect a fruitful approach might be to make an initial adjustment to the instrumental colors using SFD and $R_V = 3.1$, and then run SLR on the resulting catalog.

3.2.8 Summary

Taking all this information together, we have clear expectations for what constitutes the typical observed stellar locus, and what factors change its observed position or shape.

Stars with $r - i > 0.7$ are mainly faint M dwarfs in the disk, with correspondingly high metallicity. Since these objects are only visible out to $\sim 1\,\mathrm{kpc}$, only metallicity variations in this local region of the Galaxy could perturb the kink region of the observed locus.

The stars blue-ward of the kink, however, are a magnitude-dependent combination of halo stars and disk main sequence stars. The metallicity dependence of this region of the locus is small.

While the location of the bluest terminating edge of the stellar locus is an indicator of the age of the underlying population, it does not distort the basic shape of the locus line.

Galactic dust should be a prime source for locus shifts and possibly small distortions. At high Galactic latitudes the vast majority of SDSS stars reside behind the dust lanes of the Milky Way. At low Galactic latitudes, even distant stars come closer to the Galactic plane. We would therefore expect to eventually see a smearing of the stellar locus due to stars suffering different amounts of extinction along the line of sight.

Finally, atmospheric and instrumental effects will naturally perturb the stellar locus, and we model these in our mathematical formulation of Stellar Locus Regression (§3.3). Given what we have learned about the nature of the observed stellar locus, our conception of SLR begins with a simple set of assumptions.

1. The standard stellar locus is representative of the typical stellar populations that we will observe in practice, and is sufficiently uniform so as to constitute a calibration standard. The standard locus stars:
    (a) are disk dwarfs in the red and both disk and halo stars in the blue, thanks to the dramatic color-volume effects at SDSS depths, and
    (b) lie at high enough Galactic latitude to put them behind the dust, but suffer low dust extinction.
2. Stars we observe in practice are always *behind* the Galactic dust sheet. This way, SLR directly outputs dereddened colors.
3. The Galactic dust extinction can obey *any* power law R_V.
4. The Galactic dust extinction is locally smooth.
5. Observations include the g-band, and are deep enough to observe at least a few of the faint M dwarfs that constitute the kink feature (limiting $g \gtrsim 18\,\mathrm{mag}$, Ivezić et al., 2008).
6. The input images from which instrumental photometry is extracted are properly flat-fielded.

Many of these are testable in isolation (§3.4), but some possibly degenerate effects, such as simultaneously anomalous metallicities and extinction laws, may be difficult to disentangle. We deduce nonetheless that the combination of magnitude dynamic range selection effects and the relative insensitivity of the $grizJ$ stellar locus to stellar metallicity, age differences, and binary and variable contamination produces an observed stellar locus that is uniform enough to achieve calibration of colors using a standard stellar locus.

3.3 The Method

The basis of Stellar Locus Regression is to transform instrumental stellar colors so that they align with a standard locus, on the SDSS photometric system. This requires typical data preprocessing and photometry that produces instrumental stellar colors from single-epoch, flat-fielded images. The only calibration images required for SLR are a single set of multiband observations of a high-density standard star field, from which instrumental color terms are measured. Periodic updates to the instrumental color terms will depend on the timescale over which these terms evolve. Mosaic imagers will benefit from chip-by-chip color terms. Then, with fixed color terms applied, SLR calibrations are performed on science frames by iteratively transforming the instrumental stellar colors to optimize a goodness-of-fit (GOF) statistic. The resulting best-fit parameters, including the instrumental color terms, define the color transformation that achieves the SLR calibration. Uncertainties in the calibration are estimated numerically. These calibration terms are then applied to all the cataloged photometry of objects appearing in the same images. This way all objects in the field are calibrated using the same stars lying in that field, and no spatial nor temporal interpolation is required.

In this section we describe and motivate our calibration equations, discuss our chosen GOF and method of error estimation, and outline a practical algorithm that we have implemented for the real-time calibration of $grizJ$ colors.

3.3.1 Color Transformations

A *color transformation* is the mathematical transformation of colors by translations, scalings, rotations and shears. Instrumental colors are represented with the vector[7] $\boldsymbol{c}$, and "true" colors, which we take to be on the SDSS photometric system, are represented with the vector $\boldsymbol{c}_0$. Instrumental colors relate to the true colors via the color transformation equation

$$\boldsymbol{c} = \boldsymbol{\kappa} + (\mathbf{1} + \mathbf{B})\boldsymbol{c}_0. \tag{3.1}$$

The color translation vector $\boldsymbol{\kappa}$ accounts for first order atmospheric extinction, Galactic extinction, zeropoints, and any other additive effects, *known or unknown.* We discuss $\boldsymbol{\kappa}$ in §3.3.2. The color term matrix $\mathbf{B}$ is populated by zeros and constants, typically small, and corresponds to the instrumental color terms from conventional photometric calibrations. We discuss $\mathbf{B}$ in §3.3.3. §3.8 shows in mathematical detail how Equation (3.1) relates to photometric calibration equations that astronomers typically adopt.

3.3.2 The Color Translation Vector

The color translation vector $\boldsymbol{\kappa}$ accounts for differences of zeropoints a, atmospheric extinction E, and Galactic extinction A. The scalar elements of the translation vector

---

[7] Our convention is to assign vectors boldface, lowercase letters, and matrices boldface, capital letters. The *elements* of vectors, matrices, and tensors, like all scalars, are not boldface.

are

$$\kappa_{nm} = a_n - a_m + E_n - E_m + A_n - A_m. \tag{3.2}$$

where n and m are elements of the filter set, for example $n, m \in \{g, r, i, z\}$, and $n \neq m$. See §3.8 for a derivation of this relation, starting from traditional photometric calibration equations.

In traditional photometric calibration, the terms on the right-hand side of Equation (3.2) are estimated independently. Atmospheric extinction is usually modeled using a Bouger extinction law, $k_n X_n$, where k_n is a filter-dependent constant and X_n is the airmass through which the R-band image was taken. The atmospheric extinction constants are extracted using intermittent standard star observations at a range of airmasses and interpolated in space and time to the science frames. This assumes that the linear airmass model reflects truth and is spatiotemporally invariant. Galactic extinction is normally estimated from SFD—a procedure that assumes a single $R_V = 3.1$ dust reddening law (cf. Schlegel et al., 1998). Finally, zeropoints are estimated using the same standard star frames used to measure the atmospheric terms. The zeropoints standardize the photometry, and account for differences in instrumental throughput between facilities and any other unmodeled additive effects. Zeropoints are then interpolated in space and time to the science frames in "photometric conditions," which again assumes spatiotemporal invariance.

SLR is fundamentally different and is not subject to these assumptions. SLR fits for each element of the vector $\boldsymbol{\kappa}$ directly, and therefore calibrates the entire right-hand side of Equation (3.2) in one step. The atmospheric and dust extinctions and the zeropoints are not estimated independently. This is made possible by the universality of colors of abundant MS stars (§3.2). Because of this unique ability of SLR, *it does not matter what mathematical form the extinction and zeropoint terms take in reality, as long as they are additive, because all additive systematic effects are accounted for together by $\boldsymbol{\kappa}$ during SLR.* For example, the Bouger atmospheric extinction law is likely incorrect in the z-band, where water absorption is saturated and the additive airmass dependence probably better follows an $X_z^{1/2}$ airmass power law (cf. Stubbs et al., 2007). Further, as we have mentioned it is probable that not all Galactic dust columns obey the canonical $R_V = 3.1$ extinction law. SLR is immune to additive mis-modeling of the atmosphere, Galactic dust, overall instrument sensitivity differences, aperture corrections, and so on.

Figure 3.1 demonstrates the effect of leaving the color translation vector free during Stellar Locus Regression. The top panels show how the known, standard locus compares to an instrumental stellar locus. In the middle panel, we perform SLR, letting $\boldsymbol{\kappa}$ be free and fixing the color term matrix $\mathbf{B}$ to zero. Residual systematics are clearly evident, in the form of deviations that appear to increase with color. This is expected because we are comparing standard SDSS data to data taken with a different instrument than SDSS. We remedy this by measuring color terms for the instrument once using a standard stellar field observation, and then fixing these nonzero color terms while performing SLR. Color term issues are described in the following section.

3.3.3 The Color Term Matrix

The entries of the color term matrix $\mathbf{B}$ are zeroes or constants. For example, for the SDSS colors we use in §3.4.2-3.4.4, $\boldsymbol{c} = (g - r, r - i, i - z)$, we adopt the color term matrix

$$\mathbf{B} = \begin{pmatrix} b_g & -b_r & 0 \\ 0 & b_r & -b_i \\ 0 & 0 & b_i - b_z \end{pmatrix}. \tag{3.3}$$

This has a direct correspondence with traditional photometric color term formulations, as shown in §3.8.

Color terms, and the color term matrix, account for broad, differential instrument sensitivity differences that arise when data are acquired with different telescopes, CCDs, or filters than those used to generate the standard catalog. For example, we see a clear systematic error between IMACS and SDSS in Figure 3.1 that varies monotonically with color. By estimating color terms with an observation of a standard star field and applying the color term matrix transformation during our SLR, we significantly improve the fit.

We have also estimated color terms directly with SLR by letting the color terms be free in addition to $\boldsymbol{\kappa}$ during the fit. This results in a divergent regression when using our weighted color residual GOF (§3.3.6). The reason is that the global minimum of this GOF occurs when all instrumental data points collapse to a single point, which is allowed by divergent shears and rescalings from $\mathbf{B}$, and divergent, compensatory color translations that put the singular instrumental data somewhere on the standard locus line. The best-fit color terms are extremely large, violating our assumption of smallness. We have experimented with other GOFs with varying success, but none yields color terms with accuracy that rivals that of the traditional procedure.

This is the only step in our real-time color calibration procedure (§3.3.8) that requires standard star observations. If instrumental color terms are stable over, say, month- and year-long timescales, then color terms need only be estimated as infrequently. Without the requirement of multiple standard field exposures per night, the observer maximizes the total exposure time on science fields.

3.3.4 Color-Airmass and Higher Order Corrections

Color-airmass terms take the same essential form as instrumental color terms. §3.8 gives an explicit example of this. Correspondingly, color-airmass terms can be estimated with the same color term procedure described in §3.3.3 and §3.3.8. We have not yet implemented this as we assume these corrections to be small; this is an obvious future addition to our SLR formulation. In principle, corrections proportional to higher order powers of the color, airmass, and even the Galactic dust column can also be measured, but these will require larger, dedicated programs in order to minimize error. As shown in §3.4.2-3.4.4, we achieve 1–2% level self-consistency with respect to zeropoints, airmass, and Galactic dust, without making these corrections.

We now show how, using the same formalism and the same standard locus of §3.2.1, SLR can be made to output individual calibrations for each filter, producing calibrated photometry instead of colors.

3.3.5 Photometric Calibration with SLR Using 2MASS

If the stellar locus is extended into other passbands that are already photometrically calibrated, then the instrumental photometry can be directly calibrated using only the SLR methodology. 2MASS is an obvious choice for an external catalog, as it is full-sky and freely available and the standard locus (§3.2.1) bridges JHK with *ugriz*.

The procedure requires the additional prior step of cross-correlating instrumental stellar catalogs against 2MASS's calibrated data. This is easily done using the Gator web interface[8].

For illustration, say we have obtained the J-band photometry of our instrumental *griz* stars. We construct a color that is a hybrid of instrumental optical magnitudes and calibrated 2MASS magnitudes, $z - J$, which extends the instrumental stellar locus to $\boldsymbol{c} = (g - r, r - i, i - z, z - J)$. SLR is executed in precisely the same way as for the optical data alone, using the standard optical-infrared hybrid locus line. The result is still $\boldsymbol{\kappa}$, but the last entry is $\kappa_{zJ} = a_z + E_z + A_z$ because the 2MASS data are already calibrated: κ_{zJ} is the z-band photometric calibration. This can be done for any combination of instrumental calibrated 2MASS data and instrumental optical or infrared data from a different passband. §3.8 makes the mathematics of SLR photometric calibration explicit for this particular example.

SLR photometric calibration is subject to the errors of 2MASS, and is more precise when more stars are used in the fit. Given typical 2MASS errors of 5%, SLR-calibrated photometric zeropoints should typically be accurate to 5% or better. By the nature of SLR, the Galactic dust correction is inextricable from the photometric calibration when the instrumental stars are all behind the dust, so uncertainty from the dust must be added in quadrature. Finally, color terms carry with them additional uncertainty from the color term estimate and the colors that they multiply. If color terms are used, then the colors must be estimated independently from the the non-2MASS data,

---

[8] `http://irsa.ipac.caltech.edu/cgi-bin/Gator/nph-dd?catalog=fp_psc`

either simultaneously during the 2MASS fit or prior to it.

2MASS matches will probably only occur for a *subset* of one's instrumental data. The reduced number of stars will generically degrade the Stellar Locus Regression errors. Our optimized procedure is to first perform an instrumental-only SLR to estimate the colors using a maximal number of stars, and, if the photometry is needed at all, to perform a 2MASS SLR on the subset of matches to calibrate the photometry separately. This ensures that the color errors are minimal and not subject to the errors from 2MASS and from the reduced statistics. SLR never requires the subtraction of calibrated photometry to arrive at colors.

3.3.6 Goodness of Fit

During Stellar Locus Regression we optimize goodness-of-fit (GOF) statistics and estimate errors numerically. The GOF statistic we have adopted is the weighted, perpendicular color-distance residual.

The perpendicular color-distance is a hyper-dimensional distance in color space between an instrumental data point and the nearest point on the standard locus line. Our standard locus line is a collection of closely-spaced data points, so we make numerical approximations to calculate the distance. As we make explicit below, we first compute all possible distances between the instrumental colors and the points on the standard locus line, then we find the minimum distance for each instrumental data point. Finally we sum the result.

Consider instrumental color data points $\boldsymbol{c}_\alpha$, where α indexes the instrumental color data vector of each star. We compute the vector distances between every $\boldsymbol{c}_\alpha$

and every data point on our standard locus line, $\boldsymbol{c}_{0\beta}$, where $\boldsymbol{c}_{0\beta}$ is also an array of vectors and β varies along the standard locus line. These distances are $\boldsymbol{d}_{\alpha\beta} \equiv \boldsymbol{c}_{\alpha} - \boldsymbol{c}_{0\beta}$, where $\boldsymbol{d}_{\alpha\beta}$ is a tensor of all possible distances between the instrumental colors and the points on the standard locus line.

We weight the distances either by the number 1 or by the color measurement uncertainty in the direction of the line connecting each pair of points α-β. Whether to weight by unity or by color uncertainties is at the discretion of the user. We take the norms of each weighted distance vector, so our weighted distance measure is

$$|\boldsymbol{d}^{\mathrm{w}}_{\alpha\beta}| = \frac{|\boldsymbol{d}_{\alpha\beta}|}{|\boldsymbol{\sigma}_{\alpha} \cdot \hat{\boldsymbol{d}}_{\alpha\beta}|}. \tag{3.4}$$

Here the dot product $\cdot$ is taken between the vector of data uncertainties $\boldsymbol{\sigma}_{\alpha}$ and the unit vector that lies along the pairs of points $\hat{\boldsymbol{d}}_{\alpha\beta}$. The quantity $\boldsymbol{\sigma}_{\alpha} \cdot \hat{\boldsymbol{d}}_{\alpha\beta}$ is the uncertainty projected along the line that connects each pair of points.

Then, for each α, we select the one $\beta = \beta^*$ such that $|\boldsymbol{d}^{\mathrm{w}}_{\alpha\beta^*}| = \min(|\boldsymbol{d}^{\mathrm{w}}_{\alpha\beta}|)$. This is the closest distance to the standard locus line for the instrumental data point α. We do this for all data points α, and sum the results as

$$T = \sum_{\alpha} |\boldsymbol{d}^{\mathrm{w}}_{\alpha\beta^*}|, \tag{3.5}$$

noting that there is one β^* for each α. This is an estimate of the weighted distance residual between all instrumental data points and the standard locus line—a scalar.

Our SLR implementation produces best-fit calibration parameters by varying $\boldsymbol{\kappa}$ and adding it to the instrumental colors, then recomputing T, and repeating this process until T is minimized. We use the amoeba downhill simplex method (Nelder & Mead, 1965).

Our statistic was chosen for robustness. T would be equivalent to the χ^2 statistic if the distances were squared and weighted by the inverse variance[9], but the square puts undue weight on statistical outliers. Likewise, using uniform weights of unity, the residual of square perpendicular distances becomes equivalent to the so-called "total least-squares" statistic. This similarly gives undue weight to *non*-statistical outliers. We wish to apply SLR to any data at the telescope, on the fly, so robustness to outliers is critical.

To insure doubly against outliers, we perform SLR twice. The first iteration gives rough estimates of best-fit calibration parameters, allowing us to excise stars we deem to lie too far away from standard locus line. We typically cut stars with color distance $|\boldsymbol{d}_{\alpha\beta^*}| > 6|\boldsymbol{\sigma}_\alpha \cdot \hat{\boldsymbol{d}}_{\alpha\beta^*}|$ away from our standard locus line (a figure informed by Covey et al., 2007), and as well as those with $|\boldsymbol{d}_{\alpha\beta^*}| > 1\,\mathrm{mag}$. We then perform SLR once more on the cleaned data.

3.3.7 Uncertainty Estimation

We estimate all uncertainties on best-fit parameters with the bootstrap method (Efron, 1979). At each bootstrap iteration i we resample N_{stars} data points N_{stars} times with replacement to obtain a bootstrap sample, and perform the GOF optimization described above on the new sample. This gives best fit parameters $\boldsymbol{\kappa}_i$, which we record. We repeat this $N_{\mathrm{boot}} \sim 100$ to 1000 times, obtaining N_{boot}-size arrays of each vector $\boldsymbol{\kappa}_i$. The mean of each bootstrap distribution is an estimate of the sample

---

[9] In this case our GOF is closely related to the 7-dimensional color distance of Covey et al. (2007). The difference is that we weight by the errors in the direction of the line connecting the data and the nearest point on the standard locus line.

mean of each parameter. The standard deviation of the bootstrap distribution is an estimate of the standard error on the mean.

This approach means that to estimate uncertainties we repeat the entire stellar locus regression N_{boot} times. This can be time-prohibitive for large samples, but we argue it is not always necessary to repeat the error estimation after it has been performed once. If different stellar images are taken from the same instrument under similar circumstances, and if the bootstrap distributions are roughly normal, then errors for different size data sets can be estimated with rescaling by $\sqrt{N_{\mathrm{stars}}}$. This estimate may break down if those assumptions do not apply, but we argue $\sqrt{N_{\mathrm{stars}}}$ rescaling can give errors to a factor of a few for N_{stars} that are not wildly different. We now describe the full algorithm we have implemented to produce calibrated colors from flatfielded images.

3.3.8 An Algorithm

We have developed an optimized algorithm that produces SLR-calibrated colors from flatfielded images, essentially in real time. It is schematically outlined in Figure 3.3. The data undergo standard preprocessing, color terms are determined in the normal way from standard star frames *once*, and SLR fitting is done subsequently on all science frames.

SLR requires single-epoch multiband observations of any number of science fields and one standard star field. All images are bias-subtracted, flat-fielded, WCS-registered, and Source Extracted. The resulting instrumental catalogs from each passband are cross-correlated with one another to find the unique objects, and point-sources are

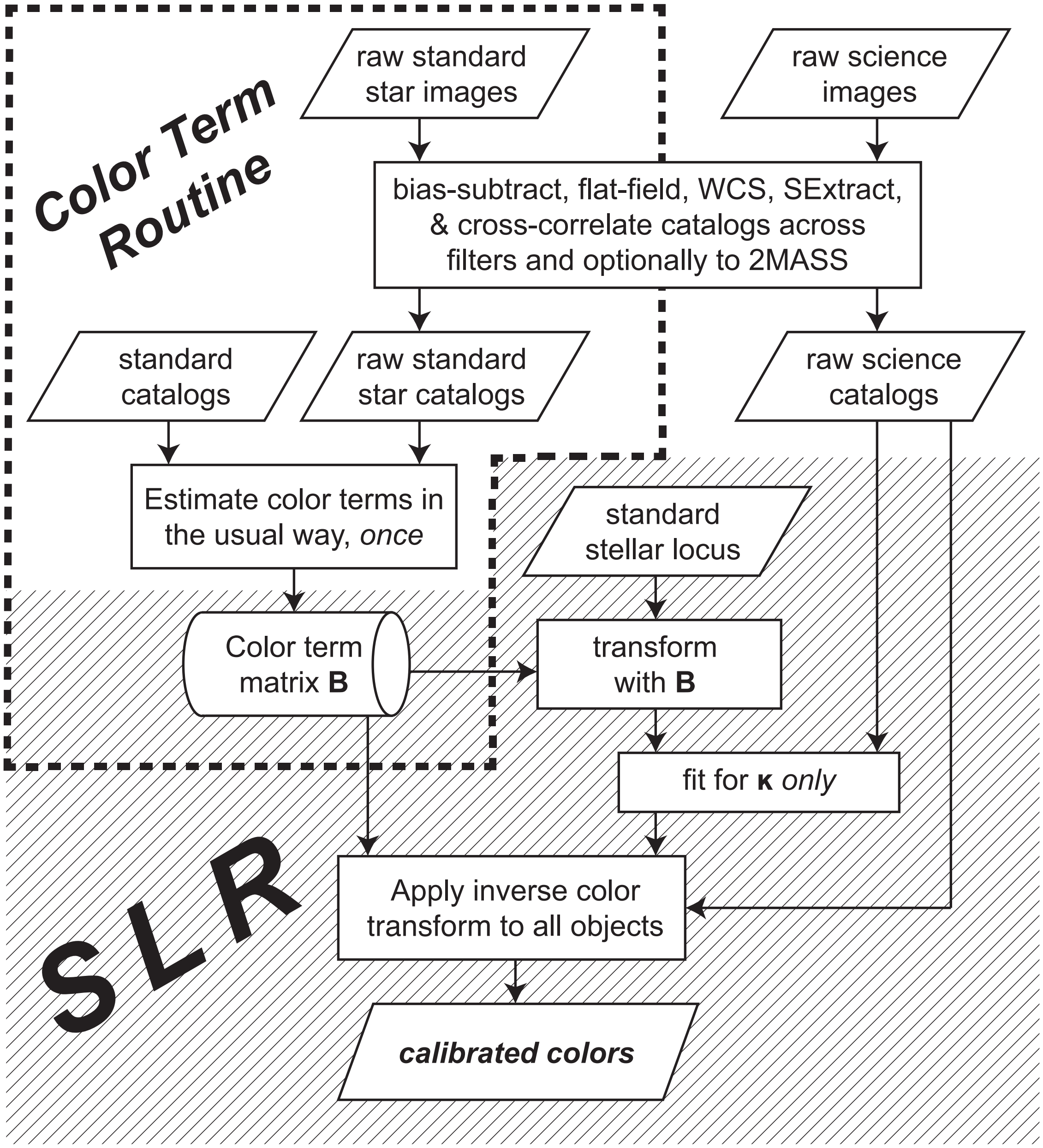

Figure 3.3: SLR flow chart for calibrating colors. The hashed region denotes parts of the algorithm that are unique to SLR, while the non-shaded region shows steps that are more traditional. The dotted region denotes the color term estimation routine, which need only be performed once per detector.

identified, for example, using Source Extractor's CLASS_STAR parameter. All stars are required to be unambiguously identifiable in all bands, and at all stages we only consider those with signal-to-noise > 10.

Instrumental color terms are then determined once only from the standard star field, in the traditional way. For example, following the equations of §3.8 we estimate the g-band color term b_g as the slope of the best-fit line to $g - g_0$ vs. $g_0 - r_0$, and so forth for the rest of the passbands. The color terms are stored as the color term matrix $\mathbf{B}$.

With color terms in hand, real-time SLR calibration of any number of science fields can be undertaken. The color terms are first applied to the standard stellar locus with the transform $(\mathbf{1} + \mathbf{B})$, bringing the standard locus into *standardized instrumental color space*. In this space, the instrumental stellar colors from the flat-fielded science images are regressed to the standard locus, leaving only the color translation vector $\boldsymbol{\kappa}$ free. This stage can be executed as soon as flat-fielded multiband images are in hand. Flat-fielding and object cataloging can be performed at the telescope during observation, so Stellar Locus Regression is viable as a real-time calibration technique.

The instrumental science catalog of both point-like and extended sources is calibrated by applying the inverse color transformation,

$$\boldsymbol{c}_0 = (\mathbf{1} + \mathbf{B})^{-1} (\boldsymbol{c} - \boldsymbol{\kappa}) . \tag{3.6}$$

$\mathbf{B}$ was determined from the standard star observations, and $\boldsymbol{\kappa}$ was obtained from the SLR. The transform $(\mathbf{1} + \mathbf{B})$ is invertible under normal circumstances of small color terms (see §3.8).

As outlined in §3.3.5, SLR generates calibrated magnitudes using 2MASS entries using exactly the color calibration process described above, with judicious choices of color vector entries. The additional step of matching one's instrumental objects to 2MASS lasts seconds to minutes for typical catalogs containing of order tens to hundreds of stars.

We apply this algorithm to real data in a series of test, presented in the following section.

3.4 First Tests

We employed the algorithm of §3.3.8 on existing, calibrated SDSS data and on new *griz* data we have acquired on the 6.5 m Magellan telescopes using the IMACS (Dressler et al., 2003b; Osip et al., 2008b) and LDSS3 (see Osip et al., 2008b) instruments in imaging mode. We designed a series of tests to isolate the effect of Galactic extinction and airmass and to generally assess the reproducibility of colors using SLR. Finally, we used SLR in a measurement of redshifts of 11 galaxy clusters using colors alone.

3.4.1 Galactic Extinction

The majority of SDSS stars at high Galactic latitude are expected to be behind the dust (§3.2), so we designed a simple test of SLR to measure the extinction directly. We applied SLR to ubercalibrated (Padmanabhan et al., 2008) SDSS stars subject to varying degrees of predicted reddening, and compared the results to SFD expectation. Ubercal SDSS data are calibrated to the top of the atmosphere, in front of the Galactic dust. We therefore expect the best-fit color vector κ to be equal to the reddening vector, especially at high Galactic latitudes, and we expect the canonical $R_V = 3.1$ extinction law to hold.

We began by querying photometric quality ubercalibrated SDSS point sources from the CasJobs web server[10]. Photometric quality ubercalibrated colors are accurate over a wide area of the sky, with 1.5% estimated uncertainty, so this is the ideal SDSS data set to perform our test on, in terms of size and quality. We queried stars in small ranges of SFD-predicted extinction and performed multiple such queries over a wide range of mean extinctions. The results were samples of hundreds of stars each in finite Galactic extinction bins over a wide range of SFD dust columns. We selected stars with signal-to-noise ratio > 10 in all bands to minimize uncertainty from poor color measurement.

Figure 3.4 displays three of these data sets. Low ($A_g \sim 0.05\,\mathrm{mag}$), intermediate ($A_g \sim 0.5\,\mathrm{mag}$), and high ($A_g \sim 1.2\,\mathrm{mag}$) Galactic extinction ranges were queried, as shown in the figure. Histograms of the SFD-predicted extinction in the g-band for each star show that these extinction distributions are localized and well separated. The gross effect of Galactic reddening is readily apparent in color-color diagrams (top panels).

In total we acquired 7 such data sets, sampled from the northern and southern Galactic hemispheres, probing mean A_g between 0.05 and 1.2 mag. By nature of the SDSS database organization and the available data itself, the data sets happen to come from fields that are localized to $\sim 1\,\mathrm{deg}^2$, except for one. The Galactic coordinates are given in Table 3.3. The last field in Table 3.3 shows a wide range of

---

[10] `http://casjobs.sdss.org/CasJobs/`

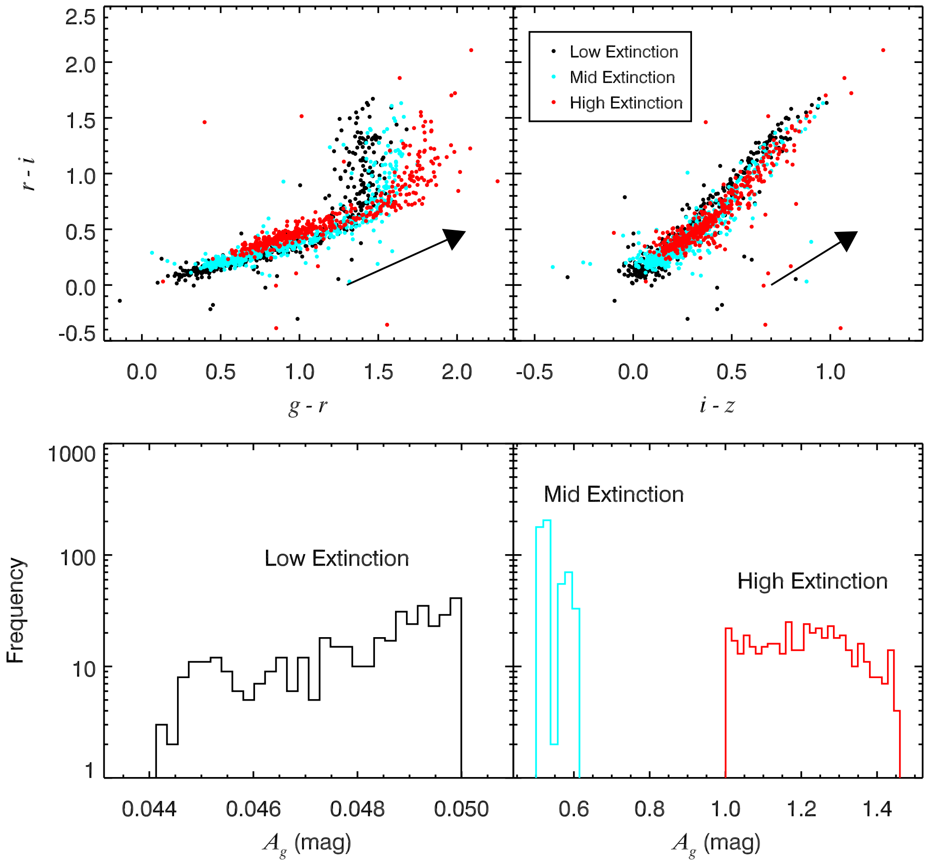

Figure 3.4: Three samples of SDSS stars with different ranges of predicted Galactic extinction (low: $A_g \sim 0.05\,\mathrm{mag}$, intermediate: $A_g \sim 0.5\,\mathrm{mag}$, and high: $A_g \sim 1.2\,\mathrm{mag}$). *Top panels*: color-color stellar loci, shown with the canonical reddening unit vector in three-dimensional color space. *Bottom panels*: histograms for predicted g-band Galactic extinction.

stellar coordinates because the CasJobs query, by chance, returned stars spread over a few disjointed regions of the sky.

Table 3.3: Galactic Extinction Fields.

Mean A_g (mag)	ℓ (deg)[a]	b (deg)[b]
0.048	57.9 ± 1.0	37.9 ± 0.5
0.538	15.8 ± 0.2	29.0 ± 0.2
1.210	11.4 ± 0.1	36.2 ± 0.1
0.090	130.6 ± 0.9	-49.0 ± 0.2
0.268	115.2 ± 0.4	-48.7 ± 0.1
0.727	149.8 ± 0.4	-46.6 ± 0.1
1.068	56.6 ± 33.9	-37.5 ± 3.1

We performed Stellar Locus Regressions on each data set. We fixed the color term matrix **B** to zero because this test involved comparing a standard stellar locus standardized to the SDSS photometric system, to colors generated by the SDSS instrument itself. After our restrictions on the data were enforced (see §3.3.6), between 380 to 490 stars from each data set were ultimately used in the fits. The best-fit

---

[a] Mean and standard deviation of Galactic longitudes for stars in the sample.

[b] Mean and standard deviation of Galactic latitudes for stars in sample.

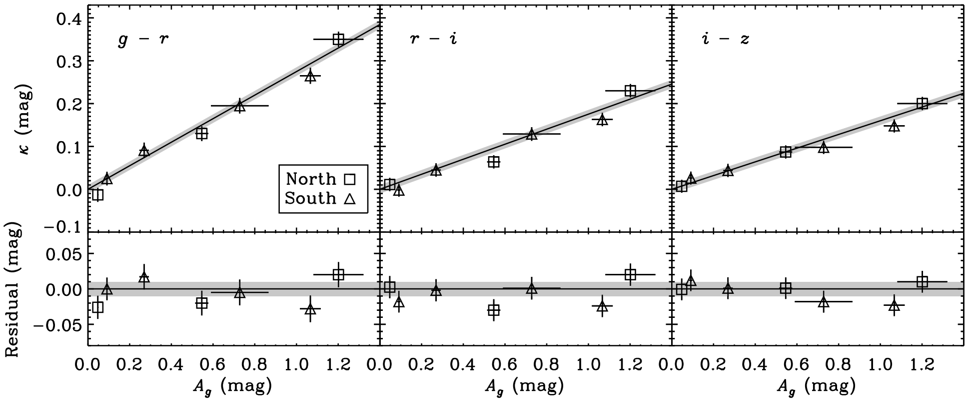

Figure 3.5: Best-fit color shifts $\boldsymbol{\kappa}$ vs. predicted Galactic extinction in the g-band, and residuals. The solid lines are the SFD-predicted reddening corresponding to the g-band extinction given on the abscissa. Northern and southern Galactic hemisphere fields are indicated, and the ±10 mmag region is shaded.

color shifts $\boldsymbol{\kappa}$ that resulted are directly compared to the SFD-predicted reddening in Figure 3.5. The expectation, if our hypotheses hold, is that $\boldsymbol{\kappa}$ will be equal to the reddening vector.

The solid lines in Figure 3.5 show the *predicted* color-reddening values $A_n - A_m$, $n, m \in \{g, r, i, z\}$ corresponding to the predicted g-band extinction given on the abscissa, assuming the canonical $R_V = 3.1$ reddening law. The error bars for the abscissa are the standard deviation of predicted extinction values for the corresponding data set. Error bars for the ordinate are the standard error on the mean predicted reddening added in quadrature to the bootstrap errors of SLR and the 1.5% color uncertainty limit to which ubercalibrated colors are subject.

The best-fit color shifts from SLR are consistent with Galactic reddening within the errors for these data, with residual RMS of 19 mmag in the color $g - r$, 18 mmag in $r - i$, and 13 mmag in $i - z$. The maximum residual disagreement is 30 mmag in

$g - r$ and $r - i$, and 19 mmag in $i - z$.

Ivezić et al. (2007) performed a similar analysis in SDSS Stripe 82 with their "stellar locus method," showing maximum sensitivity to the magnitude of SFD extinction at roughly the 20 mmag level at high Galactic latitudes. Their measurements showed disagreement with SFD prediction at Galactic latitudes $|b| \sim 40$–50 deg and below (their §2.7.1). Our results probed latitudes in this range and lower, but in fields from different Stripes, so our results are not inconsistent with theirs. In other tests (§3.4.2), we observed Stripe 82 fields where their stellar locus method failed, and we reproduced their results. Taking this information together, we conclude that stellar locus methods *can* reproduce the $R_V = 3.1$ reddening law in both magnitude and direction, even through significant dust columns, so dust thickness alone is not a good indicator of SLR reliability.

3.4.2 Color and Magnitude Reproducibility

We tested the ability of SLR to reproduce colors and magnitudes using data acquired at different telescopes. We chose Stripe 82 fields because of the high quality, 1% photometry available from Ivezić et al. (2007). We probed fields that contained among the highest densities of stars in the entire Stripe 82 in order to minimize statistical uncertainty. The stars in these regions, however, are known not to reproduce the SFD extinction prediction with stellar locus methods (§2.7.1 of Ivezić et al., 2007). The possible reasons cited were an invalid extinction law R_V, a drift in mean metallicities, or dust that was both in front of and behind the stars. Nonetheless, we designed our experiment to control for the anomalous dust, as described below, so that we could study in isolation SLR's fundamental ability to reproduce colors and magnitudes when applied to data from different instruments.

In 2008 we undertook observing programs at the 6.5 m Magellan telescopes using the IMACS instrument in imaging mode. We observed three, high stellar density Stripe 82 fields, which we label S1, S2, and S3. Our field S1 is centered at $(\ell, b) = (48.65151, -26.04729)$ deg, S2 at $(\ell, b) = (51.86849, -33.74441)$ deg, and S3 at $(\ell, b) = (50.43107, -30.24483)$ deg. These fields are all at lower Galactic latitude $|b|$ than those of §3.4.1, except for the second field shown in Table 3.3. Each IMACS CCD is $4' \times 8'$, arranged in two rows of four. Just as we have described in §3.3.8, we flat-fielded the data and produced instrumental, multiband catalogs. We associated stars between passbands by requiring their positions to agree to better than $1''$ in radius. We then found the corresponding photometry in the catalog of Ivezić et al. (2007) in the same way, selecting only those stars with more than 4 SDSS observations per passband and with signal-to-noise > 10.

In order to compare the colors of stars directly, we treated the SDSS catalog data as pseudo-IMACS observations: we extracted only the stars that also appeared in the 8 IMACS CCDs, in all *griz* bands. This was repeated for the three fields. Because we wished to compare SLR magnitudes in addition to colors, we also found the 2MASS J-band photometry for the stars. Of order 10–100 stars per CCD per field were matched across the IMACS, SDSS, and 2MASS data sets.

Following the procedure outlined in §3.3.3 and §3.3.8, we measured the IMACS color terms from the SDSS standard stars. We exploited the fact that we observed 3 standard fields, and measured color terms independently in all of them, one CCD at a time, taking the average of the result. We applied the same mean color term correction to all CCDs. This color term procedure gave smaller color and magnitude residuals than (1) using different mean color terms for each CCD and (2) using separate color terms for each field *and* CCD.

First, we ran SLR to calibrate only the colors. We controlled for the anomalous stellar locus shifts by regressing both the calibrated SDSS data and our instrumental colors to the standard locus line. The best-fit $\boldsymbol{\kappa}$ for the SDSS data showed color translations that disagreed with SFD prediction by $\sim$ 50–100%, consistent with the findings of Ivezić et al. (2007). By applying SLR to both the instrumental and SDSS data sets, we effectively canceled the anomaly by subtraction.

In a separate, subsequent step we calibrated the photometry using SLR, fixing the optical-only color shifts to those measured in the first step, as described in §3.3.5 and §3.3.8. We solved for the SLR-standardized photometry as

$$g_0 = g - \kappa_{gJ} - b_g(g_0 - r_0) \tag{3.7a}$$

$$r_0 = r - \kappa_{rJ} - b_r(r_0 - i_0) \tag{3.7b}$$

$$i_0 = i - \kappa_{iJ} - b_i(i_0 - z_0) \tag{3.7c}$$

$$z_0 = z - \kappa_{zJ} - b_z(i_0 - z_0) \tag{3.7d}$$

where the color terms b_n were the measured values for the IMACS catalogs, and zero for the SDSS catalogs. For the colors on the right-hand side, we used the SLR calibrations from the first, optical-only color iteration. The κ_{gJ}, κ_{rJ}, *etc*, were those obtained from the second, optical-infrared magnitude iteration of SLR.

Figures 3.6 and 3.7 show the resulting color and magnitude residuals. The figures show a lack of pronounced systematic error in SLR colors as a function of effective temperature, $g-i$. We assess that colors calibrated purely with SLR are reproducible between the SDSS and the IMACS instruments to $(18, 6, 5)$ mmag in the colors $(g-r, r-i, i-z)$. Magnitudes obtained only with SLR, using 2MASS, are reproducible between IMACS and SDSS to $(44, 25, 19, 9)$ mmag in the (g, r, i, z) passbands. These numbers do not include the Galactic dust uncertainty because we applied SLR to both data sets, but they do necessarily include the intrinsic airmass correction that SLR makes. Our following test isolated completely the effect of the atmosphere using IMACS data alone.

3.4.3 The Atmosphere

We again tested the reproducibility of SLR-calibrated colors, this time isolating and varying the effect of atmospheric extinction. An advantage to the SLR approach is that is does not assume any particular functional dependence of color variation with airmass (§3.3.2). We therefore expect precise airmass corrections from SLR.

We isolated the effect of the atmosphere by performing SLR on the *same sets of stars* observed through 2 different airmasses using the same instrument, and compared directly the SLR-calibrated colors of the matched stars. We observed the IMACS fields described in §3.4.2 through multiple airmasses with the *griz* passbands. We included two additional fields, S5 at $(\ell, b) = (122.46159, -63.21097)$ deg and CL1 at $(\ell, b) = (96.07818, -61.31761)$ deg—the latter of which we observed at three different airmasses. The field S5 is in Stripe 82, but did not contain enough matches between IMACS, SDSS, and 2MASS to include in the analysis of §3.4.2. The field CL1 is not in the SDSS footprint.

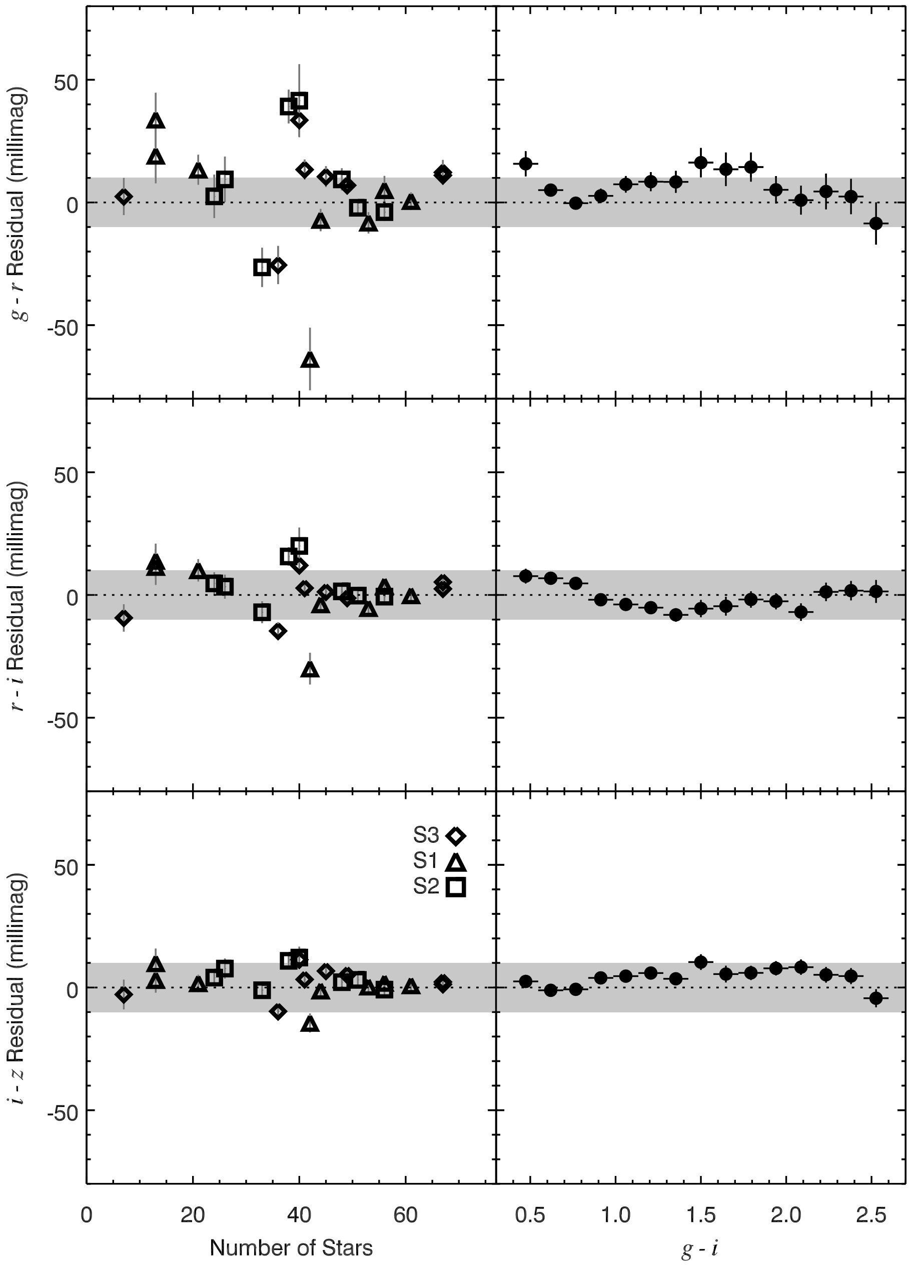

Figure 3.6: SLR color reproducibility, where SLR was applied both to SDSS and new IMACS observations. Color residuals are plotted vs. number of stars used per SLR (*left panels*) and vs. true $g - i$ color (*right panels*). Each data point on the left represents an SLR calibration done on one CCD, and residuals vs. $g - i$ are averaged over the union of all stellar residuals across all fields and CCDs. The ±10 mmag region is shaded.

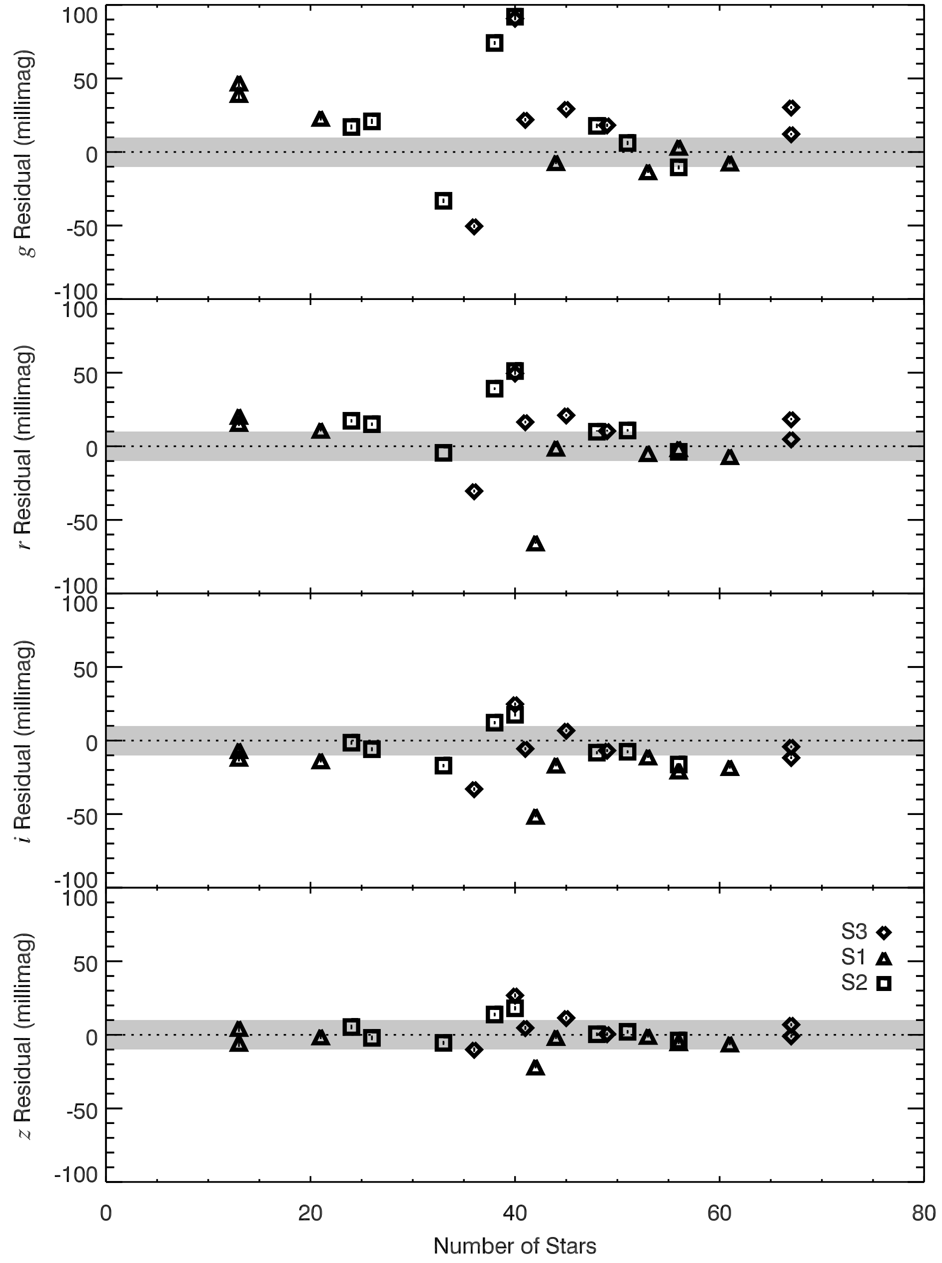

Figure 3.7: SLR magnitude reproducibility, where SLR was applied both to SDSS and new IMACS observations. A 2MASS SLR magnitude calibration was performed, again on both data sets as in Figure 3.6, with one data point per CCD. The ±10 mmag region is shaded.

The data preprocessing was identical to that of §3.4.2, except here we applied the nonzero color term corrections to all IMACS data, and we did not cross-correlate with 2MASS as we only wish to examine colors.

Figure 3.8 shows the results. The left panel shows the weighted mean residuals of stellar colors per CCD per field, with bootstrap errors, plotted against the number of useful stars extracted from each CCD. The right hand panel shows the mean of each set of 8 data points per field, with error bars reflecting the RMS scatter, plotted vs. the airmass ratio of the two observations. CL1 was observed at three airmasses, and the highest two airmasses are each paired with the lowest airmass in this figure.

This shows that SLR colors are reproducible over a wide range of airmasses, with residual RMS scatter in $(g-r, r-i, i-z)$ of $(14, 8, 5)$ mmag when the number of stars used is > 30, and $(20, 10, 8)$ mmag overall. Color errors do not correlate well with increased airmass. As is expected, there is a dependence of the color errors on the number of stars used per regression. The reduced χ^2 of the fits are roughly in the range $[1, 3]$, with larger values for bluer bands. The larger N_{stars} data exhibit slightly larger χ^2, and smaller N_{stars} data exhibit slightly smaller χ^2. This suggests that the bootstrap slightly overestimates errors at small N_{stars}, and slightly underestimates errors at larger N_{stars}. This may be due to mildly non-Gaussian distributions. Overall, these results suggest that SLR systematic errors are not dominated by airmass issues for the fields we tested, but instead are dominated by the statistical noise inherent to the method as applied to the particular data we have used it on here.

As our final test, we deployed SLR colors in a photometric redshift measurement, as distance estimation is one of the prime uses of accurately calibrated colors.

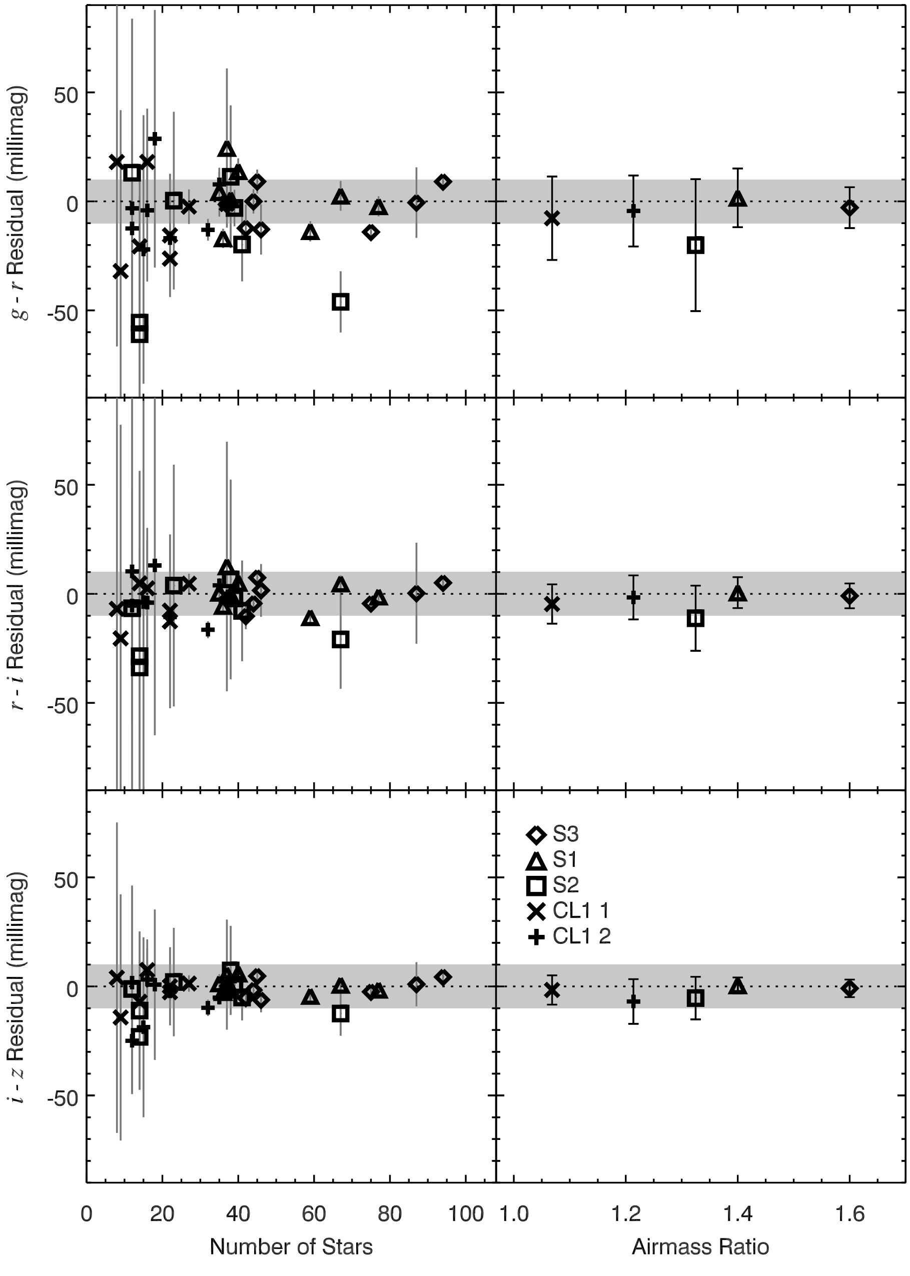

Figure 3.8: Color residuals between SLR calibrations of fields imaged with IMACS at different airmasses. The ±10 mmag region is shaded. *Left hand plots:* Residuals vs. number of stars used to perform each SLR. *Right hand plots:* Mean of residuals over the 8 IMACS CCDs vs. airmass ratio between the two observations, and error bars are the RMS of residuals per field.

3.4.4 Galaxy Cluster Redshifts

We used SLR-calibrated colors to recover the redshifts of galaxy clusters. As part of the 2008 observing program we mentioned in §3.4.2 and §3.4.3, we observed known galaxy clusters from the REFLEX catalog (Böhringer et al., 2004b), primarily a subset that are also Abell clusters (Abell et al., 1989b). These observations were acquired with the LDSS3 camera at the Magellan 6.5 m telescopes (see Osip et al., 2008b) in imaging mode. Because the redshift of the clusters are known, this serves as a test of our color calibrations within the context of a full scientific analysis.

We estimated LDSS3 color terms using standard star fields. Individual SLR calibrations were then obtained directly from each of the single-epoch $griz$ cluster fields, and the $\mathbf{B}$ and best-fit $\boldsymbol{\kappa}$ applied to the galaxy colors without applying any further corrections for airmass or Galactic extinction. We then selected the brightest red-sequence cluster galaxies from color-magnitude diagrams, spanning $\sim$ 1–2 mag fainter than the brightest cluster galaxy (BCG) magnitude. This typically included of order 10 galaxies. We calculated the weighted mean of their $g - i = (g - r) + (r - i)$ colors and estimated the cluster redshift with the empirical color-to-redshift tables of Lopes (2007). For the low redshift range we probed, the $g - i$ color of red cluster galaxies varies rapidly and monotonically with redshift and is an ideal redshift estimator.

Table 3.4 summarizes the galaxy clusters we targeted, along with their Galactic coordinates and our results. The Abell systems 3693 and 3738 have been identified by previous authors as multi-redshifts systems. We were able to isolate the subsystems using color-magnitude diagrams and image inspection, and we estimated their redshifts independently.

Table 3.4: Summary of the Cluster Data and Results.

Name	References[a]	Redshift		Airmass[d]	Seeing[e]	E_{g-i}[f]	N stars[g]	b[h]
		Spec[b]	SLR[c]		(arcsec)	mag		(deg)
ABELL 3668	1, 2	0.1496	0.156 ± 0.011	1.9	2.0–3.0	0.083	58	−32
ABELL 3675	1, 2	0.1383	0.150 ± 0.012	1.9	1.8–1.9	0.079	67	−35
RXC J2023.4-5535	2	0.232	0.238 ± 0.012	1.7	1.7–2.3	0.102	70	−35
ABELL 3693	1, 3, 4	0.091	0.093 ± 0.016	1.5	1.8–3.0	0.060	62	−35
ABELL 3693	1, 4, 5	0.123	0.120 ± 0.016	1.5	1.8–3.0	0.060	62	−35
ABELL 3739	1, 2	0.1651	0.177 ± 0.010	1.3	1.6–2.1	0.054	63	−42
ABELL 3739	1, 6, 7	0.1786	0.183 ± 0.010	1.3	1.6–2.1	0.054	63	−42
ABELL 3740	1, 3	0.1521	0.141 ± 0.007	1.3	1.4–2.7	0.086	39	−42

Continued on next page…

Table 3.4 – Continued

Name	References[a]	Redshift		Airmass[d]	Seeing[e]	E_{g-i}[f]	N stars[g]	b[h]
		Spec[b]	SLR[c]		(arcsec)	mag		(deg)
ABELL 3836	1, 3	0.11	0.120 ± 0.007	1.3	1.4–2.7	0.032	32	−51
RXC J2218.6-3853	8	0.1379	0.138 ± 0.022	1.5	1.2–1.9	0.026	12	−56
ABELL 3866	1, 9	0.1544	0.156 ± 0.008	1.4	1.1–1.9	0.020	22	−57
ABELL 3888	1, 10	0.152912	0.159 ± 0.016	1.4	1.3–1.9	0.029	28	−59

Continued on next page…

Table 3.4 – Continued

Name	References[a]	Redshift		Airmass[d]	Seeing[e]	E_{g-i}[f]	N stars[g]	b[h]
		Spec[b]	SLR[c]		(arcsec)	mag		(deg)
AM 2250-633	9, 11	0.2112	0.204 ± 0.014	1.2	1.1–1.4	0.046	26	−49

---

[a] References—(1) Abell et al. (1989b), (2) Böhringer et al. (2004b), (3) Struble & Rood (1999), (4) Katgert et al. (1996), (5) Zaritsky et al. (2006), (6) Voges et al. (1999), (7) Schwope et al. (2000), (8) Cruddace et al. (2002), (9) de Grandi et al. (1999), (10) Pimbblet et al. (2006), (11) Arp & Madore (1987).

[b] Spectroscopic redshift reported by references.

[c] Photometric redshift based on SLR color corrections, with standard errors on the mean redshift estimates of the brightest cluster member galaxies.

[d] Airmass at which the images were obtained.

[e] Range of seeing in the multiband images.

[f] SFD-predicted Galactic reddening in $(g - i)$.

[g] Number of stars used to determine the SLR color correction.

[h] Galactic latitude of the cluster.

The results for the 11 clusters are plotted in Figure 3.9. The $g-i$ cluster color errors SE_{gi} were estimated as the standard error on the mean $g-i$ color of the red sequence galaxies we selected, and cluster redshift errors were taken to be $\mathrm{SE}_{gi}/3$, taken from the slope of the color-redshift relation of Lopes (2007). The reduced χ^2 of residuals is 0.6, so this error slightly overestimates the scatter. The residual cluster redshift RMS is $\sigma_z = 0.007$, or $\sigma_z/(1+z) = 0.6\%$ for the range of redshifts we measured. We emphasize that this is the estimated redshift error not per red galaxy, but per cluster, each of which made use of an ensemble of red galaxies.

The $\sigma_z = 0.007$ RMS error corresponds to $g-i$ color errors of $\sim 20\,\mathrm{mmag}$, again estimating from the roughly linear relationship between redshift and $g-i$. This level of residual error is roughly in accord with the SLR systematic errors due to Galactic dust and the atmosphere, estimated in §3.4.1, §3.4.2, and §3.4.3, and the residuals are inconsistent with erroneous Galactic dereddening. If Galactic extinction were completely unaccounted for by our calibration method, redshifts would lie along the dashed line of the right-hand panel of Figure 3.9, assuming no other systematic effects. Because our redshift residual trend is not consistent with the dashed line, these results provide further evidence (see §3.4.1) that SLR accounts for Galactic extinction in these fields.

3.5 Discussion

We have provided a new way to calibrate instrumental photometry. It differs substantially from traditional techniques, and so a side-by-side comparison of SLR with traditional approaches is in order. This the first item of discussion. We then list

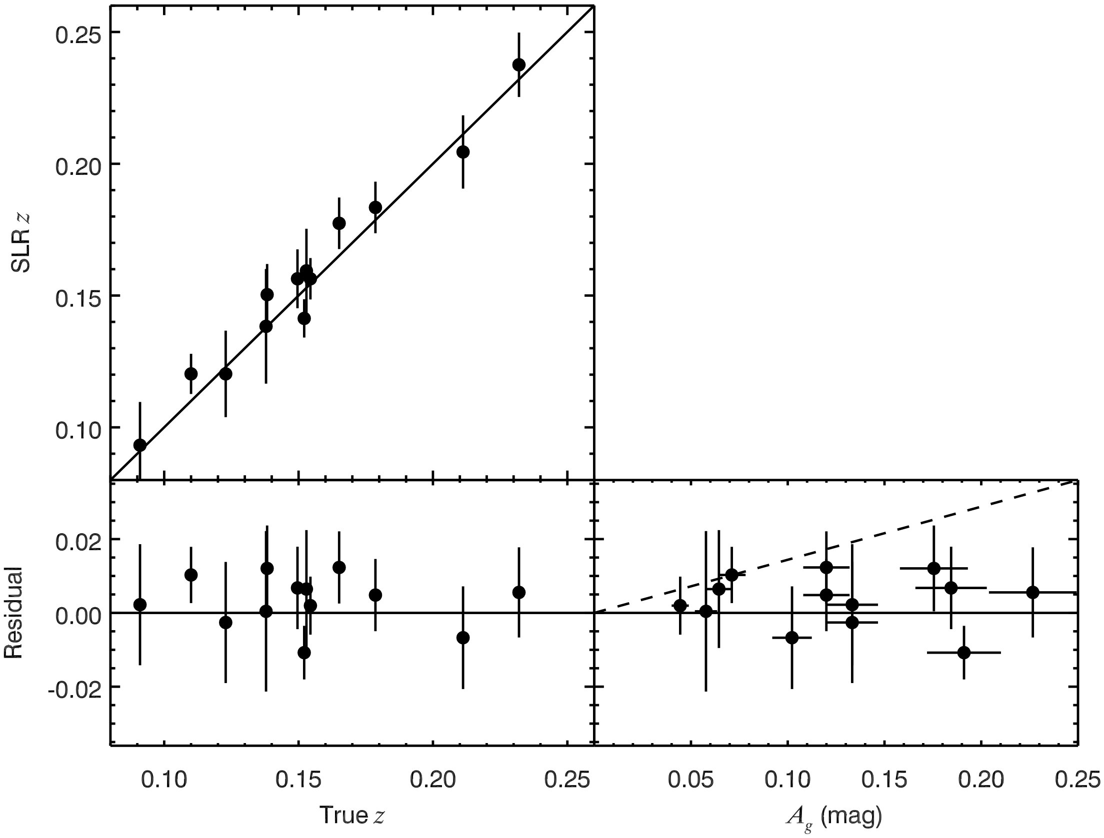

Figure 3.9: Photometric galaxy cluster redshifts from SLR-corrected colors vs. spectroscopic redshifts, and residuals. *Right panel:* Redshift residuals vs. expected g-band Galactic extinction. The dashed line is the redshift error expected using colors that are not corrected for Galactic extinction. There is no evidence for a redshift residual correlated with Galactic extinction, indicating that SLR makes an appropriate correction.

in detail the unique advantages and limitations of SLR, and complete our discussion with tasks for the future.

3.5.1 SLR vs. Traditional Photometric Calibration

3.5.1.1 Traditional Photometric Calibration

The traditional path to calibrated colors has been to first calibrate magnitudes, then to subtract them. Magnitudes are calibrated by tying instrumental flux to photometric standard stars, which most often requires additional exposure time investment outside one's field of scientific interest. The resulting zeropoints must be interpolated in space and time to the science fields, but only after extinction by the atmosphere is modeled and measured—which necessitates further standard field observations over a wide range of zenith angles.

The analysis of these data to extract calibrated colors traditionally involves the steps of:

1. Bias subtraction and flat-fielding;
2. Extracting instrumental magnitudes for all images, in all bands;
3. Using either observations of standard stars or program objects over a substantial span of zenith angles, in each band, to determine atmospheric extinction coefficients, and correcting each observation for atmospheric extinction;
4. Assessing whether the atmospheric conditions during observation were photometric, and thus whether the zeropoint and atmospheric extinction interpolations are valid;

5. Correcting for the frame-by-frame difference between PSF-fitting magnitudes and aperture photometry;
6. Determining and correcting for any differential sensitivity mismatch between the instrument and the desired photometric system, and applying these color term corrections to the photometry;
7. Determining Galactic extinction in the direction of the observation from some external source such as SFD, and making an appropriate correction to all magnitudes; and
8. Generating colors of sources of interest by subtracting these fully calibrated apparent magnitudes.

The result of this procedure is a source catalog that contains magnitudes and derived colors. Besides being costly in telescope time, this procedure is also suffers from extra uncertainty from the explicit mathematical modeling of atmospheric attenuation. Moreover, the individual magnitudes must each be calibrated to a better fractional precision than the desired color error. In the future, when high accuracy all-sky photometric catalogs of faint sources are readily available in all bands of interest, this process will be somewhat simplified. In the meantime we offer the SLR approach. SLR renders the preliminary magnitude calibration step unnecessary, instead allowing for the direct determination of colors of all objects of interest. SLR also provides a way to calibrate the photometry by tying the magnitude scale to the all-sky 2MASS catalog, again without the need for extra standard star observations.

3.5.1.2 SLR Photometric Calibration

The SLR approach matches the distribution of stars in the instrumental color-color space to a standard stellar locus, allowing us to replace the traditional analysis path with a streamlined set of steps.

1. For each previously uncharacterized instrument, we observe only one field that contains stars whose calibrated magnitudes are known. This allows us to establish, in the traditional way, the instrumental color terms that arise from filter and detector differences.

2. All subsequent images are bias subtracted and flat-fielded.

3. Instrumental magnitudes are extracted for objects in each image.

4. Objects are immediately cast in instrumental color-color space, and we determine the transformations needed to bring the instrumental stellar locus into agreement with the universal, calibrated color properties of stars.

5. This color transformation is then applied to all photometry, producing calibrated colors for all measured objects.

6. If desired, calibrated photometric zeropoints are determined by bootstrapping the photometry to any stellar photometric catalog that overlaps the program fields. At the time of this writing, 2MASS is the obvious choice.

The result is a catalog of colors, and optionally magnitudes that are calibrated in a separate step and whose uncertainties do not factor into those of the colors. As a fundamentally different calibration technique, SLR has unique (in)sensitivities to astrophysical and instrumental effects. We break out the unique advantages and limitations these afford.

3.5.2 Advantages

SLR corrects for atmospheric extinction, even if time-variable. Atmospheric extinction distorts the apparent colors of celestial sources, compared to what would be observed at the top of the atmosphere. To first approximation, this produces a translation of stars in color-color space. The atmospheric transmission function is expected to change as a function of time, zenith angle, and azimuthal angle as parcels of aerosols and water vapor travel and evolve in the sky (cf Stubbs et al., 2007). Traditional airmass and zeropoint interpolations cannot account for this, unless specially designed systems to monitor atmospheric conditions along the line of sight are deployed in parallel during observation. Moreover, the $\sim X^{1/2}$ airmass dependence of saturated water lines in the z-band is simply not modeled by most observers (§3.3.2). SLR is unique because it naturally corrects for all of these additive effects at once with $\boldsymbol{\kappa}$, and is therefore insensitive to any additive mis-modeling of atmospheric extinction. We showed in §3.4.2 and §3.4.3 that SLR corrects for atmospheric attenuation in the z-band with sub-percent accuracy. Our SLR formalism also supports color-airmass corrections, but we have shown that we already achieve high quality atmospheric corrections through a wide range of airmasses without these.

SLR corrects for attenuation through clouds. As long as the exposures are long enough to homogenize the extinction due to clouds blowing across the images being analyzed, then the SLR technique will compensate for a common flux diminution across each frame. Integration times that exceed 60 seconds typically satisfy this, even for images that span a degree on the sky. The multi-epoch SDSS Stripe 82 analysis of Ivezić et al. (2007) supports the assertion that we can treat the effect of clouds as "grey" extinction, which SLR corrects for at once with $\boldsymbol{\kappa}$.

SLR corrects for passband sensitivity differences, even across different instruments and telescopes. An overall multiplicative difference between the system throughput vs. wavelength of two different cameras or telescopes can be caused by filter transmission functions, detector quantum efficiency, and other instrumental properties. These are some reasons the nominal zeropoints between two facilities are not equal. We have shown that SLR accounts for zeropoints in all tests we performed (§3.4). *Differential* variation in system throughput vs. wavelength brings about disagreements in apparent magnitudes and colors that change with objects' color. The SLR technique takes these into account by applying traditional color terms, measured from infrequent standard star observations. In color-color space, these cause apparent colors to scale, shear, and rotate. Our SLR methodology fully permits color term correction, and we have demonstrated this in §3.4.2 and implicitly in §3.4.4 using two different cameras.

SLR circumvents aperture corrections and photometric artifacts from PSF variations. Because the SLR technique maps observed, instrumental magnitudes onto a standard stellar locus, even if photometry from a given image in a given passband has some systematic photometry error from PSF-related issues, the applied color transformation will correct for these artifacts. Differences in aperture corrections between passbands produce a common displacement in color-color space. Ivezić et al. (2007) showed that using the stellar locus to correct colors of galaxies works well for photometry obtained with the SDSS analysis pipeline. We have demonstrated in §3.4.4 that applying SLR to Source Extractor instrumental magnitudes produces photometric redshifts that are in excellent agreement with spectroscopic redshifts, without additional aperture corrections.

SLR avoids the need to take more than a single calibration frame per instrument, per filter. The universality of the stellar locus in effect allows the colors from a set of multiband images to be self-calibrating. We find that taking only one set of multiband images of a calibration field is required, to determine the instrumental color terms. At all times thereafter, on timescales of months or years, and as long as there is a sufficient number of stars ($\gtrsim 10$) in each image being analyzed, there is no need to obtain additional calibration frames. Our galaxy cluster observations of §3.4.4 used color terms measured only once in an SDSS standard star field.

SLR corrects for Galactic extinction, independent of A_V and R_V. Whatever processes might bring about an overall observed displacement of the stellar locus, SLR will make the appropriate correction as long as it is locally well correlated. This includes Galactic reddening effects when the stars are behind the dust. Because a single global color correction is applied to all the data, the cataloged objects should span a sufficiently small region on the sky to assure they have a common Galactic reddening. We showed in §3.4.1 that SLR can recover the canonical reddening through very high and very low dust thicknesses to $\sim 20\,\mathrm{mmag}$ in color. We point out that our photometric redshift analysis in §3.4.4 made no explicit dust correction of any kind, and results were nonetheless consistent with an intrinsic Galactic dereddening by SLR. The anomalous extinction results of §3.4.2 are suggestive of possible deviations from the typically assumed reddening law—although drifts in mean metallicity cannot be ruled out as yet.

SLR takes advantage of all stars in the images, producing a "democratic" color calibration. For fields of view that are currently typical of astronomical imaging instruments, Galactic stars are approximately uniformly distributed across the image. SLR allows for the calibration of all objects in a field using the very stars appearing in that field. As long as there are no effects that vary across the field of view, the SLR color calibration technique inherently produces a homogenized calibration of colors across the frame.

SLR uses a single common standard stellar locus, and thereby reduces sensitivity to systematic errors in photometric zeropoints. The photometry from SDSS exhibits zeropoint drifts at the few percent level across the sky (Padmanabhan et al., 2008). If these cataloged magnitudes are used to derive local colors, the colors inherit a position-dependent systematic drift that is the difference between the underlying photometric zeropoint errors. SLR uses a single common standard stellar locus for all color corrections, so the derived colors should show reduced position-dependent systematic errors. The *precision* of SLR-derived colors should be outstanding. The *accuracy* of SLR-derived colors depends upon the accuracy of the standard stellar locus, the extent to which this locus is representative of the population being observed, and the nature of the Galactic dust extinction, as discussed in §3.2.

SLR is flexible. The simple matching of the observed instrumental stellar locus to a standard one allows for a diversity of input catalogs. The input can be purely flat-fielded, instrumental photometry, and SLR will correct them for atmospheric and Galactic extinction, and zeropoints. SLR will equally allow input photometry that has already been corrected for some or all of these effects, as previous authors have shown. We have applied SLR to pre-calibrated SDSS photometry (§3.4.2) and to instrumental photometry from two different instruments (§3.4.3, §3.4.4). The method makes no distinction between the various sources of locus shifts in color-color space, so it can be applied to photometric catalogs generated up to any stage in the traditional analysis chain. One can even envision mixing catalogs by, for example, acquiring *griz* imagery of a field and performing SLR, then acquiring further z-band images of the same field and coupling the new instrumental z-band catalogs to the already-calibrated *gri* ones. The resulting $\boldsymbol{\kappa}$ will produce the new z-band calibration, and should reproduce the *gri* calibrations. SLR can be optimized to give fast calibrations for a wide variety of optimized observing strategies. Of course, SLR will perform best when the prior reduction steps do not induce additional color scatter nor scalings, rotations, and shears.

SLR is fast: mountaintop reductions can provide accurate colors, and hence photometric redshifts, on-the-fly. Optimizing the use of allocated telescope time is an important goal. By performing real-time SLR reductions of photometric data, observers can determine when a desired signal to noise ratio is attained. A specific application of SLR by our group is the real-time determination of photometric redshifts of large numbers of galaxy clusters—an application we illustrated in §3.4.4. In upcoming runs we intend to use SLR to make adaptive adjustments of integration times while observing clusters of known position but unknown redshift.

3.5.3 Limitations

As a different way of calibrating photometry, SLR also carries some unique limitations. The main limitation is that SLR performs better in obtaining highly accurate colors than magnitudes in each of the bands. By the same token, the colors that are produced by the SLR approach are only as good as the standard stellar locus used as the calibration standard. Of particular concern is the need of identify a set of calibration stars that have suffered minimal Galactic extinction, and whose median metallicity reflects that of the stellar populations we observe in practice.

Another principal limitation is that SLR calibrations necessarily correct for Galactic extinction. To SLR, the dust correction is as natural as the atmospheric extinction correction. This is because our locus is standardized to stars suffering minimal extinction, while stars we observe in practice will almost always be behind the dust. It is, however, more common to calibrate photometry to the top of the atmosphere and only optionally apply an SFD Galactic extinction correction by hand, if needed. There is considerable uncertainty in our understanding of the dust, and this must be folded into our *a priori* color error estimates. In nearly all the fields we have studied, results suggest that SLR corrects extinction through a wide range of dust thicknesses with high accuracy. Users should take special care not to double-correct the extinction when using SLR.

Consequently, SLR will produce discrepant results if the sources of extinction vary significantly across the field of view. This introduces a trade-off between larger field size, which allows more stars to be included in the regression, and spatially constant extinction, which SLR corrects for best. We have applied SLR on small fields of view with as few as 7 useful stars, and the uncertainties in these cases are predominantly statistical. If SLR is to be applied to larger fields, one possible way to minimize extra scatter from Galactic extinction is to first apply the SFD dust correction for each stellar position, and then allow SLR to make the residual color calibration. For widely varying dust across a field, this should suppress the large scale gradients and thus unnecessary scatter in the stellar locus.

A third source of concern, both for traditional methods and SLR, are systematic differences between point source and galaxy photometry. Ivezić et al. (2007) and our own results demonstrate that applying a color correction derived from stars to galaxies does produce reliable photometric redshift estimates for red sequence galaxies. Some level of systematic error is nonetheless expected, because the spectral energy distributions (SEDs) of Galactic stars differ from the underlying SEDs of possibly redshifted galaxies of all types. Moreover, heavily extincted sources with different intrinsic SEDs will not suffer identical color shifts (McCall, 2004). These are fundamental limitations of broadband photometry: as integrals over the product of a source's SED, atmospheric and Galactic dust transmission functions, and the instrumental sensitivity curve, broadband measurements entangle the true SEDs with intervening attenuation effects almost irreversibly (Stubbs & Tonry, 2006). This systematic error afflicts *all* photometry that uses stellar calibration standards, and is not unique to SLR.

We finally note that, in the optical, SLR implicitly requires the g-band. This is because the critical optical feature that makes our realization of SLR possible is the kink in the stellar locus at $r - i \sim 0.7$—the stellar locus in the $(r - i, i - z)$ plane is virtually featureless. The kink (1) gives the one-dimensional locus line a distinctive shape that uniquely locates it in color-color space, and (2) provides a component of the locus that is nearly perpendicular to the reddening from Galactic and atmospheric extinction (see also Straizys et al., 1998). A purely linear stellar locus line does not allow for a *unique* stellar locus regression solution, as an instrumental locus could slide freely along that line. Inspection of Figure 3.1 reveals the importance of having g-band data.

3.5.4 Future Directions

Standard locus refinements. We consider the standard stellar locus used for this paper to be a starting point. SLR's performance rests on the standard locus being representative of the population that any given observation probes. It may be advantageous to develop different standard loci for different expected populations—for example, one for low Galactic latitudes, or different standard loci for different exposure times. The various standard loci could be measured empirically, or the expected perturbing effects could be modeled analytically and applied to the Covey et al. (2007) locus.

A fuller treatment of Galactic extinction. As pointed out by McCall (2004), extinction by Galactic dust produces a shift in color that depends on the underlying photon spectral energy distribution of the source. For the current implementation of SLR we have ignored this effect, which will produce shears, scalings, and rotations as well as a simple translation in color-color space. These are analogous to color-airmass effects. We also expect that, if large fields must be calibrated in one SLR pass, it may be advantageous to apply the SFD correction for each stellar position first, as mentioned in §3.5.3. This may reduce scatter in stellar loci constructed from large data sets with widely varying extinctions.

SLR vs. Galactic extinction and metallicity. This paper has shown that SLR accounts for the Galactic extinction in nearly all fields we have studied so far. The notable exceptions are the Stripe 82 results in §3.4.2, which corroborate those of Ivezić et al. (2007). Interestingly, the Galactic latitudes of the Stripe 82 fields where stellar locus methods fail are roughly equal to and *higher than* many of the fields we have used to recover the SFD extinction (§3.4.1) and measure cluster redshifts (§3.4.4). This presents difficulty in placing a hard lower bound on $|b|$ where SLR should be valid. While we expect SLR to perform more reliably toward higher Galactic latitudes, we suspect SLR, by its nature, has the potential to make *better* Galactic extinction corrections than SFD. This warrants extended and in-depth studies comparing SLR color shifts jointly to SFD prediction and metallicity.

Other passband combinations. We have concentrated heavily on the $grizJ$ bands, but the basic approach should be applicable to other photometric systems, such as u, HK, and $UBVRI$. MacDonald et al. (2004) have shown that the stellar locus as probed by the Johnson bands has a kink feature that makes this possible. We will also be interested to see how the PanSTARRS y band at $1\,\mu$m will add to the accuracy of SLR. Another interesting path to pursue is the use of the SLR approach to transform data between photometric systems.

Multi-frame SLR. If we ignore color-airmass terms, then image stacks from individual frames taken at different airmasses should also be amenable to SLR analysis. A better approach, however, might be to extract SLR colors from all possible independent permutations of the multiband images, and then average the resulting colors. This is similar to the philosophy applied in the "$N(N-1)$" approach to frame subtraction photometry for supernova cosmology (Barris et al., 2005), wherein all possible pairs of images are subtracted. This seems especially worth pursuing for multi-epoch surveys like PanSTARRS and LSST, as it completely sidesteps the challenges of combining frames with different PSFs obtained at different airmasses.

Color recalibration of SDSS and 2MASS? If the stellar locus does in fact provide us with a uniform calibration source over most of the sky, and if SLR provides special insensitivities to anomalous atmospheric and Galactic extinction effects, then it is enticing to consider a joint recalibration of *colors only* from both the SDSS and 2MASS surveys. A Bayesian approach using the uniformity of the stellar locus, as was done in optical bands by Ivezić et al. (2007), might improve the accuracy of both optical and IR colors in these catalogs.

3.6 Conclusions

We have developed and demonstrated a technique that exploits the universality of the stellar locus to immediately obtain accurate colors from uncalibrated multiband data. For those who might wish to exploit the SLR approach, the core IDL tools we have developed are available at `http://stellar-locus-regression.googlecode.com`.

Using archived photometry from the SDSS survey, we have demonstrated that SLR can produce results that agree with the commonly used SFD extinction map over a wide range of dust thicknesses. The performance of SLR in these cases appears to be limited by systematic zeropoint drifts in SDSS magnitudes. We also reproduced the anomalous stellar locus reddening results of Ivezić et al. (2007) in a few SDSS Stripe 82 fields. This puts into question (1) the validity of the $R_V = 3.1$ reddening law in those fields, (2) whether the dust is *both* in front of and behind the stars, and (3) whether these fields have stars with spatially correlated deviations from expected median metallicity.

Images of fields obtained through a wide range of airmasses were subjected to SLR analysis. We recovered the colors of the stars in these images with an uncertainty limited by the Poisson and flat-field errors in the photometry from each frame. Using SLR-only techniques and 2MASS calibrated photometry, we additionally obtained i-band zeropoints in the fields good within 18 mmag.

Finally, we have also presented photometric redshift results using SLR-derived colors only. We recovered the spectroscopic redshifts of 11 galaxy clusters at redshifts $0.09 < z < 0.25$ with $\sigma_z/(1+z) = 0.6\%$ RMS residual error. The redshift residuals also showed that the red sequence galaxy colors from SLR alone were consistent with an intrinsic Galactic extinction correction.

The SLR technique, as implemented in our IDL code, can be used at the telescope in real-time to optimize the use of allocated telescope time. We regard SLR as a promising way to calibrate colors and magnitudes using fundamentally different physical assumptions, providing calibrations far faster than the traditional approach.

3.7 Acknowledgments

The approach outlined here builds upon the impressive work carried out in building and analyzing the SDSS and 2MASS data archives. We are grateful to the builders and operators of the SDSS and 2MASS systems. We also acknowledge our deep reliance on the groundwork laid by the authors of the Covey et al. (2007), Ivezić et al. (2008), Sesar et al. (2007), and Ivezić et al. (2007) papers. We are also grateful to the developers (Marigo et al., 2008) of the on-line stellar evolution modeling tool at `http://stev.oapd.inaf.it/cgi-bin/cmd_2.1`. We are pleased to thank D. Finkbeiner, Z. Ivezic, T. Axelrod, A. Saha, D. Burke, J. Mohr, C. Smith, W. M. Wood-Vasey, A. Loehr, T. Stark, N. Suntzeff, J. Tonry, and J. Battat for valuable conversations.

This research has made use of the NASA/IPAC Extragalactic Database (NED) which is operated by the Jet Propulsion Laboratory, California Institute of Technology, under contract with the National Aeronautics and Space Administration. This publication has made use of data products from the Two Micron All Sky Survey, which is a joint project of the University of Massachusetts and the Infrared Processing and Analysis Center/California Institute of Technology, funded by the National Aeronautics and Space Administration and the National Science Foundation. This research has made use of the NASA/ IPAC Infrared Science Archive, which is operated by the Jet Propulsion Laboratory, California Institute of Technology, under contract with the National Aeronautics and Space Administration.

Funding for the creation and distribution of the SDSS Archive has been provided by the Alfred P. Sloan Foundation, the Participating Institutions, the National Aeronautics and Space Administration, the National Science Foundation, the U.S. Department of Energy, the Japanese Monbukagakusho, and the Max Planck Society. The SDSS Web site is http://www.sdss.org/. The SDSS is managed by the Astrophysical Research Consortium (ARC) for the Participating Institutions. The Participating Institutions are The University of Chicago, Fermilab, the Institute for Advanced Study, the Japan Participation Group, The Johns Hopkins University, Los Alamos National Laboratory, the Max-Planck-Institute for Astronomy (MPIA), the Max-Planck-Institute for Astrophysics (MPA), New Mexico State University, Princeton University, the United States Naval Observatory, and the University of Washington.

This work is supported by the NSF (AST-0607485, AST-0506752), the DOE (DE-FG02-08ER41569), NIST (70NANB8H8007), and Harvard University. We also thank the team of scientists, engineers and observing staff of the Las Campanas Observatory.

3.8 Motivating the Color Transformation Equation

Note that this section appeared originally as an appendix in High et al. (2009).

Equation (3.1) represents photometric calibrations using a compact, filter-independent matrix notation because in the future we wish our procedure to be applicable to any set of filters. In this section we give a concrete example for the $grizJ$ filters in order to motivate and convey the meaning of the notation.

3.8.1 Usual Photometric Calibration Equations

Photometric calibrations are normally modeled with simple additive and sometimes multiplicative terms. Following the southern SDSS standards literature (Smith et al., 2002, 2003; Clem et al., 2007)[11] as rough guides, we relate the instrumental magnitude (g, r, i, z) through the SDSS passbands to the true, extra-Galactic magnitude (g_0, r_0, i_0, z_0) as

$$g = g_0 + a_g + E_g + A_g + b_g(g_0 - r_0) + c_g X_g(g_0 - r_0) \tag{3.8a}$$

$$r = r_0 + a_r + E_r + A_r + b_r(r_0 - i_0) + c_r X_r(r_0 - i_0) \tag{3.8b}$$

$$i = i_0 + a_i + E_i + A_i + b_i(i_0 - z_0) + c_i X_i(i_0 - z_0) \tag{3.8c}$$

$$z = z_0 + a_z + E_z + A_z + b_z(i_0 - z_0) + c_z X_z(i_0 - z_0) \tag{3.8d}$$

$$J = J_0, \tag{3.8e}$$

---

[11] For other relevant unpublished documents see http://www-star.fnal.gov/Southern_ugriz/publications.html

where in the last equality we take the 2MASS data to be calibrated already. Here, a_n is the zeropoint for the passband n; E_n is the atmospheric extinction, often modeled as $k_n X_n$ for some filter-dependent coefficient k_n and airmass X_n through which exposure R is taken; and A_n is the estimated Galactic extinction. b_n is the color coefficient, and c_n is the color-airmass cross term coefficient. The free parameters k_n, a_n, b_n and c_n can be estimated from the literature or measured using intermittent standard star observations, interpolating in airmass and in time to the science exposures. Galactic extinction is estimated using SFD.

3.8.2 Corresponding Color Equations

Colors are magnitude differences. Subtracting magnitudes between adjacent passbands using Equations (3.8) gives

$$(g-r) = (g_0 - r_0) + (a_g - a_r) + (E_g - E_r) + (A_g - A_r) + \tag{3.9a}$$

$$b_g(g_0 - r_0) - b_r(r_0 - i_0) + c_g X_g (g_0 - r_0) - c_r X_r (r_0 - i_0) \tag{3.9b}$$

$$(r-i) = (r_0 - i_0) + (a_r - a_i) + (E_r - E_i) + (A_r - A_i) + \tag{3.9c}$$

$$b_r(r_0 - i_0) - b_i(i_0 - z_0) + c_r X_r (r_0 - i_0) - c_i X_i (i_0 - z_0) \tag{3.9d}$$

$$(i-z) = (i_0 - z_0) + (a_i - a_z) + (E_i - E_z) + (A_i - A_z) + \tag{3.9e}$$

$$b_i(i_0 - z_0) - b_z(i_0 - z_0) + c_i X_i (i_0 - z_0) - c_z X_z (i_0 - z_0) \tag{3.9f}$$

$$(z-J) = (z_0 - J_0) + a_z + E_z + A_z + \tag{3.9g}$$

$$b_z(i_0 - z_0) + c_z X_z (i_0 - z_0). \tag{3.9h}$$

This is greatly simplified with matrix notation. We define the instrumental color vector as

$$\boldsymbol{c} \equiv \begin{pmatrix} g - r \\ r - i \\ i - z \\ z - J \end{pmatrix}, \tag{3.10}$$

and likewise for the true color vector $\boldsymbol{c}_0$; the additive color calibration vector as

$$\boldsymbol{\kappa} \equiv \begin{pmatrix} a_g - a_r + E_g - E_r + A_g - A_r \\ a_r - a_i + E_r - E_i + A_r - A_i \\ a_i - a_z + E_i - E_z + A_i - A_z \\ a_z + E_z + A_z \end{pmatrix}; \tag{3.11}$$

the color term matrix as

$$\mathbf{B} \equiv \begin{pmatrix} b_g & -b_r & 0 & 0 \\ 0 & b_r & -b_i & 0 \\ 0 & 0 & b_i - b_z & 0 \\ 0 & 0 & b_z & 0 \end{pmatrix}; \tag{3.12}$$

and the color-airmass term matrix as

$$\mathbf{T} \equiv \begin{pmatrix} c_g X_g & -c_r X_r & 0 & 0 \\ 0 & c_r X_r & -c_i X_i & 0 \\ 0 & 0 & c_i X_i - c_z X_z & 0 \\ 0 & 0 & c_z X_z & 0 \end{pmatrix}; \tag{3.13}$$

then we can write the color calibration equations as a single matrix equation,

$$\boldsymbol{c} = \boldsymbol{\kappa} + (\mathbf{1} + \mathbf{B} + \mathbf{T})\, \boldsymbol{c}_0, \tag{3.14}$$

where $\mathbf{1}$ is the identity matrix. Setting $\mathbf{T} = \mathbf{0}$, this is equal to Equation (3.1). The inverse color transformation is

$$\boldsymbol{c}_0 = (\mathbf{1} + \mathbf{B} + \mathbf{T})^{-1} (\boldsymbol{c} - \boldsymbol{\kappa}) . \tag{3.15}$$

Whether the transformation matrices are invertible depends on the details of how first order color coefficients are chosen, but under normal circumstances it will be possible. Using the example we've just presented, $(\mathbf{1} + \mathbf{B})$ is invertible because its determinant is $(1 + b_g + b_r + b_g b_r)(1 + b_i - b_z)$, which is not equal to zero for typical (small) values of color terms.

This is how our matrix notation corresponds to typical photometric calibrations. The notation is trivially generalized to any filter set. The notation also motivates generalizations in choice of calibration parameters. For example, the color term matrix $\mathbf{B}$ can be made to be diagonal, (anti-)symmetric, or populated entirely by different nonzero entries, depending only the particular application. Furthermore, higher order terms can be considered by including higher powers of $\boldsymbol{c}_0$ to Equation (3.14).

Chapter 4

Sky Variability in the y Band

4.1 Introduction

The Large Synoptic Survey Telescope (LSST) is a proposed wide-field camera that is currently in the design and development phase (LSST Science Collaborations: Abell et al., 2009, hereafter LSST09). The project has designated the telescope's site to be Cerro Pachon, Chile, on the same ridge that hosts the Gemini South and SOAR telescopes. The LSST will survey the sky in the Sloan Digital Sky Survey's *ugriz* passbands, plus an additional near infrared band, y, at wavelengths ~ 990 nm, only recently made possible by deep depletion CCD technology that enhances quantum efficiency (QE) at the reddest wavelengths (O'Connor et al., 2006). The Pan-STARRS (Kaiser et al., 2002) survey also uses the y band.

The designation of "y" may present confusion. Infrared astronomers use a band Y, typically with a central wavelength near 1.03μm (Hillenbrand et al., 2002; Hewett et al., 2006). Their use of infrared detectors, with a flatter response curve near a micron, yields a passband with significantly different shape than the CCD-based y. Our filter also bears no relation to the optical y filter of the Stromgren passbands, which is centered on 550 nm. This degeneracy in terminology is most unfortunate, but seems likely to persist.

The sky brightness in the y band has not been well characterized for astronomical CCD applications. Past work describing sky brightness at observatories typically cite values for the $UBVRI$ bands, but not y (Patat, 2003; Kriscuinas et al., 2007; Sanchez, 2007). The reddest band in the SDSS survey is z, whose red edge is determined by the rapidly falling QE of the SDSS detectors, which have very little sensitivity in the y band region. The UKIRT survey presented sky measurements for the Y band (Warren et al., 2007), but as explained before, the total transmission curve is significantly different than that using a deep depletion CCD.

Our aim has been to provide the first dedicated CCD measurements, at the proposed LSST site, of the y band sky background and its variability over the course of a night. While the exact character of the new y band to be used for LSST is under active consideration, we used a filter candidate called y_3 (LSST09). We expect our qualitative findings to hold for any y band variant under active consideration because the sky background in all cases arises overwhelmingly from narrow OH emission lines. Figure 4.1 shows potential y band transmission curves with detector quantum efficiency (QE) and atmospheric response for both LSST and our apparatus, along with the anticipated sky emission spectrum.

In §4.2 we briefly describe the known nature of sky emission within the y passband, covering past aeronomic (§4.2.1) and astronomical (§4.2.2) measurements. In §4.3 we

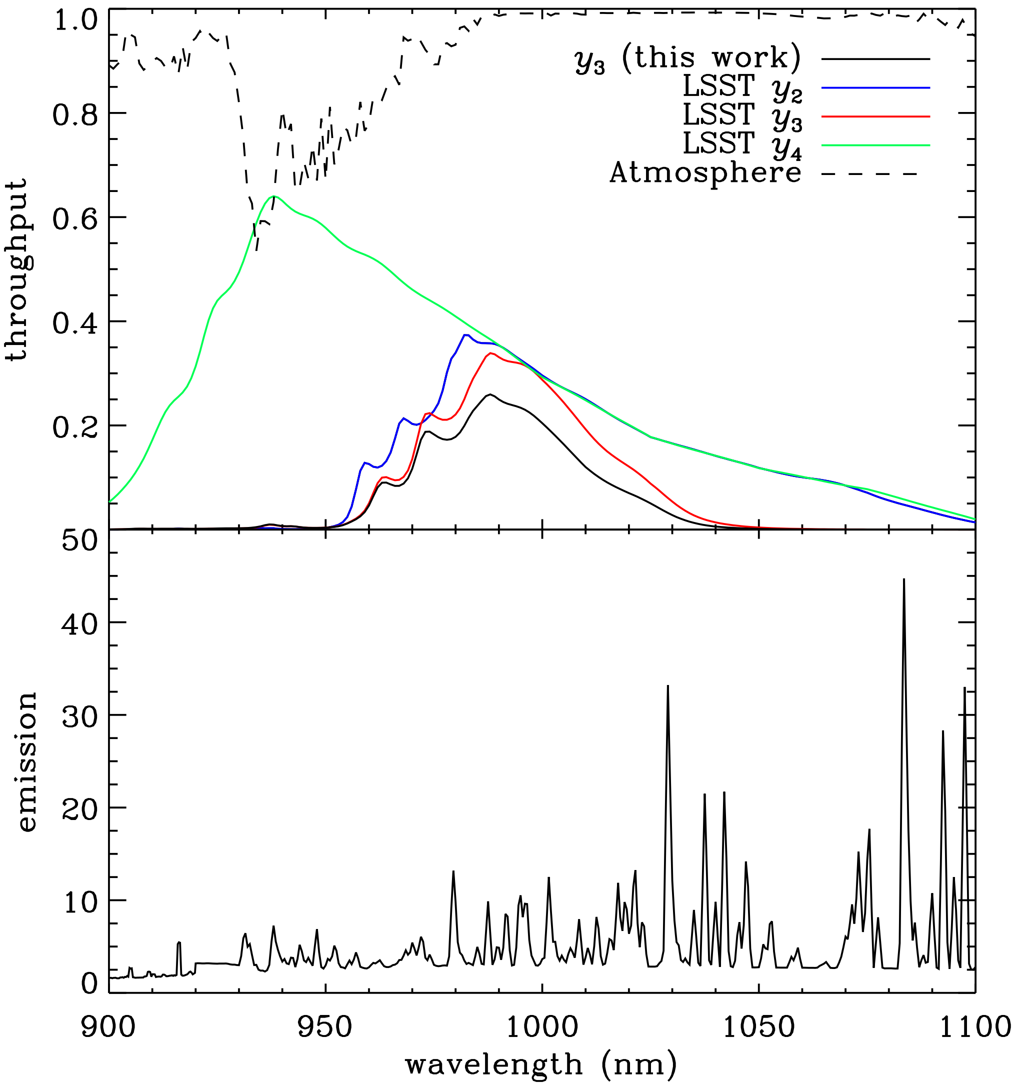

Figure 4.1: The LSST y band and its variants (top), and the sky emission spectrum (bottom). The top panel shows the expected transmission spectrum for proposed y band variants (LSST Science Collaborations: Abell et al., 2009) including predicted optics and detector response, as well as the relative transmission that we measure for our apparatus (black solid line). Our effective filter curve closely resembles the planned y_3 band. All spectra exclude atmospheric absorption and scattering, which we plot separately as a dashed line. The bottom panel shows a typical sky spectrum in photons sec^{-1} m^{-2} nm^{-1} arcsec^{-2}, dominated by Meinel band OH emission lines (taken from Puxley & the Gemini Observatory, 2001).

describe the dedicated instrument we assembled for these measurements. Section 4.4 discusses the observations, and the data reduction is outlined in §4.5. Section 4.6 presents results on spatial (§4.6.1) and temporal (§4.6.2) variability, and an absolute calibration (§4.6.3), and we conclude with §4.7.

4.2 The Nature of y Band Sky Background

The background sky in the y passband is dominated by Meinel band emission due to hydroxyl (Meinel, 1950a,b), in a physical process that has long been observed (eg Wiens et al., 1997; Nakamura et al., 1999) and modeled (Rousselot et al., 2000; Cosby et al., 2006; Cosby & Slanger, 2007) by atmospheric scientists (for a useful overview, see Marsh et al., 2006). Hydroxyl is well stratified in the mesopause at 90 km in a 10 km thick layer (Baker & Stair, 1988; Melo et al., 2000). Above the ozone layer in the stratosphere, daytime UV light from the sun dissociates O_2 to make $O + O$, which react with other O_2 to produce O_3. UV light also dissociates O_3, completing the oxygen-ozone cycle. O_3 additionally reacts with H to produce O_2 and excited OH, which then emits photons to produce the airglow within the y band.

As distinct from Rayleigh scattering, Meinel emission is known to vary significantly over a number of spatial and temporal scales (eg Marsh et al., 2006). The airglow varies with the tides, and is linked to the seasons and the solar cycle. Traveling and standing atmospheric gravity waves, which are coherent density perturbations analogous to ocean waves, are regularly observed by aeronomers (eg Taylor & Hill, 1991; Garcia et al., 1997; Nakamura et al., 1999; Li et al., 2005), and give rise to a variable background over a single, wide-field y band CCD image.

4.2.1 Aeronomic Measurements

Aeronomers, like astronomers, have made extensive use of CCDs since their invention, but also have not explored the y passband region with them in depth because the development of deep depletion is recent. CCDs have been used to measure sky emission lines in isolation with Fabry-Perot interferometers, for the purpose of monitoring atmospheric gravity waves and variability in species temperature and emission rate (eg, the Spectral Airglow Temperature Imager, SATI, Wiens et al., 1997). They have also been used to image gravity waves directly with narrow and broad filters (eg Taylor & Hill, 1991; Garcia et al., 1997; Li et al., 2005). These applications have been most often used in concert with radar, lidar, balloons, rocketry, and space-based experiments to achieve fully three-dimensional dynamical information of O_2 and OH atmospheric layers. None of these observations ventured far into the red of today's deep depletion CCDs, nor did the analyses achieve calibrated photometry. Existing aeronomic data are therefore of limited use to LSST, as LSST requires prior knowledge not only of the variability but also of the expected absolute background level in the y channel. Our instrument and data reduction techniques aim to provide all needed information at once.

4.2.2 Previous Astronomical Measurements

Previous astronomical work is also insufficient, as the y band sky has not been directly characterized. Extrapolating to the y band using other astronomical filters is problematic because of the highly structured nature of the Meinel band emission (Figure 4.1, bottom panel). Small changes in the filter's red edge may suddenly alter the background level. For example, the recent UKIRT survey (Warren et al., 2007) does include a Y band, but using an infrared detector and filter whose total response function do not match that expected for LSST. Warren et al. (2007) in fact showed that their Z band sky brightness from the UKIRT observations on Mauna Kea was 0.4 mag arcsec^{-2} brighter than that obtained by SDSS in their z band, at Apache Point, New Mexico. Besides differences in effective filtering, the discrepancy may be explained by differences in atmospheric conditions in time and in space given the great geographical separation. We therefore must assume that the UKIRT median sky brightness of $Y = 17.4$ mag arcsec^{-2} (Vega) cannot be applied to LSST.

Our effective filter function closely matches LSST's y_3 band and thus minimizes potential errors due to differences in relative spectral response; we additionally address the geographical problem by observing at Cerro Tololo, a mountain ridge 10 km northwest of LSST's planned site, Cerro Pachon. Kriscuinas et al. (2007) presented a historical overview of sky brightness observations from Cerro Tololo, for the period 1992–2007. They claimed that there was no discernable difference in sky brightness between Cerro Tololo, where we obtained our data, and Cerro Pachon, the designated site for LSST. This leads us to conclude that our y band sky brightness measurements from Tololo should be applicable to the LSST site on Pachon.

We conclude that previous work within aeronomy and astronomy is not sufficient for characterizing the y band sky background for LSST, and that the precise nature of the chosen y filter affects the observed background due to the multitude of strong OH lines at ~ 1 μm and redder. The dependence of the apparent NIR sky brightness on the filter and detector combination, and the potential for variation between observatory sites, motivates the measurements described here.

4.3 Apparatus

We used a Pixis system (detector, readout electronics, dewar and shutter) from Princeton Instruments, equipped with a type 1024BR CCD. This detector, made by EEV with their designation 47-10, was a back-illuminated deep depletion sensor that exhibits enhanced sensitivity at wavelengths near 900 nm due to the thicker region of silicon from which photocharge is harvested. The sensor was an array of 1040×1027 pixels, each of which was 13.0 μm on a side. The Pixis camera was equipped with a thermoelectric cooler that maintained the detector at a temperature of -20 C. Dark current was negligible compared to the flux seen from the sky. We measured the camera's gain to be 3.8 e^{-} ADU^{-1}.

Princeton Instruments designed the 1024BR CCD to suppress fringing that would otherwise arise from night sky line emission. We observed no significant fixed fringing patterns in any of the images we obtained, and did not have to apply any fringe-frame corrections to the data. We therefore judge any systematics in the photometry due to fringing to be subdominant for the purposes of the results presented here.

The Pixis camera was controlled from a laptop computer that ran the Linux operating system. We used custom software to control the exposure times and imaging sequence of the instrument. All images were stored as 16 bit FITS files.

We attached a 17–55 mm variable focal length $f/2.8$ Canon EFS lens to the Pixis dewar, using a C-mount adapter made by Birger Engineering. The system was operated at $f/2.8$. The y filter we used was an interference filter manufactured to the

LSST y_2 specification by Barr Associates, in a 2 in × 2 in format. We attached the filter to the front of the lens using a modified professional photography filter holder that mated to the 75 mm front threads of the Canon lens. The lens's focal length was adjusted so as to provide a plate scale of 145 arcsec pixel^{-1}, and a square field of view of 41 deg. Although we make use of a y_2 filter, the resultant system throughput more closely matches the LSST y_3 response curve due to the difference in our detector QE and AR coatings on the optics from the predicted LSST system.

The camera, lens and filter combination was mounted on a stationary tripod. This arrangement did not provide pointing information in the image headers, but as described below we were later able to determine astrometry using the positions of cataloged sources.

Our optical configuration was not identical to that of LSST. The LSST filters will be placed in an $f/1.23$ converging beam. Light from a point source therefore passes through the LSST filter in a (hollow) cone with an opening half-angle between 14.2 deg and 23.6 deg. Obscuration from the secondary blocks rays at angles less than 14.2 deg. The transmission curve through the interference filter depends on the angle of incidence. Rays that traverse the filter at angles θ other than normal incidence produce a blue shifted transmission function, shifted to the blue by roughly

$$\delta\lambda = \lambda(\sqrt{1 - n^{-1}\sin^2(\theta)} - 1) \tag{4.1}$$

where n is the effective index of refraction of the filter dielectric. The effective LSST passband is the appropriately weighted integral of these angle-dependent transmission functions.

For our observations we placed the filter in front of the lens, so rays from any point source pass through the filter as parallel rays. The center of our field is observed through the filter at normal incidence. The edges of our field are observed through the filter at an incidence angle of 20 deg. While we can't replicate the *distribution* of rays that will pass through the LSST filters, by judiciously choosing the region in our field where we measure the sky brightness, we can try to match the median LSST ray that traverses the filter at an angle of 18.9 deg (LSST09). We therefore expect, even for a perfect match between our interference filter and that of LSST, slight differences in the effective passbands. See Figure 4.1 for a comparison of passbands.

4.4 Observations

We obtained images over four nights, UT 2007 Sep 13, 14, 18, and 19. On the 13th we acquired data on the second half of the night, and pointed the camera on the local meridian and low to the horizon at a zenith angle of about 60 deg. For the remaining nights we aimed the camera on the local meridian toward the equatorial, at approximately 30 deg north.

The moon was 6% illuminated on the first two nights and set at $01^{\mathrm{h}}43^{\mathrm{m}}$ UT. The moon was 44% illuminated on the last two nights and rose at $05^{\mathrm{h}}30^{\mathrm{m}}$ UT. For the all observations, the moon was not a complicating factor. We estimate that the conditions on the first two nights were photometric, whereas high clouds began to form on the second half of the 18th and all of the 19th. Table 4.1 summarizes the observations.

Table 4.1: Summary of the Data.

Night[a]	Num exposures		Conditions[b]
	5 min	20 sec	
2007 09 13	54	31	Photometric
2007 09 14	111	58	Photometric
2007 09 18	76	40	First half of night photometric
2007 09 19	67	35	Clouds

On each night we elected to take all images at a fixed azimuth and elevation in order to simplify our analysis of the temporal variation in sky brightness. The nominal pointing changed somewhat from night to night, however, because we disassembled the apparatus each morning. We did not track the camera in R.A. We alternated between sequences of five 20 sec ("short") exposures and ten 300 sec ("long") exposures throughout the night. On the 14th we acquired a total of 55 short exposures and 110 long exposures. The short frames had only slight trailing of stars, and were useful for astrometry and photometric normalization using the normal toolkit of astronomical

---

[a] Local date at start of night.

[b] Based on our observations, archived SASCA red-channel animations (see `http://www.ctio.noao.edu/$\sim$sasca/sasca.htm`), GOES East 10 micron satellite imagery (see `http://www.ctio.noao.edu/sitetests/GOES/`), CTIO DIMM and flux monitor data, and Blanco Cosmology Survey observers' logs.

data reduction for point sources. The longer images offered better signal to noise for the sky brightness, but stars trailed significantly in the EW direction.

4.5 Data Reduction

We used the utilities in IRAF to do a line-by-line bias subtraction of each of the images, using the overscan. The 300 sec exposures were combined into a normalized sky flat, by taking a flux-scaled median of the frames. This normalized sky flat was then used to flat-field each of the images. The normalized sky flat had a fractional response suppression of about 20% from the center to the corners of the field, presumably due to vignetting and perhaps plate scale variation from the lens. This variation in flux sets an upper bound for potential systematic errors in sky brightness due to passband dependence on the angle of incidence, at 0.2 mag. We take this as an extreme upper limit, since we do expect $\cos^n$ factors to roll off the response at the edges of the field. Because we are measuring sky brightness, the stacked sky flat is indeed appropriate for correcting the pixel-to-pixel variations on the scale of a PSF. Our 41 deg ×41 deg field of view rendered twilight flat-fielding impossible due to sky gradients over such a large field and to the short window of time over which useful sky levels per pixel could be acquired, and we had no system in place for obtaining the equivalent of dome-flats. As noted in §4.3, the 1024BR CCD was specifically designed to suppress fringing, and indeed we observed no fringe patterns in any of our data and therefore made no fringe-frame corrections. Figures 4.2 and 4.3 show typical long exposures, after flat-fielding and bias subtraction.

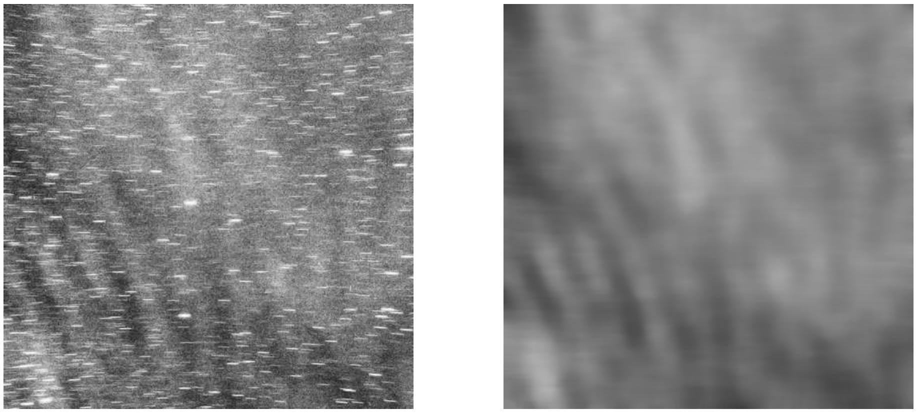

Figure 4.2: A flat-fielded 300 sec exposure in y_3, taken at fixed altitude and azimuth (righthand frame has stars removed to emphasize the airglow structure). The star trails subtend about 1.25 deg in the EW direction; north is up and east is right. This image shows two distinct gravity waves traced by NIR narrowband emission, which gives rise to short term variability in y_3 band sky brightness. The high frequency ripples have wavelength of about 5 deg and propagate at between zero and about a degree per minute. The low frequency ripple's wavelength is roughly the field of view (40 deg) and travels at a degree per minute. Root mean square sky variations in a given frame are up to 4%, while the overall sky level over a full night varies by a factor of 2.

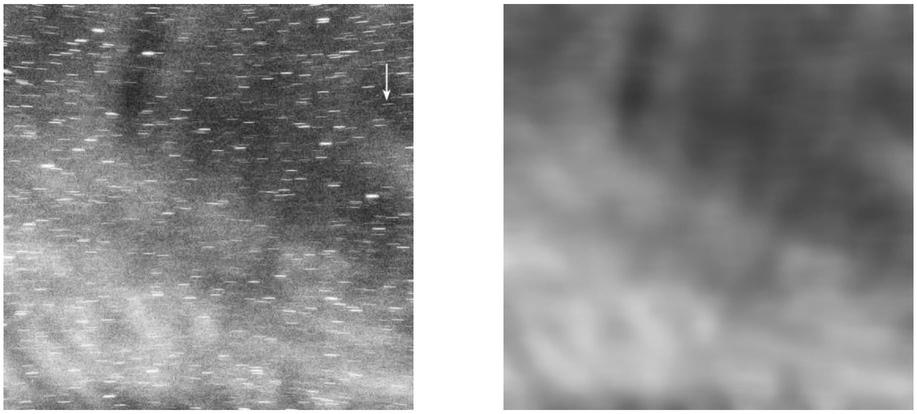

Figure 4.3: Same as Figure 4.2, but taken later in the night, just as our calibration star ρ Ceti entered the field of view (upper right corner of lefthand frame).

4.6 Results

We first explored relative measurements of the sky background, because we expect relative errors to be significantly smaller than the overall uncertainty from absolute zeropoint calibration. We then estimated the overall zeropoint in the Vega and AB magnitude systems.

4.6.1 Spatial Variability

The gravity waves we observed in the vast majority of our images are easily seen in Figure 4.2 and 4.3. These structures were not due to flatfielding errors. This can be deduced from the two example images themselves, which were taken from the same night and had the same flatfield correction applied to them. Roughly speaking, the locations of large-scale brightness minima in Figure 4.2 correspond to maxima in Figure 4.3. Indeed, these waves appear and disappear, and move coherently in images from any given night viewed consecutively. Their direction of propagation is perpendicular to their wavefronts.

To quantitatively estimate the effect of the waves on sky brightness at any given time, we computed the mode of the sky brightness values for three regions of the detector, for each of the flatfielded 300 s images. The reference region was the central 500×500 pixel area of the detector. This was used to estimate the zero-level over the large area of sky that we observed. Our "calibrator" region was a smaller, circular aperture of radius 50 pixels near the detector corner that we ultimately used for zeropoint calibration (§ 4.6.3). The "control" region was another 50 pixel radius aperture near the opposite corner, but at the same angle of incidence with respect to the camera boresight. The calibrator and control regions were chose to be smaller than the size of the smallest coherent spatial gravity waves in the images, whereas the reference region was chosen to be much larger.

We calculated the mode of pixel values in each aperture to attain sky counts c in ADU pixel^{-1}. Relative magnitudes between each corner region and the central reference region were calculated as $\Delta\Sigma = 2.5 \log(c_{\mathrm{cal}}/c_{\mathrm{ref}})$, (likewise for $c_{\mathrm{ctrl}}/c_{\mathrm{ref}}$) with units of mag arcsec^{-2}, assuming a common pixel scale between the two apertures. Figure 4.4 shows these fractional differences over each night.

Observations on the night of the 13th were taken at $\sec(z) = 2$ airmasses at the center of the detector, with the calibrator region at 1.4 airmasses and the control region at approximately 4 airmasses, due to our large field of view. This gave rise

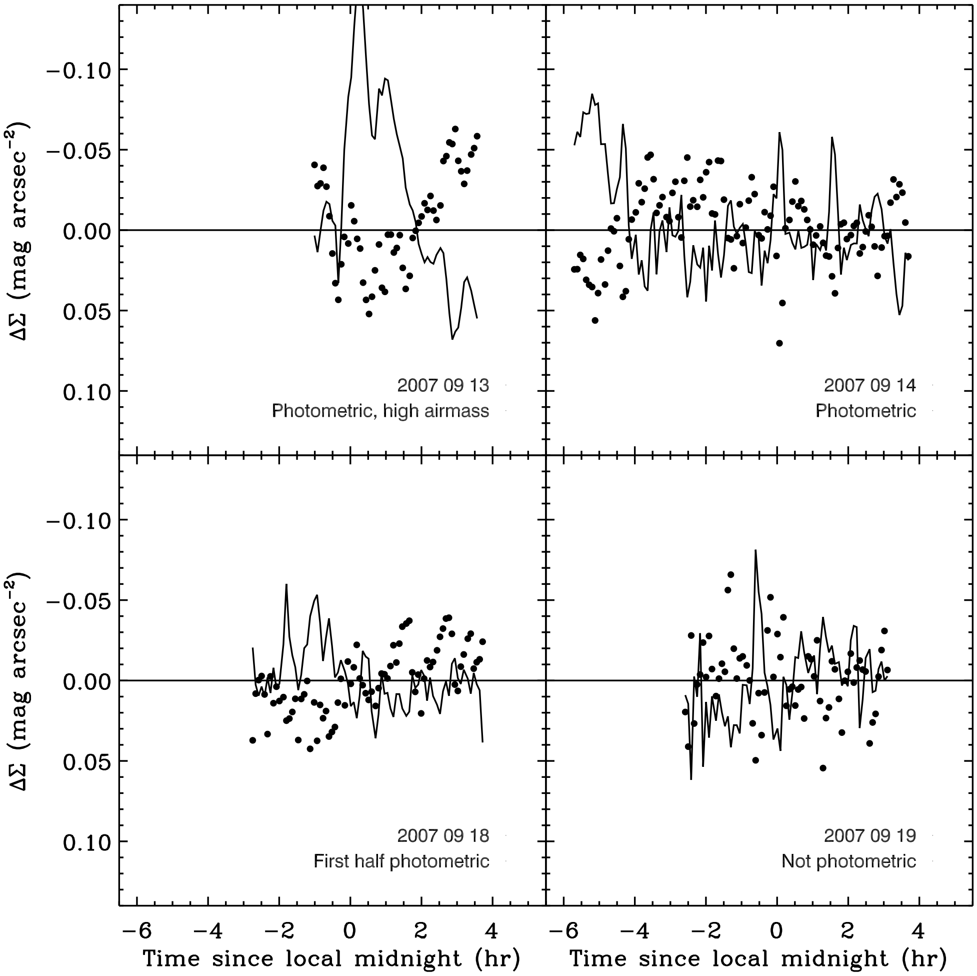

Figure 4.4: Spatial variation in y_3 band sky brightness versus time, showing 2–5% root mean square variability in flux. This plot shows the fractional difference in sky brightness between our calibrator region (circular aperture of radius 50 pixels) versus a central reference region of size 500 × 500 pixels (points), and between a second 50 pixel radius region on the opposite corner of the chip and the reference region (line). The large variation on the 13th is due to the extreme difference in airmass between to two corner regions: 5.8 for the northeast corner and 1.3 for the southwest corner. Early on in the night on the 14th, the Galactic plane fell within the NW aperture, again causing larger than typical variation.

to root mean square spatial sky brightness variations of 3% between the calibrator and the reference region, 6% between the control and the reference region, and 8% between the calibrator and control regions. On the other three nights, the camera pointed at about 1.2 air masses, with the calibrator region at 1.0 air masses and the control region at 1.4 air masses. Ignoring the early part of the 14th, where the Galactic plane fell within the control region, these nights exhibited 2–3% rms spatial variability with respect to the reference, and 3–4% rms variability between the calibrator and control regions. We conclude that, on angular scales of the wavelength of the gravity waves, $\gtrsim$ 2%, the spatial variability in the y band is typically 3–4% rms. Our relative photometric errors are expected to be subdominant to this effect. Under the assumptions that gain, exposure time, and pixel scale are all constant in any given image, these results are independent of those quantities and of any absolute flux calibration.

4.6.2 Temporal Variability

The overall temporal sky variability is estimated using a similar approach as in the previous section. The fluxes within the 500×500 pixel reference region are compared to the mean over all 4 nights, and plotted in Figure 4.5. Here we are comparing 2.5 times the log of sky counts in ADU pixel^{-1} *between* images rather than within them, but because all exposure times, gain values, and pixel regions (and therefore pixel scales) were the same, this is equivalent to measuring relative sky brightness in mag arcsec^{-2}. Again, all that needs to be done to bring this to an absolute scale is to add a zeropoint in mag arcsec^{-2}.

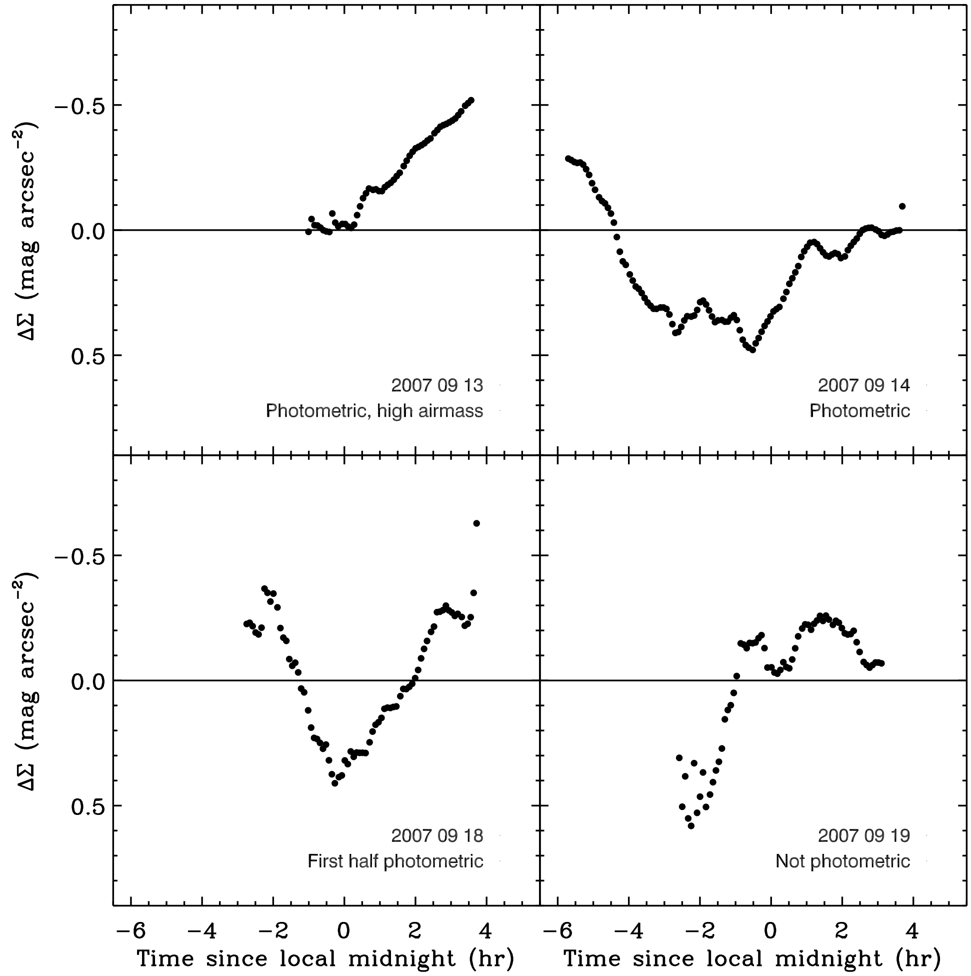

Figure 4.5: Temporal variation in y_3 band sky brightness versus time, showing highly coherent variability of up to a factor of 2 in flux over the course of a night. Flux was taken along a fixed line of sight that is 20 deg from the zenith and directed north. Data from the 13 and 14 are most probably photometric, the first half of the 18 may be useful, and the 19 is not photometric. The sky brightness levels in this plot were obtained from the same 2.13 deg radius circular region on the detector, and constitutes a differential measurement with very high signal to noise ratio. The fluctuations on both long and short timescales are real. We consider the Vega-based y_3 band zeropoint to be reliable to 0.2 mag, but this systematic uncertainty is swamped by the temporal variability in sky brightness. To convert to AB mag arcsec^{-2}, add 0.5 mag to the y_2^{Vega} values.

Immediately evident both in the Figure and in the raw images viewed in succession is a significant overall sky level variability. The peak-to-peak variation on the 13th is 1.8 in flux, and on the 14th, 18th, and 19th are 2.0, 2.7, and 2.2 in flux, respectively. We have used a huge region of about 400 deg^2, and we expect our statistical uncertainties from both the gravity waves and from electron counting to be subdominant to the temporal variability we measure. Changes in overall sky level are highly correlated in time, and all of the structure seen in Figure 4.5 is due to the atmospheric emission variablity.

The relative results have made use of only ADU counts, assuming constancy for all other quantities that are needed for an absolute flux calibration. Our final task is to estimate the overall zeropoint.

4.6.3 Absolute Sky Brightness

In order to convert measurements from ADU sec^{-1} pixel^{-1} to mag arcsec^{-2} we determined the gain, pixel scale, and magnitude zeropoint. We measured the gain to be 3.8 e^- ADU^{-1}. The pixel scale and zeropoint measurements were both accomplished using a standard star.

We used photometry of a type A0V standard star to establish a conversion between our instrumental magnitudes and a Vega-based y_3 band magnitude scale. This follows the approach used in Hillenbrand et al. (2002) and Hewett et al. (2006), where A0V stars are used as proxies for Vega to establish a zeropoint on the Vega magnitude scale.

We were fortunate to have beta-test access to the astrometry.net web utility (`http://astrometry.net/`), which has the remarkable ability to determine a WCS solution for an arbitrary image. We input one of our images, frame 110 (taken at UT $06^{\mathrm{h}}19^{\mathrm{m}}22^{\mathrm{s}}$) to this site and learned that the image was centered at R.A. = $01^{\mathrm{h}}17^{\mathrm{m}}34.8^{\mathrm{s}}$, Decl. = $-02^{\circ}20'49''$ (J2000). We then queried the SIMBAD archive to find A0 stars that coincided with this field. The A0V star ρ Ceti at R.A. = $02^{\mathrm{h}}25^{\mathrm{m}}57.0^{\mathrm{s}}$, Decl. = $-12^{\circ}17'26''$ (J2000) (also designated as HR 708 and SAO 148385) met our criteria. This object has cataloged magnitudes that are listed in Table 4.2.

Table 4.2: ρ Ceti data from the literature.

Band [a]	m^{Vega}	σ_m
U	4.85	0.03
B	4.85	0.03
V	4.88	0.03
J	5.08	0.20
H	4.86	0.02
K	4.81	0.02

We identified ρ Ceti in five of the short exposure images, and used IRAF to

---

[a] UBV data are from Mermilliod (1987) and JHK data are from Skrutskie et al. (2006).

perform aperture photometry. The resulting centroid positions, object fluxes, and sky background values are given in Table 4.3. We determined the flux from the star by averaging these measurements, obtaining 119 ± 17 ADU accumulated in 20 sec, or 5.95 ± 0.85 ADU sec^{-1} for an object with a Vega-based magnitude of $y^{\mathrm{Vega}} = 4.86$ mag. This fractional flux uncertainty corresponds to a systematic uncertainty in the Vega-based magnitude zeropoint of 0.15 mag. Using the long exposures would not gain much in signal to noise ratio, because the SNR is independent of exposure time when an object trails in an image.

Table 4.3: ρ Ceti data.

Frame	UT	x^{a} (pixel)	y^{a} (pixel)	ϕ^{b} (ADU)	c^{c} (ADU pixel^{-1})
110	$06^{\mathrm{h}}19^{\mathrm{m}}01^{\mathrm{s}}$	925.4	257.7	92.6	14.6
111	$06^{\mathrm{h}}19^{\mathrm{m}}22^{\mathrm{s}}$	923.5	257.8	117.0	15.5
112	$06^{\mathrm{h}}19^{\mathrm{m}}44^{\mathrm{s}}$	921.7	257.9	129.6	13.6
113	$06^{\mathrm{h}}20^{\mathrm{m}}05^{\mathrm{s}}$	919.1	257.8	119.2	15.3
114	$06^{\mathrm{h}}20^{\mathrm{m}}26^{\mathrm{s}}$	916.8	258.0	136.7	15.3

---

[a] Centroid of the star.

[b] ρ Ceti flux.

[c] Local sky.

The rate of motion of a star at a known right ascension and declination allows for the mapping from pixels to arcseconds in the region near the star. The data from Table 4.3 were also used to this end. ρ Ceti was at a declination of -12.29 deg, implying an apparent motion across the sky of $\mu = 15$ arcsec sec^{-1} $\cos 12.29 =$ 14.66 arcsec sec^{-1}. We detected the object as moving 8.6 pixel in 85 sec, or 0.101 pixel sec^{-1}. This implies a plate scale of 144.9 arcsec pixel^{-1}, so that each pixel subtends an area of $20,995$ arcsec^2, or 5.8 arcmin^2. We consider this plate scale to be determined with a fractional uncertainty of about 5%, due to both the 1 sec granularity in the timing between exposures and the centroid measurement uncertainty for the star. Our dynamic plate scale determination is also within 6% of the 153.4 arcsec pixel^{-1} that was returned by astrometry.net, based on matching sources across the field to cataloged objects. In one of our longer exposures we measured the trail length of a star at this same location on the array as spanning 31.2 pixels in a 300 sec exposure, again confirming the plate scale determination at the 5% level.

The calibration source, and the region around it where we determined the sky brightness values, reside near a corner of the field. The rays that are brought to a focus at this location pass through the filter at an angle of 18.6 deg, while the median LSST incidence angle is 18.9 deg. We therefore consider the center of our effective passband at this location to be a good match to LSST's, but the shape at the passband edges will still differ somewhat.

With the photometric calibration and plate scale in hand, we were in a position to convert the sky brightness values, Σ, into Vega-based units of mag arcsec^{-2}. We converted the sky brightness values into units of ADU $\sec^{-1}$ arcsec^{-2} by dividing by 20,995 arcsec^2 pixel^{-1}. We then computed the Vega-based sky brightness using the flux from the comparison star, as

$$\Sigma^{\mathrm{Vega}} = -2.5\log(\phi/5.95) + 4.85\,\frac{\mathrm{mag}}{\mathrm{arcsec}^2} \tag{4.2}$$

where ϕ is the sky flux in ADU $\sec^{-1}$ arcsec^{-2}. Note that we selected a region for sky brightness determination that surrounded the calibration star to minimize our sensitivity to large scale flatfielding errors and pixel scale variations. The final zeropoint that converts all temporal results of Figure 4.5 to Vega magnitudes is $\Sigma = \Delta\Sigma + 17.8$ mag arcsec^{-2} (Vega).

We also supply the conversion of Vega magnitudes through the y band to AB magnitudes, because, while the AB and Vega magnitude scales are matched at the V band, they monotonically diverge at longer wavelengths. The Spitzer flux conversion utility at `http://ssc.spitzer.caltech.edu/tools/magtojy/` delivers $\mathrm{AB}_y^{\mathrm{Vega}} = 0.5$ mag with an uncertainty of 0.05 mag,, where $y^{\mathrm{AB}} = y^{\mathrm{Vega}} + \mathrm{AB}_y^{\mathrm{Vega}}$. This level of uncertainty is adequate for our purposes here. The conversion also agrees within the uncertainties with the AB-to-Vega offset terms presented in Table 7 of Hewett et al. (2006). Thus the conversion $\Sigma = \Delta\Sigma + 18.3$ mag (AB) brings all temporal results of Figure 4.5 into the AB system. Table 4.4 presents a summary of the potential sources of systematic error that might afflict these results.

Table 4.4: Systematic error budget.

Source	Error[a]
Sky area pixel^{-1}	0.05
Vega-system zeropoint	0.15
AB system zeropoint	0.05
Stray & scattered light	Unknown
Photometric conditions	0.01
Passband errors	Unknown

4.7 Conclusions

We have performed first measurements of y_3 band sky brightness in Chile from Cerro Tololo, and have argued that these results to apply to the nearby LSST site on Cerro Pachon. We observed rms spatial variability of 3–4% due to atmospheric gravity waves on scales of a few degrees and larger, and a factor of 2 variability in flux over the course of the nights we observed. These relative results make no reference to absolute calibrations, and we argue that they apply to nearly any y band variant because the sky background is due overwhelming to narrowband OH

---

[a] Estimated upper limit of systematic error.

emission. Finally, we estimate an absolute zeropoint and find the mean sky level is about 17.8 mag arcsec^{-2}. Our absolute calibration suffers up to 20% systematic uncertainty from zeropoint and pixel scale measurement errors, while our relative photometry is uncertain at about a percent.

Previous aeronomy work has characterized the OH background in depth, and suggests that the variability is somewhat predictable. We expect the sky background through any similar, CCD-based y band variant to fluctuate significantly, although nominal variation and absolute levels will differ depending on the precise nature of the total filter response curve. Our qualitative results and conclusions should apply to any y band.

The variability suggests that sky survey projects would benefit from a y band sky brightness monitor, and an adaptive strategy that would exploit times when the y sky is dark to take observations in this band. The background in y appears uniform to within 4% over much of the sky, so we advise it is better to chase *times* of low background than to find *directions* of dark sky in y. The coherent spatial structures in y band airglow present a potential difficulty to sky-based illumination correction strategies. Assuming random Gaussian fluctuations, 15 images or more are needed to achieve sub-percent uniformity over fields of view larger than about a degree. The spatial coherence of the gravity waves means the fluctuations are not random, making this a lower limit.

We have demonstrated the effectiveness of this apparatus. Given the observed variability in y_3 band sky brightness, there is considerable merit in implementing a long term monitor at the LSST site. Having long term sky brightness data in hand early will inform the optimal scheduling of the LSST system.

4.8 Acknowledgments

We thank the LSST Corporation, Harvard University and the Department of Energy Office of Science and the National Science Foundation for their support. The LSST design and development activity is supported by the National Science Foundation under Scientific Program Order No. 9 (AST-0551161) through Cooperative Agreement AST-0132798. Additional funding comes from private donations, in-kind support at Department of Energy laboratories and other LSSTC Institutional Members. We thank the CTIO scientific and technical staff for their invaluable help in setting up these observations. We are also very grateful to the team that is establishing the astrometry.net (`http://astrometry.net/`) online resource, which we used in its testing phase to determine the centers of the images we obtained. This publication makes use of data products from the Two Micron All Sky Survey, which is a joint project of the University of Massachusetts and the Infrared Processing and Analysis Center/California Institute of Technology, funded by the National Aeronautics and Space Administration and the National Science Foundation. SIMBAD too.

Bibliography

Abell, G. O., Corwin, Jr., H. G., & Olowin, R. P. 1989a, ApJS, 70, 1

—. 1989b, ApJS, 70, 1

Albrecht, A., Bernstein, G., Cahn, R., Freedman, W. L., Hewitt, J., Hu, W., Huth, J., Kamionkowski, M., Kolb, E. W., Knox, L., Mather, J. C., Staggs, S., & Suntzeff, N. B. 2006, ArXiv Astrophysics e-prints

Arp, H. C. & Madore, B. F. 1987, A Catalogue of Southern Peculiar Galaxies and Associations 2 volume set (A Catalogue of Southern Peculiar Galaxies and Associations 2 volume set, by Halton C. Arp and Barry F. Madore, pp. 504. ISBN 0521343364. Cambridge, UK: Cambridge University Press, May 1987.)

—. 1996, VizieR Online Data Catalog, 7170, 0

Baker, D. J. & Stair, A. T., J. 1988, Phys. Scr, 37, 611

Barris, B. J., Tonry, J. L., Novicki, M. C., & Wood-Vasey, W. M. 2005, AJ, 130, 2272

Battye, R. A. & Weller, J. 2003, Phys. Rev. D, 68, 083506

Beers, T. C., Flynn, K., & Gebhardt, K. 1990, AJ, 100, 32

Bertelli, G., Bressan, A., Chiosi, C., Fagotto, F., & Nasi, E. 1994, A&AS, 106, 275

Birkinshaw, M. 1999, Physics Reports, 310, 97

Böhringer, H., Schuecker, P., Guzzo, L., Collins, C. A., Voges, W., Cruddace, R. G., Ortiz-Gil, A., Chincarini, G., De Grandi, S., Edge, A. C., MacGillivray, H. T., Neumann, D. M., Schindler, S., & Shaver, P. 2004a, A&A, 425, 367

—. 2004b, A&A, 425, 367

Brott, I. & Hauschildt, P. H. 2005, in ESA Special Publication, Vol. 576, The Three-Dimensional Universe with Gaia, ed. C. Turon, K. S. O'Flaherty, & M. A. C. Perryman, 565–+

Bruzual, G. & Charlot, S. 2003, MNRAS, 344, 1000

Carlstrom, J. E., Ade, P. A. R., Aird, K. A., Benson, B. A., Bleem, L. E., Busetti, S., Chang, C. L., Chauvin, E., Cho, H., Crawford, T. M., Crites, A. T., Dobbs, M. A., Halverson, N. W., Heimsath, S., Holzapfel, W. L., Hrubes, J. D., Joy, M., Keisler, R., Lanting, T. M., Lee, A. T., Leitch, E. M., Leong, J., Lu, W., Lueker, M., McMahon, J. J., Mehl, J., Meyer, S. S., Mohr, J. J., Montroy, T. E., Padin, S., Plagge, T., Pryke, C., Ruhl, J. E., Schaffer, K. K., Schwan, D., Shirokoff, E., Spieler, H. G., Staniszewski, Z., Stark, A. A., & Vieira, K. V. J. D. 2009, submitted to PASP, arXiv:0907.4445

Carlstrom, J. E., Holder, G. P., & Reese, E. D. 2002, ARA&A, 40, 643

Chabrier, G. 2003, PASP, 115, 763

Clem, J. L., Vanden Berg, D. A., & Stetson, P. B. 2007, AJ, 134, 1890

Cosby, P. C., Sharpee, B. D., Slanger, T. G., Huestis, D. L., & Hanuschik, R. W. 2006, Journal of Geophysical Research (Space Physics), 111, 12307

Cosby, P. C. & Slanger, T. G. 2007, Canadian Journal of Physics, 85, 77

Covey, K. R., Ivezić, Ž., Schlegel, D., Finkbeiner, D., Padmanabhan, N., Lupton, R. H., Agüeros, M. A., Bochanski, J. J., Hawley, S. L., West, A. A., Seth, A., Kimball, A., Gogarten, S. M., Claire, M., Haggard, D., Kaib, N., Schneider, D. P., & Sesar, B. 2007, AJ, 134, 2398

Crawford, S. M., Bershady, M. A., & Hoessel, J. G. 2009, ApJ, 690, 1158

Cruddace, R., Voges, W., Böhringer, H., Collins, C. A., Romer, A. K., MacGillivray, H., Yentis, D., Schuecker, P., Ebeling, H., & De Grandi, S. 2002, ApJS, 140, 239

de Grandi, S., Böhringer, H., Guzzo, L., Molendi, S., Chincarini, G., Collins, C., Cruddace, R., Neumann, D., Schindler, S., Schuecker, P., & Voges, W. 1999, ApJ, 514, 148

Dressler, A. M., Sutin, B. M., & Bigelow, B. C. 2003a, in Society of Photo-Optical Instrumentation Engineers (SPIE) Conference Series, Vol. 4834, Society of Photo-Optical Instrumentation Engineers (SPIE) Conference Series, ed. P. Guhathakurta, 255–263

Dressler, A. M., Sutin, B. M., & Bigelow, B. C. 2003b, in Society of Photo-Optical Instrumentation Engineers (SPIE) Conference Series, Vol. 4834, Society of Photo-Optical Instrumentation Engineers (SPIE) Conference Series, ed. P. Guhathakurta, 255–263

Dunkley, J., Komatsu, E., Nolta, M. R., Spergel, D. N., Larson, D., Hinshaw, G., Page, L., Bennett, C. L., Gold, B., Jarosik, N., Weiland, J. L., Halpern, M., Hill, R. S., Kogut, A., Limon, M., Meyer, S. S., Tucker, G. S., Wollack, E., & Wright, E. L. 2009, ApJS, 180, 306

Efron, B. 1979, The Annals of Statistics, 7, 1

Evrard, A. E. 2004, 1

Finlator, K., Ivezić, Ž., Fan, X., Strauss, M. A., Knapp, G. R., Lupton, R. H., Gunn, J. E., Rockosi, C. M., Anderson, J. E., Csabai, I., Hennessy, G. S., Hindsley, R. B., McKay, T. A., Nichol, R. C., Schneider, D. P., Smith, J. A., York, D. G., & the SDSS Collaboration. 2000, AJ, 120, 2615

Foley, R. J., Papenkova, M. S., Swift, B. J., Filippenko, A. V., Li, W., Mazzali, P. A., Chornock, R., Leonard, D. C., & Van Dyk, S. D. 2003, PASP, 115, 1220

Fowler, J. W., Niemack, M. D., Dicker, S. R., Aboobaker, A. M., Ade, P. A. R., Battistelli, E. S., Devlin, M. J., Fisher, R. P., Halpern, M., Hargrave, P. C., Hincks, A. D., Kaul, M., Klein, J., Lau, J. M., Limon, M., Marriage, T. A., Mauskopf, P. D., Page, L., Staggs, S. T., Swetz, D. S., Switzer, E. R., Thornton, R. J., & Tucker, C. E. 2007, Appl. Opt., 46, 3444

Garcia, F. J., Taylor, M. J., & Kelley, M. C. 1997, Appl. Opt., 36, 7374

Gilbank, D. G., Yee, H. K. C., Ellingson, E., Gladders, M. D., Loh, Y., Barrientos, L. F., & Barkhouse, W. A. 2008, ApJ, 673, 742

Haehnelt, M. G. & Tegmark, M. 1996, MNRAS, 279, 545+

Haiman, Z., Mohr, J. J., & Holder, G. P. 2001, ApJ, 553, 545

Hansen, S. M., McKay, T. A., Wechsler, R. H., Annis, J., Sheldon, E. S., & Kimball, A. 2005, ApJ, 633, 122

Hansen, S. M., Sheldon, E. S., Wechsler, R. H., & Koester, B. P. 2009, ApJ, 699, 1333

Hawley, S. L., Covey, K. R., Knapp, G. R., Golimowski, D. A., Fan, X., Anderson, S. F., Gunn, J. E., Harris, H. C., Ivezić, Ž., Long, G. M., Lupton, R. H., McGehee, P. M., Narayanan, V., Peng, E., Schlegel, D., Schneider, D. P., Spahn, E. Y., Strauss, M. A., Szkody, P., Tsvetanov, Z., Walkowicz, L. M., Brinkmann, J., Harvanek, M., Hennessy, G. S., Kleinman, S. J., Krzesinski, J., Long, D., Neilsen, E. H., Newman, P. R., Nitta, A., Snedden, S. A., & York, D. G. 2002, AJ, 123, 3409

Herranz, D., Sanz, J. L., Barreiro, R. B., & Martínez-González, E. 2002a, ApJ, 580, 610

Herranz, D., Sanz, J. L., Hobson, M. P., Barreiro, R. B., Diego, J. M., Martínez-González, E., & Lasenby, A. N. 2002b, MNRAS, 336, 1057

Hewett, P. et al. 2006, MNRAS, 367, 454

High, F. W., Stalder, B., Song, J., Ade, P. A. R., Aird, K. A., Benson, B. A., Bertin, E., Bleem, L. E., Brodwin, M., Buckley-Geer, E. J., Carlstrom, J. E., Challis, P., Chang, C. L., Crawford, T. M., Crites, A. T., de Haan, T., Desai, S., Dobbs, M. A., Dudley, J. P., Foley, R. J., George, E. M., Gladders, M., Halverson, N. W., Hamuy, M., Hansen, S. M., Holder, G. P., Holzapfel, W. L., Hrubes, J. D., Joy, M., Keisler, R., Lee, A. T., Leitch, E. M., Lin, H., Loehr, A., Lueker, M., Marrone, D. P., McMahon, J. J., Mehl, J., Meyer, S. S., Mohr, J. J., Montroy, T. E., Morell, N., Ngeow, C.-C., Padin, S., Plagge, T., Pryke, C., Reichardt, C. L., Rest, A., Ruel, J., Ruhl, J. E., Schaffer, K. K., Shaw, L., Shirokoff, E., Smith, R. C., Spieler, H. G., Staniszewski, Z., Stark, A. A., Stubbs, C. W., Tucker, D. L., Vanderlinde, K., Vieira, J. D., Williamson, R., Wood-Vasey, W. M., Yang, Y., Zahn, O., & Zenteno, A. 2010a, submitted to ApJ, arXiv:1003.0005

High, F. W., Stubbs, C. W., Rest, A., Stalder, B., & Challis, P. 2009, AJ, 138, 110

High, F. W., Stubbs, C. W., Stalder, B., Gilmore, D. K., & Tonry, J. L. 2010b, submitted to PASP, arXiv:1002.3637v1

Hillenbrand, L. et al. 2002, PASP, 114, 708

Holder, G., Haiman, Z., & Mohr, J. J. 2001, ApJ, 560, L111

Ivezić, Ž., Sesar, B., Jurić, M., Bond, N., Dalcanton, J., Rockosi, C. M., Yanny, B., Newberg, H. J., Beers, T. C., Allende Prieto, C., Wilhelm, R., Lee, Y. S., Sivarani, T., Norris, J. E., Bailer-Jones, C. A. L., Re Fiorentin, P., Schlegel, D., Uomoto, A., Lupton, R. H., Knapp, G. R., Gunn, J. E., Covey, K. R., Smith, J. A., Miknaitis, G., Doi, M., Tanaka, M., Fukugita, M., Kent, S., Finkbeiner, D., Munn, J. A., Pier, J. R., Quinn, T., Hawley, S., Anderson, S., Kiuchi, F., Chen, A., Bushong, J., Sohi, H., Haggard, D., Kimball, A., Barentine, J., Brewington, H., Harvanek, M., Kleinman, S., Krzesinski, J., Long, D., Nitta, A., Snedden, S., Lee, B., Harris, H., Brinkmann, J., Schneider, D. P., & York, D. G. 2008, ApJ, 684, 287

Ivezić, Ž., Smith, J. A., Miknaitis, G., Lin, H., Tucker, D., Lupton, R. H., Gunn, J. E., Knapp, G. R., Strauss, M. A., Sesar, B., Doi, M., Tanaka, M., Fukugita, M., Holtzman, J., Kent, S., Yanny, B., Schlegel, D., Finkbeiner, D., Padmanabhan, N., Rockosi, C. M., Jurić, M., Bond, N., Lee, B., Stoughton, C., Jester, S., Harris, H., Harding, P., Morrison, H., Brinkmann, J., Schneider, D. P., & York, D. 2007, AJ, 134, 973

Jenkins, A., Frenk, C. S., White, S. D. M., Colberg, J. M., Cole, S., Evrard, A. E., Couchman, H. M. P., & Yoshida, N. 2001, MNRAS, 321, 372

Johnston, D. E., Sheldon, E. S., Wechsler, R. H., Rozo, E., Koester, B. P., Frieman, J. A., McKay, T. A., Evrard, A. E., Becker, M. R., & Annis, J. 2007, ArXiv e-prints

Jones, D. H., Saunders, W., Read, M., & Colless, M. 2005, Publications of the Astronomical Society of Australia, 22, 277

Jurić, M., Ivezić, Ž., Brooks, A., Lupton, R. H., Schlegel, D., Finkbeiner, D., Padmanabhan, N., Bond, N., Sesar, B., Rockosi, C. M., Knapp, G. R., Gunn, J. E., Sumi, T., Schneider, D. P., Barentine, J. C., Brewington, H. J., Brinkmann, J., Fukugita, M., Harvanek, M., Kleinman, S. J., Krzesinski, J., Long, D., Neilsen, Jr., E. H., Nitta, A., Snedden, S. A., & York, D. G. 2008, ApJ, 673, 864

Kaiser, N. et al. 2002, Proc. of the SPIE, 4836, 154

Katgert, P., Mazure, A., Perea, J., den Hartog, R., Moles, M., Le Fevre, O., Dubath, P., Focardi, P., Rhee, G., Jones, B., Escalera, E., Biviano, A., Gerbal, D., & Giuricin, G. 1996, A&A, 310, 8

Koester, B. P., McKay, T. A., Annis, J., Wechsler, R. H., Evrard, A. E., Rozo, E., Bleem, L., Sheldon, E. S., & Johnston, D. 2007, ApJ, 660, 221

Kriscuinas, K. et al. 2007, PASP, 119, 687

Kurtz, M. J. & Mink, D. J. 1998, PASP, 110, 934

Kurucz, R. L. 1993, VizieR Online Data Catalog, 6039, 0

Larson, K. A. & Whittet, D. C. B. 2005, ApJ, 623, 897

Lenz, D. D., Newberg, J., Rosner, R., Richards, G. T., & Stoughton, C. 1998, ApJS, 119, 121

Li, F., Liu, A. Z., Swenson, G. R., Hecht, J. H., & Robinson, W. A. 2005, Journal of Geophysical Research (Atmospheres), 110, 9

Lidman, C., Rosati, P., Tanaka, M., Strazzullo, V., Demarco, R., Mullis, C., Ageorges, N., Kissler-Patig, M., Petr-Gotzens, M. G., & Selman, F. 2008, A&A, 489, 981

Lima, M. & Hu, W. 2007, Phys. Rev. D, 76, 123013

Lin, Y. & Mohr, J. J. 2003, ApJ, 582, 574

Lin, Y., Mohr, J. J., & Stanford, S. A. 2004, ApJ, 610, 745

Lopes, P. A. A. 2007, MNRAS, 380, 1608

LSST Science Collaborations: Abell, P. A. et al. 2009, arXiv:0912.0201

MacDonald, E. C., Allen, P., Dalton, G., Moustakas, L. A., Heymans, C., Edmondson, E., Blake, C., Clewley, L., Hammell, M. C., Olding, E., Miller, L., Rawlings, S., Wall, J., Wegner, G., & Wolf, C. 2004, MNRAS, 352, 1255

Marigo, P., Girardi, L., Bressan, A., Groenewegen, M. A. T., Silva, L., & Granato, G. L. 2008, A&A, 482, 883

Marsh, D. R., Smith, A. K., Mlynczak, M. G., & Russell III, J. M. 2006, J. Geophys. Res., 111, A10S05

Marshall, D. J., Robin, A. C., Reylé, C., Schultheis, M., & Picaud, S. 2006, A&A, 453, 635

McCall, M. L. 2004, AJ, 128, 2144

McInnes, R. N., Menanteau, F., Heavens, A. F., Hughes, J. P., Jimenez, R., Massey, R., Simon, P., & Taylor, A. 2009, MNRAS, 399, L84

Mei, S., Holden, B. P., Blakeslee, J. P., Ford, H. C., Franx, M., Homeier, N. L., Illingworth, G. D., Jee, M. J., Overzier, R., Postman, M., Rosati, P., Van der Wel, A., & Bartlett, J. G. 2009, ApJ, 690, 42

Meinel, A. B. 1950a, ApJ, 111, 555

—. 1950b, ApJ, 112, 120

Melin, J.-B., Bartlett, J. G., & Delabrouille, J. 2006, A&A, 459, 341

Melo, S. M. L., Lowe, R. P., & Russell, J. P. 2000, J. Geophys. Res., 105, 12397

Menanteau, F. & Hughes, J. P. 2009, ApJ, 694, L136

Menanteau, F., Hughes, J. P., Barrientos, L. F., Deshpande, A. J., Hilton, M., Infante, L., Jimenez, R., Kosowsky, A., Moodley, K., Spergel, D., & Verde, L. 2010, ArXiv e-prints

Menanteau, F., Hughes, J. P., Jimenez, R., Hernandez-Monteagudo, C., Verde, L., Kosowsky, A., Moodley, K., Infante, L., & Roche, N. 2009, ApJ, 698, 1221

Menci, N., Rosati, P., Gobat, R., Strazzullo, V., Rettura, A., Mei, S., & Demarco, R. 2008, ApJ, 685, 863

Mermilliod, J.-C. 1987, Astron. Astrophys. Suppl. Ser., 71, 413

Miknaitis, G., Pignata, G., Rest, A., Wood-Vasey, W. M., Blondin, S., Challis, P., Smith, R. C., Stubbs, C. W., Suntzeff, N. B., Foley, R. J., Matheson, T., Tonry, J. L., Aguilera, C., Blackman, J. W., Becker, A. C., Clocchiatti, A., Covarrubias, R., Davis, T. M., Filippenko, A. V., Garg, A., Garnavich, P. M., Hicken, M., Jha, S., Krisciunas, K., Kirshner, R. P., Leibundgut, B., Li, W., Miceli, A., Narayan, G., Prieto, J. L., Riess, A. G., Salvo, M. E., Schmidt, B. P., Sollerman, J., Spyromilio, J., & Zenteno, A. 2007, ApJ, 666, 674

Mohr, J. J., Adams, D., Barkhouse, W., Beldica, C., Bertin, E., Cai, Y. D., da Costa, L. A. N., Darnell, J. A., Daues, G. E., Jarvis, M., Gower, M., Lin, H., Martelli, L., Neilsen, E., Ngeow, C., Ogando, R. L. C., Parga, A., Sheldon, E., Tucker, D., Kuropatkin, N., & Stoughton, C. 2008, in Society of Photo-Optical Instrumentation Engineers (SPIE) Conference Series, Vol. 7016, Society of Photo-Optical Instrumentation Engineers (SPIE) Conference Series

Molnar, S. M., Haiman, Z., Birkinshaw, M., & Mushotzky, R. F. 2004, ApJ, 601, 22

Morgan, W. W., Keenan, P. C., & Kellman, E. 1943, An atlas of stellar spectra, with an outline of spectral classification (Chicago, Ill., The University of Chicago press [1943])

Murphy, T., Sadler, E. M., Ekers, R. D., Massardi, M., Hancock, P. J., Mahony, E., Ricci, R., Burke-Spolaor, S., Calabretta, M., Chhetri, R., de Zotti, G., Edwards, P. G., Ekers, J. A., Jackson, C. A., Kesteven, M. J., Lindley, E., Newton-McGee, K., Phillips, C., Roberts, P., Sault, R. J., Staveley-Smith, L., Subrahmanyan, R., Walker, M. A., & Wilson, W. E. 2010, MNRAS, 154

Nakamura, T., Higashikawa, A., Tsuda, T., & Matsushita, Y. 1999, Earth, Planets, and Space, 51, 897

Narayan, R. & Bartelmann, M. 1996, ArXiv Astrophysics e-prints

Nelder, J. A. & Mead, R. 1965, Computer Journal, 7, 308

Ngeow, C., Mohr, J. J., Alam, T., Barkhouse, W. A., Beldica, C., Cai, D., Daues, G., Plante, R., Annis, J., Lin, H., Tucker, D., & Smith, R. C. 2006, in Society of Photo-Optical Instrumentation Engineers (SPIE) Conference Series, Vol. 6270, Society of Photo-Optical Instrumentation Engineers (SPIE) Conference Series

O'Connor, P. et al. 2006, Proc. of the SPIE, 6276, 53

Osip, D. J., Floyd, D., & Covarrubias, R. 2008a, in Society of Photo-Optical Instrumentation Engineers (SPIE) Conference Series, Vol. 7014, Society of Photo-Optical Instrumentation Engineers (SPIE) Conference Series

Osip, D. J., Floyd, D., & Covarrubias, R. 2008b, in Society of Photo-Optical Instrumentation Engineers (SPIE) Conference Series, Vol. 7014, Society of Photo-Optical Instrumentation Engineers (SPIE) Conference Series

Padmanabhan, N., Schlegel, D. J., Finkbeiner, D. P., Barentine, J. C., Blanton, M. R., Brewington, H. J., Gunn, J. E., Harvanek, M., Hogg, D. W., Ivezić, Ž., Johnston, D., Kent, S. M., Kleinman, S. J., Knapp, G. R., Krzesinski, J., Long, D., Neilsen, Jr., E. H., Nitta, A., Loomis, C., Lupton, R. H., Roweis, S., Snedden, S. A., Strauss, M. A., & Tucker, D. L. 2008, ApJ, 674, 1217

Patat, F. 2003, å, 400, 1183

Perlmutter, S., Aldering, G., Goldhaber, G., Knop, R. A., Nugent, P., Castro, P. G., Deustua, S., Fabbro, S., Goobar, A., Groom, D. E., Hook, I. M., Kim, A. G., Kim, M. Y., Lee, J. C., Nunes, N. J., Pain, R., Pennypacker, C. R., Quimby, R., Lidman, C., Ellis, R. S., Irwin, M., McMahon, R. G., Ruiz-Lapuente, P., Walton, N., Schaefer, B., Boyle, B. J., Filippenko, A. V., Matheson, T., Fruchter, A. S., Panagia, N., Newberg, H. J. M., Couch, W. J., & The Supernova Cosmology Project. 1999, ApJ, 517, 565, astro-ph/9812133

Pimbblet, K. A., Smail, I., Edge, A. C., O'Hely, E., Couch, W. J., & Zabludoff, A. I. 2006, MNRAS, 366, 645

Puxley, P. & the Gemini Observatory. 2001, `http://www.gemini.edu/sciops/ObsProcess/obsConstraints/atm-models/skybg_50_10.dat`

Rest, A., Stubbs, C., Becker, A. C., Miknaitis, G. A., Miceli, A., Covarrubias, R., Hawley, S. L., Smith, R. C., Suntzeff, N. B., Olsen, K., Prieto, J. L., Hiriart, R., Welch, D. L., Cook, K. H., Nikolaev, S., Huber, M., Prochtor, G., Clocchiatti, A., Minniti, D., Garg, A., Challis, P., Keller, S. C., & Schmidt, B. P. 2005, ApJ, 634, 1103

Reyes, R., Mandelbaum, R., Hirata, C., Bahcall, N., & Seljak, U. 2008, MNRAS, 390, 1157

Riess, A. G., Filippenko, A. V., Challis, P., Clocchiattia, A., Diercks, A., Garnavich, P. M., Gilliland, R. L., Hogan, C. J., Jha, S., Kirshner, R. P., Leibundgut, B., Phillips, M. M., Reiss, D., Schmidt, B. P., Schommer, R. A., Smith, R. C., Spyromilio, J., Stubbs, C., Suntzeff, N. B., & Tonry, J. 1998, AJ, 116, 1009

Rousselot, P., Lidman, C., Cuby, J.-G., Moreels, G., & Monnet, G. 2000, A&A, 354, 1134

Rozo, E., Rykoff, E. S., Evrard, A., Becker, M., McKay, T., Wechsler, R. H., Koester, B. P., Hao, J., Hansen, S., Sheldon, E., Johnston, D., Annis, J., & Frieman, J. 2009, ApJ, 699, 768

Rudnick, G., von der Linden, A., Pelló, R., Aragón-Salamanca, A., Marchesini, D., Clowe, D., De Lucia, G., Halliday, C., Jablonka, P., Milvang-Jensen, B., Poggianti, B., Saglia, R., Simard, L., White, S., & Zaritsky, D. 2009, ApJ, 700, 1559

Sanchez, F. 2007, PASP, 119, 1186

Schechter, P. 1976, ApJ, 203, 297

Schlegel, D. J., Finkbeiner, D. P., & Davis, M. 1998, ApJ, 500, 525

Schwope, A., Hasinger, G., Lehmann, I., Schwarz, R., Brunner, H., Neizvestny, S., Ugryumov, A., Balega, Y., Trümper, J., & Voges, W. 2000, Astronomische Nachrichten, 321, 1

Sesar, B., Ivezić, Ž., Lupton, R. H., Jurić, M., Gunn, J. E., Knapp, G. R., DeLee, N., Smith, J. A., Miknaitis, G., Lin, H., Tucker, D., Doi, M., Tanaka, M., Fukugita, M., Holtzman, J., Kent, S., Yanny, B., Schlegel, D., Finkbeiner, D., Padmanabhan, N., Rockosi, C. M., Bond, N., Lee, B., Stoughton, C., Jester, S., Harris, H., Harding, P., Brinkmann, J., Schneider, D. P., York, D., Richmond, M. W., & Vanden Berk, D. 2007, AJ, 134, 2236

Skrutskie, R. M. et al. 2006, AJ, 131, 1163

Smith, J. A., Tucker, D. L., Allam, S. S., & Rodgers, C. T. 2003, AJ, 126, 2037

Smith, J. A., Tucker, D. L., Kent, S., Richmond, M. W., Fukugita, M., Ichikawa, T., Ichikawa, S.-i., Jorgensen, A. M., Uomoto, A., Gunn, J. E., Hamabe, M., Watanabe, M., Tolea, A., Henden, A., Annis, J., Pier, J. R., McKay, T. A., Brinkmann, J., Chen, B., Holtzman, J., Shimasaku, K., & York, D. G. 2002, AJ, 123, 2121

Smolčić, V., Ivezić, Ž., Knapp, G. R., Lupton, R. H., Pavlovski, K., Ilijić, S., Schlegel, D., Smith, J. A., McGehee, P. M., Silvestri, N. M., Hawley, S. L., Rockosi, C., Gunn, J. E., Strauss, M. A., Fan, X., Eisenstein, D., & Harris, H. 2004, ApJ, 615, L141

Staniszewski, Z., Ade, P. A. R., Aird, K. A., Benson, B. A., Bleem, L. E., Carlstrom, J. E., Chang, C. L., Cho, H.-M., Crawford, T. M., Crites, A. T., de Haan, T., Dobbs, M. A., Halverson, N. W., Holder, G. P., Holzapfel, W. L., Hrubes, J. D., Joy, M., Keisler, R., Lanting, T. M., Lee, A. T., Leitch, E. M., Loehr, A., Lueker, M., McMahon, J. J., Mehl, J., Meyer, S. S., Mohr, J. J., Montroy, T. E., Ngeow, C.-C., Padin, S., Plagge, T., Pryke, C., Reichardt, C. L., Ruhl, J. E., Schaffer, K. K., Shaw, L., Shirokoff, E., Spieler, H. G., Stalder, B., Stark, A. A., Vanderlinde, K., Vieira, J. D., Zahn, O., & Zenteno, A. 2009, ApJ, 701, 32

Straizys, V., Lazauskaite, R., Liubertas, R., & Azusienis, A. 1998, Baltic Astronomy, 7, 605

Struble, M. F. & Rood, H. J. 1999, ApJS, 125, 35

Stubbs, C. W., High, F. W., George, M. R., DeRose, K. L., Blondin, S., Tonry, J. L., Chambers, K. C., Granett, B. R., Burke, D. L., & Smith, R. C. 2007, PASP, 119, 1163

Stubbs, C. W. & Tonry, J. L. 2006, ApJ, 646, 1436

Sunyaev, R. A. & Zel'dovich, Y. B. 1972, Comments on Astrophysics and Space Physics, 4, 173

Taylor, M. J. & Hill, M. J. 1991, Geophys. Res. Lett., 18, 1333

Tinker, J., Kravtsov, A. V., Klypin, A., Abazajian, K., Warren, M., Yepes, G., Gottlöber, S., & Holz, D. E. 2008, ApJ, 688, 709

van Dokkum, P. G., Franx, M., Kelson, D. D., Illingworth, G. D., Fisher, D., & Fabricant, D. 1998, ApJ, 500, 714

Vanderlinde, K., Crawford, T. M., de Haan, T., Dudley, J. P., Shaw, L., Ade, P. A. R., Aird, K. A., Benson, B. A., Bleem, L. E., Brodwin, M., Carlstrom, J. E., Chang, C. L., Crites, A. T., Desai, S., Dobbs, M. A., Foley, R. J., George, E. M., Gladders, M., Hall, N. R., Halverson, N. W., High, F. W., Holder, G. P., Holzapfel, W. L., Hrubes, J. D., Joy, M., Keisler, R., Knox, L., Lee, A. T., Leitch, E. M., Loehr, A., Lueker, M., Marrone, D. P., McMahon, J. J., Mehl, J., Meyer, S. S., Mohr, J. J., Montroy, T. E., Ngeow, C.-C., Padin, S., Plagge, T., Pryke, C., Reichardt, C. L., Rest, A., Ruel, J., Ruhl, J. E., Schaffer, K. K., Shirokoff, E., Song, J., Spieler, H. G., Stalder, B., Staniszewski, Z., Stark, A. A., Stubbs, C. W., van Engelen, A., Vieira, J. D., Williamson, R., Yang, Y., Zahn, O., & Zenteno, A. 2010, submitted to ApJ, arXiv:1003.0003

Vikhlinin, A., Kravtsov, A. V., Burenin, R. A., Ebeling, H., Forman, W. R., Hornstrup, A., Jones, C., Murray, S. S., Nagai, D., Quintana, H., & Voevodkin, A. 2009, ApJ, 692, 1060

Voges, W., Aschenbach, B., Boller, T., Bräuninger, H., Briel, U., Burkert, W., Dennerl, K., Englhauser, J., Gruber, R., Haberl, F., Hartner, G., Hasinger, G., Kürster, M., Pfeffermann, E., Pietsch, W., Predehl, P., Rosso, C., Schmitt, J. H. M. M., Trümper, J., & Zimmermann, H. U. 1999, A&A, 349, 389

Voit, G. M. 2005, Reviews of Modern Physics, 77, 207

Wade, R. A. & Horne, K. 1988, ApJ, 324, 411

Wang, L. & Steinhardt, P. J. 1998, ApJ, 508, 483

Wang, S., Khoury, J., Haiman, Z., & May, M. 2004, Phys. Rev. D, 70, 123008

Warren, S. J. et al. 2007, MNRAS, 375, 213

Wiens, R. H. et al. 1997, Advances in Space Research, 19, 677

Witham, A. R., Knigge, C., Drew, J. E., Greimel, R., Steeghs, D., Gänsicke, B. T., Groot, P. J., & Mampaso, A. 2008, MNRAS, 384, 1277

Wright, E. L. 2006, PASP, 118, 1711

Zaritsky, D., Gonzalez, A. H., & Zabludoff, A. I. 2006, ApJ, 638, 725

Zwicky, F. 1933, Helvetica Physica Acta, 6, 110